République Algérienne Démocratique et Populaire
Ministère de l'Enseignement Supérieur et de la Recherche Scientifique

Université Echahid Hamma Lakhdar - El Oued
Faculté de la technologie
Département De Génie Mécanique

Thèse

Thèse présentée en vue de l'obtention
Du diplôme de
Doctorat LMD en Génie Mécanique

Option : énergétique

Thème

Contribution à la conception des séchoirs solaires à haute performance utilisant un outil de simulation couplé avec la méthode des plans d'expériences

Présenté par

Abderrahmane BENHAMZA

Soutenu publiquement le: 11 / 06 /2021

Devant le jury composé de:

Pr. Boubaker BENHAOUA	Université Echahid Hamma Lakhdar Eloued	Président
Pr. Fethi BOURAS	Université Echahid Hamma Lakhdar Eloued	Examinateur
Dr. Ali BOUKHARI	Université Echahid Hamma Lakhdar Eloued	Examinateur
Dr. Djamel MENNOUCHE	Université Kasdi Merbah Ouargla	Examinateur
Pr. Abdelghani BOUBEKRI	Université Kasdi Merbah Ouargla	Encadreur
Dr. Abdelmalek ATIA	Université Echahid Hamma Lakhdar Eloued	Co-Encadreur
Pr. Djamel BECHKI	Université Kasdi Merbah Ouargla	Invité

People's Democratic Republic of Algeria
Ministry of High Education and Scientific Research

University of El Oued

A thesis Submitted in Partial Fulfilment of the Requirements for the Degree of

Doctor of Philosophy
in
Energy engineering

by

Abderrahmane BENHAMZA

Contribution to the design of high-performance solar dryers using simulation tools coupled with design of experiments

Jury members:

Pr. Boubaker BENHAOUA	University of Eloued	Chairman
Pr. Fethi BOURAS	University of Eloued	Examiner
Dr. Ali BOUKHARI	University of Eloued	Examiner
Dr. Djamel MENNOUCHE	Kasdi Merbah University Ouargla	Examiner
Pr. Abdelghani BOUBEKRI	Kasdi Merbah University Ouargla	Supervisor
Dr. Abdelmalek ATIA	Kasdi Merbah University Ouargla	Co-supervisor
Pr. Djamel BECHKI	Kasdi Merbah University Ouargla	Invited

June 2021

I dedicate this work to:

My mother is my aunt

My brother

My friends

My family

ACKNOWLEDGEMENTS

The present thesis was carried out in the *department of mechanical engineering, at Eloued university, Eloued, Algeria* and *Laboratory of New and Renewable Energy Development in Arid and Saharan Zones (LENREZA), Kasdi Merbah University, Ouargla, Algeria*. Furthermore, this thesis has been carried in collaboration with researchers from *laboratory of Control and Computing for Intelligent Systems and Green Energy, Cadi Ayyad University, Marrakesh, Morocco*, And *Mechanical Engineering Department, Kocaeli University, Kocaeli, Turkey.*

First, I am very grateful to the almighty Allah for everything, and for giving me the key and opportunity to accomplish my PhD thesis.

Foremost, I wish to express my deepest gratitude to my supervisor **Prof. Abdelghani BOUBEKRI** for the continuous support during the long period from the first day in my master degree until being a PhD, for his patience, motivation, supervision, and immense knowledge.

Besides, I would like also to thank my co-supervisor **Dr. Abdelmalek ATIA** for his motivation, supervision, his guidance through this process; his discussion, ideas, and feedback have been absolutely invaluable.

I would also like to show my gratitude for the honorable jury members who accepted to examine my thesis: **Pr. Boubaker BENHAOUA** for his acceptance to be the president of the examination committee, **Pr. Fethi BOURAS**, **Dr. Ali BOUKHARI**, **Dr. Djamel MENNOUCHE** for their acceptance to examine this PhD thesis, and **Pr. Djamel BECHKI** for accepting the invitation to be one of the jury members.

I would like to thank **Prof. Naji ABDENOURI** member of research team of "Control and Computing for Intelligent Systems and Green Energy, Cadi Ayyad University, Marrakesh, Morocco'' for his agreeing to welcome me to his laboratory, I am deeply grateful for his confidence, his patience, his sympathy and for his dedication. I would like to thank to my friends **Dr. Hicham el Ferouali, Dr. Ahmed Zoukit and Mr. Mouhamed Bounagui** for their help during my fellowship period.

I would like to thank **Prof. Müslüm Arıcı** professor at Kocaeli University, for the support, supervision and especially for sharing with me the keys that helped me to develop my scientific writing skills

My deepest thanks go to the Department of Mechanical Engineering, at Eloued university. The financial support of my university is greatly appreciated. I wish to thank all my colleagues, staff and technicians in LENREZA Laboratory. It is very pleasant to work in such a laboratory.

Finally, I would especially like to thank my amazing family for the love, support, and constant encouragement I have gotten over the years.

CONTENTS

CHAPTER 1 Bibligraphic study

CHAPTER 2 Optimization of solar air heater for drying applications

CHAPTER 3 Design optimization of indirect type solar dryer

CHAPTER 4 Drying uniformity analysis within an indirect solar dryer using image processing

$\dot{m}$	Mass flow rate ($kg.s^{-1}$)
C	Specific heat ($J.kg^{-1}.K^{-1}$)
D	Distance between each two components (m)
D_h	Hydraulic diameter (m)
D_1	Air gap height (m)
D_2	Flow duct height (m)
I	Solar radiation ($W.m^{-2}$)
H	Enthalpy ($J.kg^{-1}$)
h	Heat transfer coefficient ($W.m^{-2}.K^{-1}$)
IP	Improvement potential (W)
IT	Initial temperatures
j	Node in flow direction
k	Thermal conductivity ($W.m^{-1}.K^{-1}$)
L	Length of the solar air heater (m)
N	Number of nodes in the flow direction
Nn	Total number of nodes
Nu	Nusselt number
Pr	Prandtl number
R	Coefficient of radiant heat transfer
Ra	Rayleigh number
Re	Reynolds number
S	Entropy ($J.kg^{-1}.K^{-1}$)
T	Temperature (K)
t	Time (s)
U	Heat loss coefficient from the bottom ($W.m^{-2}.K^{-1}$)
V_{fluid}	Fluid velocity ($m.s^{-1}$)
W	Solar air heater width (m)
W_v	Wind velocity ($m.s^{-1}$)

Greek symbols

δ	Thickness (m)
α	Absorption coefficient
α_d	Thermal diffusivity ($m^2.s^{-1}$)
τ	Transmission coefficient
$(\tau\alpha)$	Effective transmittance-absorptance product
ρ	Density (kg/m^3)
θ	Tilt angle of the SAH (rad)
σ	Stefan-Boltzman constant ($5.67x10^{-8}$ W. m^{-2} .K^{-4})
υ	Kinematic viscosity ($m^2.s^{-1}$)
η	Efficiency

$\vec{v}$	vector of velocity
ρ	density
$\ddot{\tau}$	Reynolds stress tensor
ρ_0	the reference density
T_0	reference temperature
B	thermal expansion coefficient of the fluid.
k	Turbulence kinetic energy ()
ε	Dissipation rate of turbulent kinetic

Subscripts

abs	Absorber
amb	Ambient
en	Energy
ex	Exergy
f	Fin
fluid	Flowing air in the solar air heater
g	Glass
ga	Air gap between the absorber and glass
i	Inlet
ins	Insulation in the bottom
out	Outlet
So	Solar

ABBREVIATIONS

BBD	Box-Behnken Design
CFD	Computational fluid dynamics
DES	Desirability function
DoE	Design of experiments
GD	Geometric dimensions
ISD	Indirect type solar dryer
OP	Operating parameters
RSM	Response surface methodology
SAH	Solar air heater
TPP	Thermo-physical properties

GENERAL INTRODUCTION

Currently, one third to half of all food globally produced is lost or wasted along food supply chains *(Arias Bustos & Moors, 2018; FAO., 2013; Lundqvist et al., 2008)*. Reducing the existing high rates of global food loss and waste, including post-harvest loss, along the various production and supply chains, will play a key role in tackling the problem of food insecurity. *Hodges et al. (2011)* reported that the critical factors influencing food loss in developed countries occur at the consumption stage, whereas in less developed countries, most losses mainly occur early in the value chain, especially in post-harvest handling and processing *(Chegere, 2018)*. High rates of food loss contribute to food shortages and have left millions in low-income countries suffering from malnutrition *(Food & Organization, 2010; Munesue et al., 2015; Udomkun et al., 2020)*. In this regard, the use of appropriate drying technologies can potentially enable small-scale producers to significantly reduce post-harvest losses, improve the quality of food, and generate income and employment opportunities.

Drying, as an energy-intensive process, plays a major role in various sectors, ranging from food industry to wood industry, and affects economies worldwide. Drying applications consume a noticeable part of the world's produced energy and require a careful attention from microlevel to macrolevel applications to make them more efficient, more cost effective, and more environmentally benign. Bringing all these dimensions into the designs, analyses, and assessments of drying systems for various practical applications is of paramount significance *(Dinçer & Zamfirescu, 2016)*. In agriculture sector, drying is one of the important preservation techniques for fruits and vegetables. Removing water by drying is the oldest technique used in many applications such as wood pulp drying for making paper, drying for food preservation and drying building materials *(Lamidi et al., 2019)*.

Covering the drying energy demand is highly related to the available energy sources in the country. Due to the large area and weather diversity, Algeria has a high potential of solar energy particularly in the Saharan region (southern regions). In fact, the total solar potential of Algeria is estimated to 169,440 TW h per year *(Settou et al., 2021)*, which represents 5000 times the national annual power consumption in electricity and around 60 times the energy consumed by the European community. The insolation duration in Algeria is around 2650 h per year for the coastal regions, 3900 h per year for the high plateaus and Saharan regions and it increases to 3500 h per year for the Sahara *(CEREFE, 2020)*. In terms of received energy, the coastal regions dispose of 1700 $kWh.m^{-2}year^{-1}$; it increases to 1900 $kWh.m^{-2}year^{-1}$ for high plateaus and attains 2650 $kWh.m^{-2}year^{-1}$ for the Sahara.

Solar drying is abundantly available, free of cost and is an environmentally friendly energy source. The food is dried in open air called open sun drying (OSD). It is the oldest and traditional method of drying where the material to be dried is spread over the ground or on mats, or on trays allow them to dry throughout the day. But OSD has a lot of disadvantages as the materials are put in open air, therefore, the food material is easily contaminated by dirt, dust, pollution, damage by animals, birds or insects and their dropping, degradation through exposure to direct sun radiation, storm, and dew, additional losses during storage due to insufficient or non-uniform drying. These all are lead to infestation by fungi, bacteria and other microorganism causing the spoilage of the material *(Anderson & Westerlund, 2014)*.

Solar dryer system is mainly used for drying fruits and vegetables and the final product is clean and hygienic, if necessary provisions *(Şevik, 2013)* are made in the setup. It also saves energy and occupies less space. The main importance of solar dryer is, it protects the environment by not releasing carbon monoxide, carbon dioxide, oxides of nitrogen and other smokes as internal combustion engine and power plants release. Among the different types of dryer, indirect type solar dryer (ISD) has better product quality on the dried product than OSD and direct type solar dryer as it can provide the required temperature, better control over drying, retention of product color, nil damage to crops, and is highly recommended for photo-sensitive materials such as lemon, cucumber, papaya, etc.

The application of software is very important to develop and analyze the mathematical models and predicting the performance of different kind of solar drying systems. The design of solar dryer can be optimized with the help of software and it saves time which consumed during experiments. It is also useful for predicting the crop temperature, moisture content and drying rate, drying kinetics, texture and color of the crop. Computational fluid dynamics (CFD) can be used for the analysis and investigation of air flow, air flow rate inside the solar dryer, temperature distribution pattern and humidity, through appropriate simulation of energy and momentum equations and heat and mass transfer in both gaseous and solid phases *(Chen et al., 2008; Singh Chauhan et al., 2015)*. Therefore, CFD has been considered as a promising method which could help developing the design of new dryers, enhancing current dryers and the most important aspect of utilization of this method in the food industry research and development is “food quality” improvement.

Experimental design is a collection of tools used for studying the behavior of a system. Experimental design, or design of experiments, involves planning and performing a set of experiments to determine the effects of experimental variables on that system. The required experiments are also performed in a way that maximizes the information that can be extracted from a limited number of experiments. Once a satisfactory model has been determined, it can be used for predicting future observations within the original design range. Experimental design is thus useful for, not only studying, but also developing and optimizing a wide range of engineering systems *(Mäkelä, 2017)*.

The considerable number of experiments needed to optimize the solar dryer design is extremely time-consuming, besides from an economic point of view, it is not efficient. Furthermore, traditional factor-by-factor parametric optimization study is implicit, and a different optimal design might be produced in the presence of the cumulative impact of all factors. Therefore, in the present work, design of experiments (DoE) approach was coupled to the numerical modeling technique to provide an explicit conclusion. The main purpose of using this technique is to determine the optimized combination of ISD geometrical variables which attains the best possible performances for agri-food drying applications. The optimization process was based on Response Surface Methodology (RSM) regression models and the desirability function.

In the first chapter entitled « **BIBLIGRAPHIC STUDY** », detailed bibliographic search has been carried out in order to select the type of SD and the optimization method. The importance of solar air heaters (SAHs) in indirect SDs and SAHs' optimization methods in order to choose the optimization objectives then used in chapters 2, 3, and 4. Also the problematic of the drying uniformity in SDs cabinet was discussed.

In the second chapter entitled « **OPTIMIZATION OF SOLAR AIR HEATER FOR DRYING APPLICATIONS** », the indirect solar dryer was chosen based on the literature review. In this type of dryer, the SAH is the thermal energy motor used for drying food products. The aim of this chapter was the optimization of the SAH using the DoE coupled with a MATLAB code.

In the third chapter entitled **« DESIGN OPTIMIZATION OF CABINET INDIRECT SOLAR DRYER »** in order to find the optimal design of the indirect SD, a unidirectional model to multidirectional modeling using the CFD approach in order to examine the uniformity of the dynamic and thermal contours in the indirect solar dryer. Firstly, the description of the experimental prototype, the measurement procedure, measuring instruments and the uncertainty analysis has been presented in this chapter. Secondly, the steps of numerical modeling, mesh independence, initial and boundary conditions and other numerical parameters have been summarized in the material and methods part of the same chapter. The results of the validation of the model with the experimental results. Finally, the results of the implementation of the design of experiments method using data from the numerical tests developed by the validated CFD model. In order to improve the uniformity of the thermal and dynamic fields of the air in the drying chamber, the effect of the geometric parameters of the chimney as well as the effect of some parameters of the chamber has been tested and the optimal geometry has been tested.

In the fourth and last chapter entitled « **DRYING UNIFORMITY ANALYSIS WITHIN AN INDIRECT SOLAR DRYER USING A COLOR DENSITY METHOD** », a new method for estimating the air-drying uniformity inside the drying chamber has been tested. To define the best SD configuration ensuring uniform drying of food products, digital image processing is used as an accurate means compared to the visual reading of the speed and temperature distribution contours obtained from the CFD software. For this purpose, Multicolor Engine software was used for image analysis by calculating the percentage of each specific color in the image. Based on this last method (image processing) and CFD model developed and validated in the chapter 3, the effect of adding a solar chimney and of using forced convection to improve the dynamic fields in the drying chamber are examined using.

The main results of the above-mentioned sections are briefly presented at the end of this thesis as a general conclusion. In addition; the general conclusion followed by a perspective part includes three points that we were unable to do, either because of time or of instruments.

1. Introduction

This chapter presents a review of the previous works dealing with the improvement methodologies of indirect solar dryers. This study is aimed thus to determine the different techniques and factors which can highly improve the thermal performance of indirect solar drying systems. Solar air heaters are also studied separately in this chapter. The effect of some parameters such as operating conditions and geometrical conditions was considered and discussed. Moreover, to easily identify the shortcomings in the literature and determine the main trends in the topic of this thesis, bibliometric analysis has been carried on specific fields such us optimization of solar air heaters, drying uniformity.

2. Solar drying

Rural food processing, particularly in under-developed and developing countries majorly relies on solar energy. Among various unit operations involved, drying is a complex process involving simultaneous heat and mass transfer; with a reduction in product moisture content, drying offers multiple benefits, particularly the increase in product shelf- life. Reduction in moisture content to sufficient levels can slow down the action of enzymes, bacteria, yeast, and molds *(Mohana et al., 2020)*.

Before invention of the first solar dryer, traditionally agriculture and marine products were dried under open solar drying. This method avoids price rise and rapid depletion of fossil fuels since this method based on solar energy which is considered free, renewable and clean energy source. However, the process itself is highly dependent on weather and climate conditions, specifically the availability of sunlight, humidity and wind. The drying process can be interrupted by raining, cloudy weather or other adverse conditions. These factors are uncontrollable and resulted in ineffective drying, which can possibly lead to other problems such as prolonged drying time, inadequate drying, over-heating or fungal attack *(Kamarulzaman et al., 2021)*. Additionally, during drying the products are exposed to various impurities from surrounding such as dust, rain water, pests and animals.

Alternatively using solar drying systems allow to avoid the drawbacks of the open-sun drying such as deterioration of dried products caused by insects and direct exposure to the sun *(El Hage et al., 2018; M. Kumar et al., 2016)*. Moreover, compared to the open-sun drying, the developed solar dryers dry the products in a shorter period and offer the possibility of controlled drying *(Zoukit et al., 2019a, 2019b)*. Many developments and improvements made on solar dryers by researchers.

Solar dryers can be grouped according to two main aspects (i) the movement of air inside the dryer, and (ii) products exposure to solar radiation as well as hybrid that is shown in *Figure 1.1*.

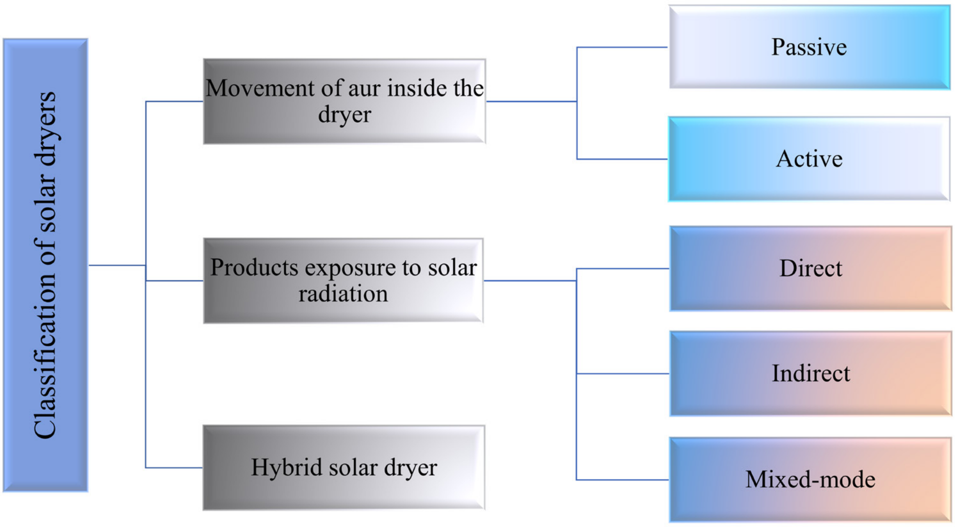

Figure 1.1 Classification of solar dryers (Kamarulzaman et al., 2021).

3. Indirect solar dryer

Among the different systems of solar drying, the indirect type solar dryer (ISD) type ensures the best quality of dried products, texture, as well as maintains at best the fresh product color. The principle of the ISD is that the food is heated indirectly through the air coming from the solar air heater (SAH), not by direct exposure to sunlight *(Messaoud; Sandali et al., 2019; P. Singh & Gaur, 2020)*. Due to the unique features of this type of solar dryers (i.e. ISD), Lingayat et al. *(Lingayat et al., 2020)* discussed literature data of different configurations investigated by researchers used this technique. Parameters affecting the drying rate, types of energy storage used in the ISDs, and the important findings were listed and tabulated. In that recent paper, the authors concluded that a well-designed ISD with minimum operating and maintenance cost is necessary for an effective drying process.

Many configurations and designs of ISDs have been developed in the literature. The conventional type contains a SAH and drying chamber. The SAH allows solar irradiation conversion into thermal energy at the absorber which transfers the heated air to the chamber by natural or forced convection *(Tarik Hadibi et al., 2021)*. The heated air triggers the evaporation of the water inside the product after absorbing the thermal energy carried by the air. In this case, the dried product can be easily stored in pressure and temperature conditions close to the ambient *(Abhay et al., 2018)*. The advantages of the ISD were highlighted by Vijayan et al.

(Vijayan, Arjunan, & Kumar, 2020). The reduced time in indirect solar drying was estimated by performing a comparison with alternative drying types. The drying time of bitter gourd slices using ISD was compared to drying the same product with other solar drying methods reported in the literature. The drying time reduced by 18 h compared to freeze drying, 10 h compared to greenhouse drying, and 4 h compared to open sun drying (*Figure 1.2*). On the other hand, the drying time was nearly halved by using the hot air and infrared radiation techniques. However, from an energetic point of view, these last two techniques require high energy/cost, thus their efficiency is low. Therefore, using the ISDs is an optimal solution to strike a balance between the quality of the dried products and the energy/cost invested.

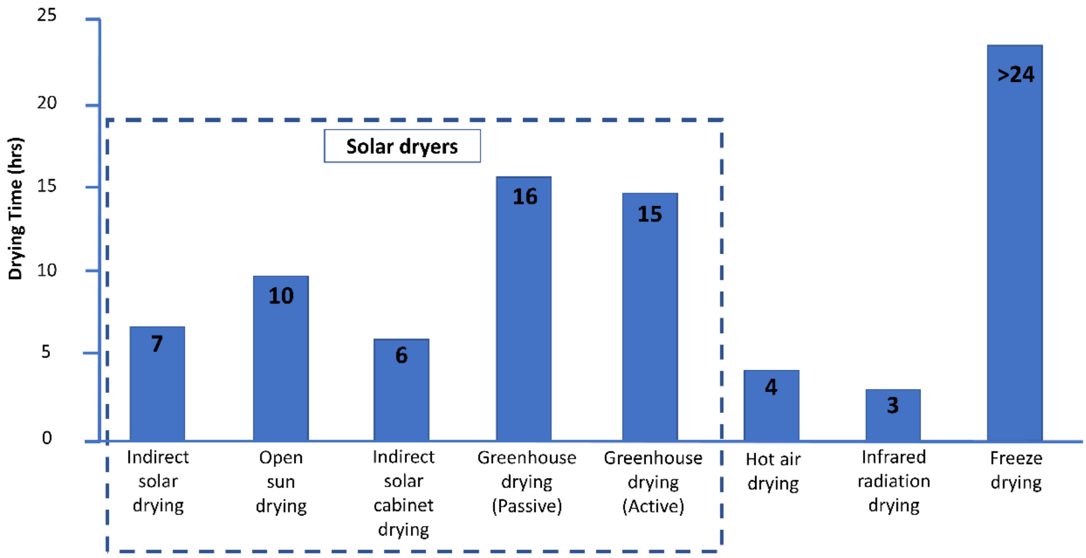

Figure 1.2 Comparison of drying time of bitter gourd slices (Vijayan, Arjunan, & Kumar, 2020).

4. Design of experiments and Response surface methodology

Design of experiments (DoE) is a collection of tools used for studying the behavior of a system. DoE, involves planning and performing a set of experiments to determine the effects of experimental variables on that system. The acquired data is separated into variation generated by the system itself and respective uncertainties or errors always present in empirical data. A statistically valid model is obtained, which by definition contains information on the effects of experimental conditions on the direction and magnitude of the measured response. The required experiments are also performed in a way that maximizes the information that can be extracted from a limited number of experiments. Once a satisfactory model has been determined, it can be used for predicting future observations within the original design range. DoE is thus useful for, not only studying, but also developing and optimizing a wide range of engineering systems. The method was originally developed by Fisher in the 1930s through factorial designs and analysis of variance for agricultural and biological research *(Mäkelä, 2017)*. Response surface methodology (RSM) was first discussed in the 1950s by Box and Wilson within chemical experimentation, and generally includes mathematical and statistical tools for both the design and analysis of response surfaces. In practice, the methods are today closely related and the use of RSM is without exception based on DoE. In this work, DoE is used to refer to practices included in both topics. DoE is closely related to the mentality of learning by experience and sequential experimentation. The effects and statistical significance of a larger group of experimental variables can be determined through factorial or screening designs, which enable choosing the relevant variables or conditions for the next set of experiments. DoE are constructed in a way that eliminates or minimizes correlations between the chosen variables. This allows independent estimation of variable effects and their potential interactions. Here lies an important advantage of DoE, as the variables are not varied one at a time while the others are being held constant. This approach assumes that the variables do not interact, i.e., the effect of one variable stays the same even though the others change. In many situations, this assumption can be unjustified.

Although DoE is useful in many areas of energy research, it has no natural connection to the studied system. What is obtained is a simple mathematical approximation of the response based on empirical data. More simple designs and models are often easier to interpret, which increases their value in practical situations. The chosen design also determines the level of detail and complexity that can be described with the subsequent model. Factorial designs can be used for quantifying linear and interaction effects, whereas RSM designs allow describing more complex behavior by including higher order model components *(Mäkelä, 2017)*.

5. Solar air heaters

Solar air heaters (SAHs) have been used at many processes for its availability and for saving energy especially for uses requiring low to moderate air temperatures. One of the most common applications in developing countries of SAHs is the drying of agro-products *(Vijayan, Arjunan, & Kumar, 2020)*. In many cases, SAHs are easy to exploit, simple and can be used far away from any energy supply centers. Reduced energy efficiency of SAHs has necessitated the researchers to focus on the enhancement of the thermal performances by providing design modifications in order to find the suitable geometric configuration. For this purpose, multiple techniques were used in previous works in order to boost the energy processes *(Arunkumar et al., 2020)*.

Among the different techniques of drying fruits and vegetables, the indirect solar dryer (ISD) is one of the best solutions as it allows better control of drying to achieve required temperature, retention of product color, nil damage to crops, and is therefore recommended for photo-sensitive materials like cucumber, papaya, lemon *(Lingayat et al., 2020)*. The principle of the ISD is that the food is heated indirectly through the air coming from the SAH. The main component of ISDs is the SAH, which has been widely used because of its simplicity, cheapness, and requiring minor maintenance cost. The SAH consists of transparent glass, absorber, and insulation to prevent the thermal losses. The absorber plate is made with black metal to absorb the solar radiation. Many types of materials have been used as insulation, such as conventional materials (e.g. glass wool *(Lingayat et al., 2020)*, polystyrene *(Sandali et al., 2017)*, and rockwool *(Kalaiarasi et al., 2020)*) or locally available bio-composite materials (e.g. date palm wood *(Nadir et al., 2019)*). At the absorber level, the solar irradiation is converted into heat energy then transferred to the air. Next, the hot air pulled up to the drying chamber by natural convection (passive mode) or using a fan (active mode). Finally, the thermal energy will be absorbed by the product which triggers the evaporation of the water inside it. Thereby, the reduction of water activity in the product increases the stability and reinforces the perishing resistance of the product. In this case, the dried product can be easily stored *(Abhay et al., 2018)*. Many review articles have been published by researchers and experts concerning design, applications and various other aspects of SAHs *(Evangelisti et al., 2019; Fudholi & Sopian, 2019; Hu & Zhang, 2019; Kabeel et al., 2017; Kalogirou et al., 2016; Saxena et al., 2015)*. Kabeel et al. *(Kabeel et al., 2017)* have published an exhaustive detailed review about design configurations and improvements in SAHs. The authors noted that there was still room to enhance SAH efficiencies taking into consideration the design cost and simplicity. Fudholi and Sopian *(Fudholi & Sopian, 2019)* summarized the studies conducted on SAHs that have been used as a pre-heater in ISDs. The authors focused on the energy–exergy analysis, economic analysis and environmental-economical aspect of SAHs.

5.1. Optimization of solar air heaters

Response Surface Methodology (RSM) is a widely used technique that characterizes the impact of test factors on output parameters (responses), identifies interrelationships among test factors and express the combined influence of all test factors in any response. Moreover, a good RSM design minimizes the number of experiments needed to acquire as much information as possible. Since nowadays physical experiments and numerical simulations are performed almost everywhere as a tool for studying and optimizing processes and systems, employing RSM is of significant importance in modern industry, science, and engineering.

In literature, many scientific contributions focused on the optimization of SAHs. Therefore, to identify the most frequently optimization techniques, a bibliometric analysis has been performed in the first stage focusing on SAHs optimization techniques used by researchers (to the author's knowledge, this analysis methodology has been applied yet in SAHs' research field). Furthermore, this kind of analysis is useful to see the specified research area from a macro perspective. This extensive bibliometric analysis can be visualized in terms of density map and as well as an overlay map, as presented in *Figure 1.3* and *Figure 1.4*, respectively. The data used in the analysis are based on 2,186 articles in the optimization of SAHs topic using data collection from relevant database by using the following searching formula: ("solar air heater" OR "solar air collector") AND "optimization". From the visualization of the research results using the VOSviewer tool *(van Eck & Waltman, 2010)*, it was observed that:

(1) The SAH is very useful tool in some specific applications like solar drying and distillation systems.
(2) The development of this type of technology by researchers is based on the optimization procedures since 2014 (*Figure 1.4*) However, *Figure 1.3* shows that previously, the advantages of RSM methodology and multi-objective optimization techniques are not widely used in SAHs development field but recently (from 2017 up to now), these methods have gained an increasing interest from researchers (*Figure 1.4*).
(3) Energy and exergy analysis are widely used by researchers however, it is remarqued that very limited research focused on exergy analysis such as improvement potential *(Nazri et al., 2019)*.

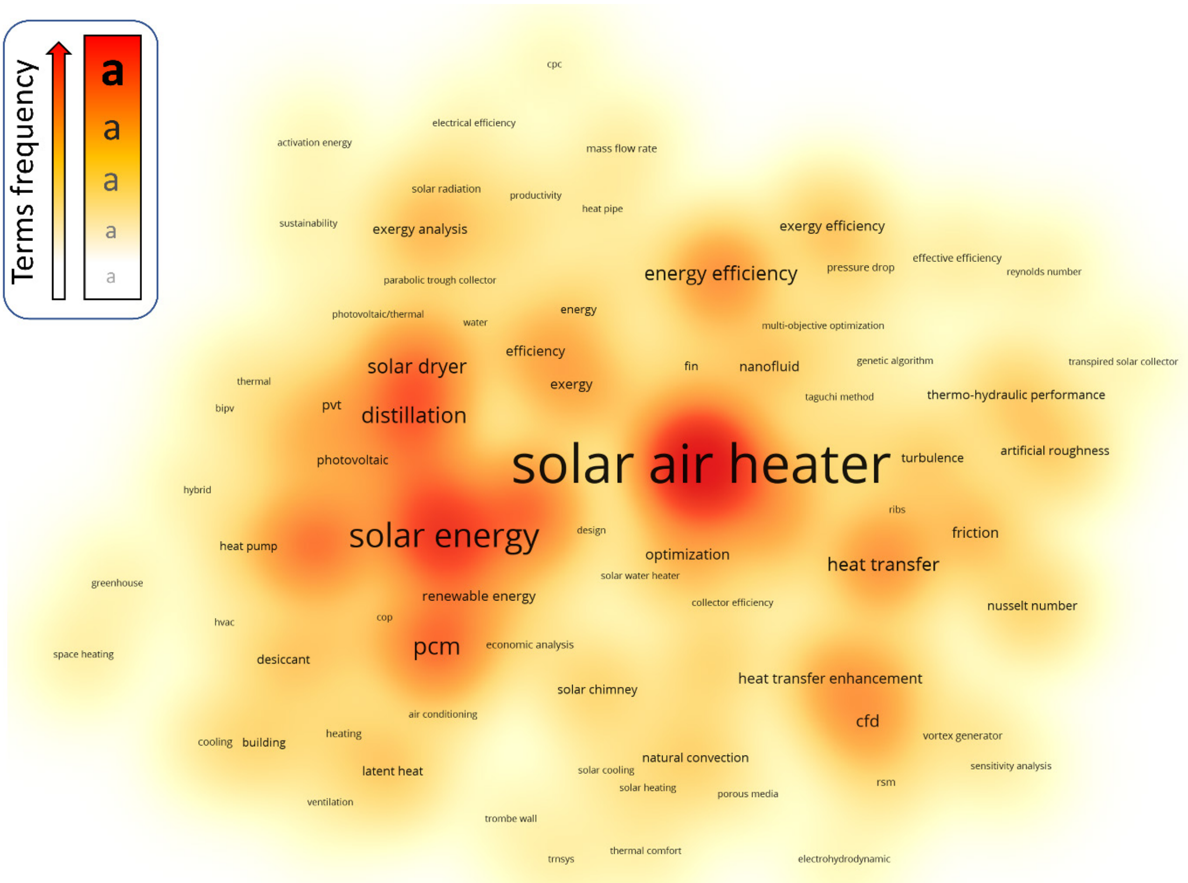

Figure 1.3 Density visualization map based of terms analysis. The most used terms are related to the intensity of red color of spots (nodes) and font size (as presented in the legend). The most used terms are with bold, big font size and highlighted with color near to red (e.g., solar air heater) and vice versa (e.g., multi-objective optimization).

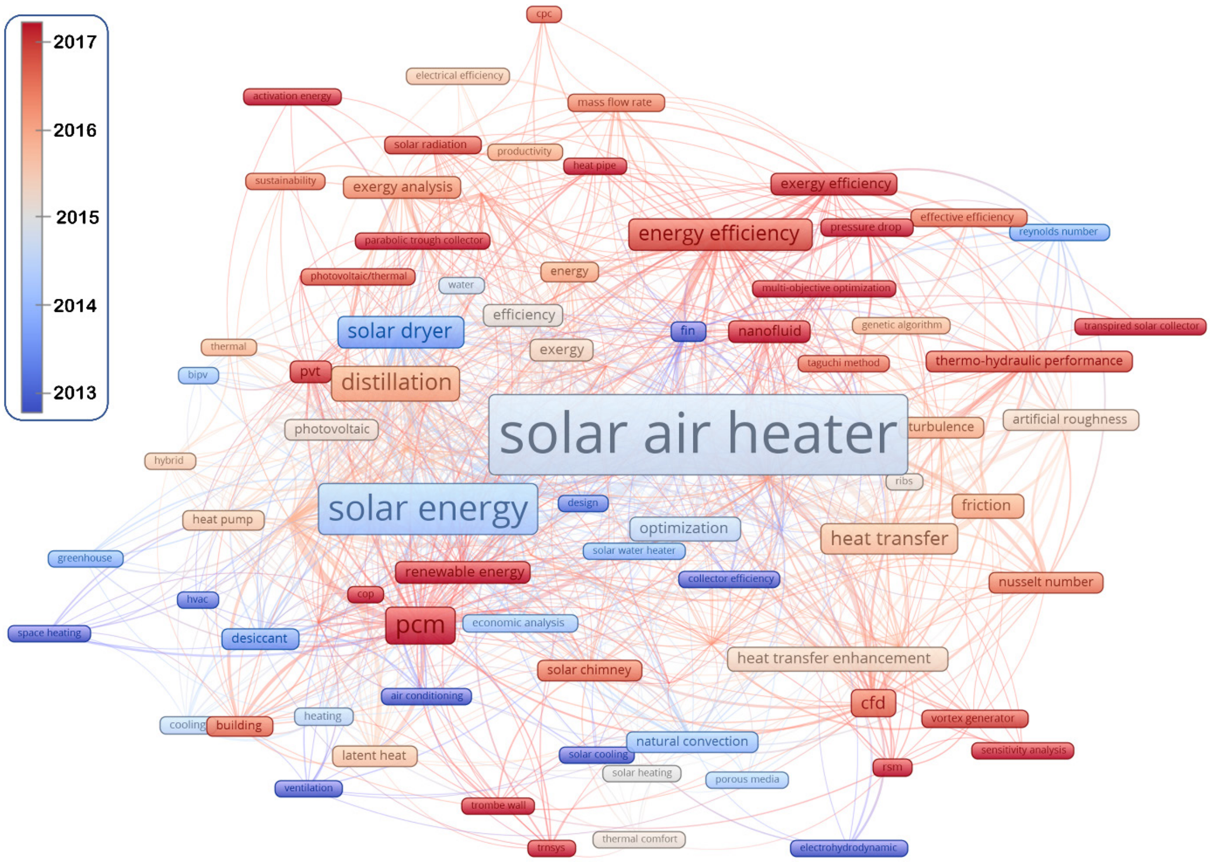

Figure 1.4 Visualization for the most used terms (in papers' titles, indexed keywords, and abstracts) based on the year of publication: For example: the red color, show the recent methods used for the optimization of solar air heaters are RSM and multi-objective optimization (from 2017 up to now), (For interpretation of the references to color in this figure legend, the reader is referred to the Web version of this article.).

RSM has been used by researchers for design optimization of SAHs. The following is a summary of major research which RSM is applied for optimization purpose. Singh et al. *(S. Singh & Dhiman, 2014)* used RSM to design the numerical experiments of double pass SAH in order to optimize the parameters to achieve the best performance and to investigate interaction between the studied parameters including channel depth between top glass covers, air mass flow rate, and recycle ratio. , closer studies have been investigated where the experiments (physical or numerical) are designed by using response surface methodology (RSM) in order to optimize SAHs thermal performances *(R. Kumar et al., 2019; Milani Shirvan et al., 2017; Qader et al., 2019; Tajdaran et al., 2020)*. Qader et al. *(Qader et al., 2019)* used CFD combined to RSM method for SAH optimization. The method has been used mainly to investigate inclined fins' geometrical parameters effect on the thermal and thermo-hydraulic performance. The experimental study was based on the investigation of the impacts of roughness elements shapes. A value of 3.85 was obtained as an optimum thermo-hydraulic performance. Tajdaran et al. *(Tajdaran et al., 2020)* used DoE coupled with CFD to optimize the geometry of the absorber plate of transpired SAH. This work utilized a formerly developed and validated CFD model to optimize the geometry of the absorber plate. The Heat Exchange Effectiveness (HEE) functions obtained through a 2^{nd} order regression model have been used to find the optimized geometry. The results showed that the optimized geometry demonstrated 43% increase in HEE. Kumar et al. *(R. Kumar et al., 2019)* used RSM for the evaluation and optimization of SAH's thermal performance. On the underside of absorber plate, multiple-arc shaped (three arcs) rib roughness is provided. The impact of different roughness elements on the thermal performance of the SAH was investigated and a remarkable improvement in thermal performance of the SAH was observed. The drawback was that varying roughness parameters led to increase the SAH pumping power. Kumar and Layek *(A. Kumar & Layek, 2019)* conducted an experimental study in order to maximize the thermo-hydraulic performance of the SAH. They adopted RSM to design the experiments and to optimize various roughness parameters. The results show the maximum thermo-hydraulic performance (2.13) was attained for optimum roughness parameter at Re = 21000, P/e = 8, α = 60° and y/e = 3. Kulkarni et al. *(Kulkarni et al., 2015)* applied three-dimensional CFD model in conjunction with the models of RSM and the Kriging models for multi-objective optimization of a SAH with obstacles. The CFD results were compared with experimental data of Bekele et al. *(Bekele et al., 2013)* in order to verify the accuracy of the numerical results. A very good agreement between the experimental and numerical data was obtained where the maximum and the minimum relative errors were 3.0% and 5.7% respectively. The design variables were the angle of attack, and the ratio of the transverse pitch to the base length of the obstacle, and height ratio of the obstacle to the duct. The main goal of the study was to find the best design variables that minimizes the friction factor and maximizes the average Nusselt number. Both RSM and the Kriging models exhibited good prediction accuracies for the objective functions, however, a better set of non-dominated results was obtained by the RSM model for a wide range of functional space. For better optimization of a system, exergy analysis should be taken into consideration by including an exergetic parameter as an objective function.

Although the RSM approach is interesting, best objective functions should be considered for the optimization. It is revealed from the above literature that absence of the exergy analysis and improvement potential (IP) in the objective functions used for optimization are the main limitations of these studies. The concept of exergetic IP is helpful and relevant in the analysis SAHs performances.

5.2. Improvement potential of solar air heaters

The following section summarizes some studies related to parametric studies on SAHs based on IP. Akpinar and Koçyiğit *(Ebru Kavak Akpinar & Koçyiğit, 2010)* experimentally evaluated the IP of four SAHs with different obstacles types and without obstacles. The results showed that adding obstacles in the SAH decreased the IP values. Dheep and Sreekumar *(Raam Dheep & Sreekumar, 2020)* studied the effect increased the convective heat transfer by modifying the absorber and the type of air flow inside the duct. Thermal analysis and impact of the flow rate on IP have been evaluated for mass flow rate varying between 30 - 90 kg/h.m^2. In another study, IP and SI values of a new drying system were calculated after performing an exergy analysis. As a novelty in the drying system, the infrared convective drying technology was combined with PV/T technology *(Arslan & Aktaş, 2020)*. In the refs. *(Ebru Kavak Akpinar & Koçyiğit, 2010; Arslan & Aktaş, 2020; Raam Dheep & Sreekumar, 2020)*, the authors have tested the effect of operating parameters on exergetic IP, all of the quoted works have utilized only the one-factor-at-a-time (OFAT) approach, which does not account the combined effects of these operating parameters *(Zeng et al., 2015)*. Nevertheless, in this type of studies, RSM would be a good alternative for studying and optimizing multivariable system also a good DoE helps to reduce cost and time of experiments. IP was also used to evaluate some SAH systems with thermal energy storage *(Atalay, 2019; Kalaiarasi et al., 2016)*. Kalaiarasi et al. *(Kalaiarasi et al., 2016)* tested the performances of two SAHs, conventional (type-I) and novel SAH with integrated sensible heat storage (type-II). The performance rating of the studied SAHs was based on energy-exergy analysis and IP. However, in this study also, the SI values were not calculated. Atalay et al. *(Atalay, 2019)* carried out a performance analysis of a solar drying system consists of SAH and a drying chamber integrated with the packed bed thermal energy storage. The energy-exergy performances, IP and other sustainability indicators of the system were analyzed, and the value of the IP was reported to be higher during the experiments performed using TES system.

Fudholi et al. *(Fudholi et al., 2013)* carried out a numerical study with an experimental validation of finned double-pass SAH. The authors reported that no information on the IP of SAHs is available. The thermal performance and IP of the SAH have been evaluated. Mugi and Chandramohan *(Mugi & Chandramohan, 2020)* reported that very few data are available on exergy analysis of SAH in ISD as it gives the available energy and it needs to be estimated to achieve suitable temperature for effective drying. In another recent study, Nazri et al. *(Nazri et* *al., 2019)* stated that very limited data currently exist regarding the exergetic IP of solar energy systems.

The detailed literature survey revealed that the useful RSM approach showed good results in multi-objective optimization of SAHs but the most cited studies tended to focus on energy analysis and disregarded exergy analysis. Moreover, it has been observed that, although the exergy analysis and the concept of an exergetic improvement potential (IP) are very useful tool for analyzing systems or processes more efficiently, currently very limited data exist considering the IP of solar energy systems *(Fudholi et al., 2013; Mugi & Chandramohan, 2020; Nazri et al., 2019)*.

6. Drying uniformity enhancement

6.1. Bibliometric analysis and literature review

The quality of the dried products varies significantly with the uniformity of velocity and temperature distribution in the drying chamber. Accordingly, optimizing the operating conditions and the dryer design has a significant importance to improve the drying uniformity. Moreover, the challenging step in the construction of a new solar dryer design or even in the renovation of old solar dryers is achieving a design with uniform airflow distribution. Hence, in parametric studies high number of experiments is needed to obtain the best SD design, these experiments are time-consuming and not efficient from an economic point of view.

To easily identify the shortcomings in the literature after best analysis and visualization of scientific papers published in literature concerning the uniformity of the dried products inside solar dryer (which is related to the air distribution), the authors performed an extensive bibliometric analysis based on 978 documents (original and review papers, book chapters and conference papers) collected by searching the words “Solar dryer and distribution” on the Scopus database with last access on February 21, 2021. Moreover, one of the benefits of such type of analysis is to determine the most relevant methodologies that have been used by researchers in any specific field. In this bibliometric study, data analyses were performed using an open-source software (VOSviewer -V 1.6.16) *(van Eck & Waltman, 2010)* that allows to generate and visualize bibliometric networks based on the links between different items of research publications.

In this analysis the link between items was been in terms of co-occurrence links *(Sultan et al., 2021)*. the results of the co-occurrences of author keywords are displayed in a network visualization in which each author keyword is represented by a colored spot with a size proportional to its weight expressed in terms of the number of occurrences or link strength which means that the most used terms are with bold, big font size and are inside big spots (e.g., drying) and vice versa (e.g., solidification) (*Figure 1.5*). The colors belong to the cluster on which the different items are grouped and the space between two spots is proportional to the relationship between the keywords.

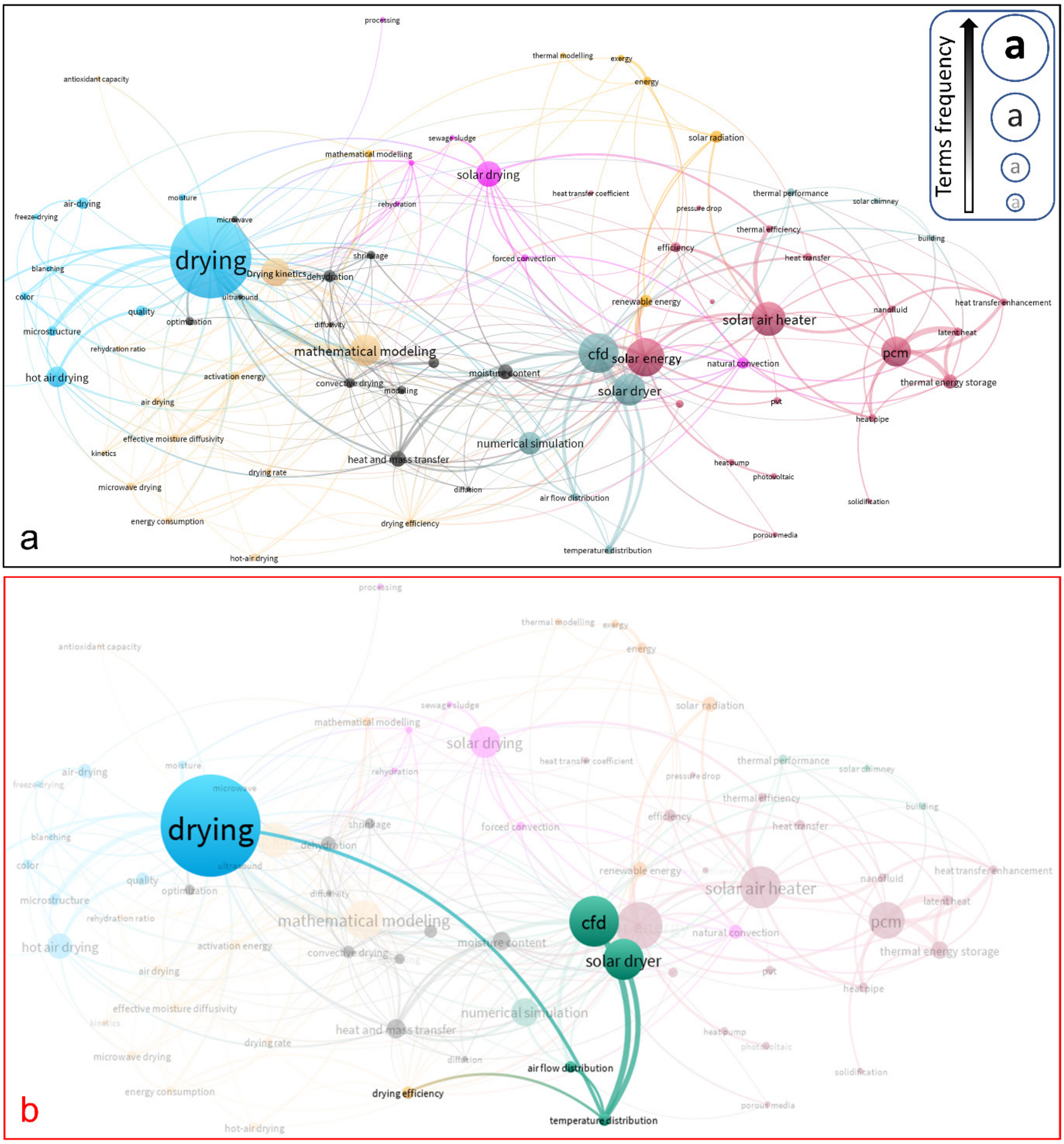

Figure 1.5 a) Network visualization of author keywords on "Solar dryer and distribution" elaborated with VOSviewer. b) Co-occurrence and link of the keywords "temperature distribution". The most used terms are related to the diameter of the spots (nodes) and font size (as presented in the legend).

By analyzing the obtained results in *Figure 1.5*, we observed that seven main clusters are presented, Cluster 1: PCM, thermal energy storage, solar air heater, pvt; Cluster 2: Drying kinetics, mathematical modeling, activation energy, kinetics, drying rate, micro-wave drying. Cluster 3: heat and mass transfer, diffusion, moisture content, convective drying, shrinkage temperature; Cluster 4: Drying, quality, color, quality, air-drying, moisture, antioxidant activity. Cluster 5: CFD, Solar dryer, numerical simulation, air flow distribution, temperature distribution, thermal performance, building; Cluster 6: Solar drying, forced convection, natural convection, rehydration, sewage sludge; Cluster 7: Renewable energy, solar radiation, energy, exergy.

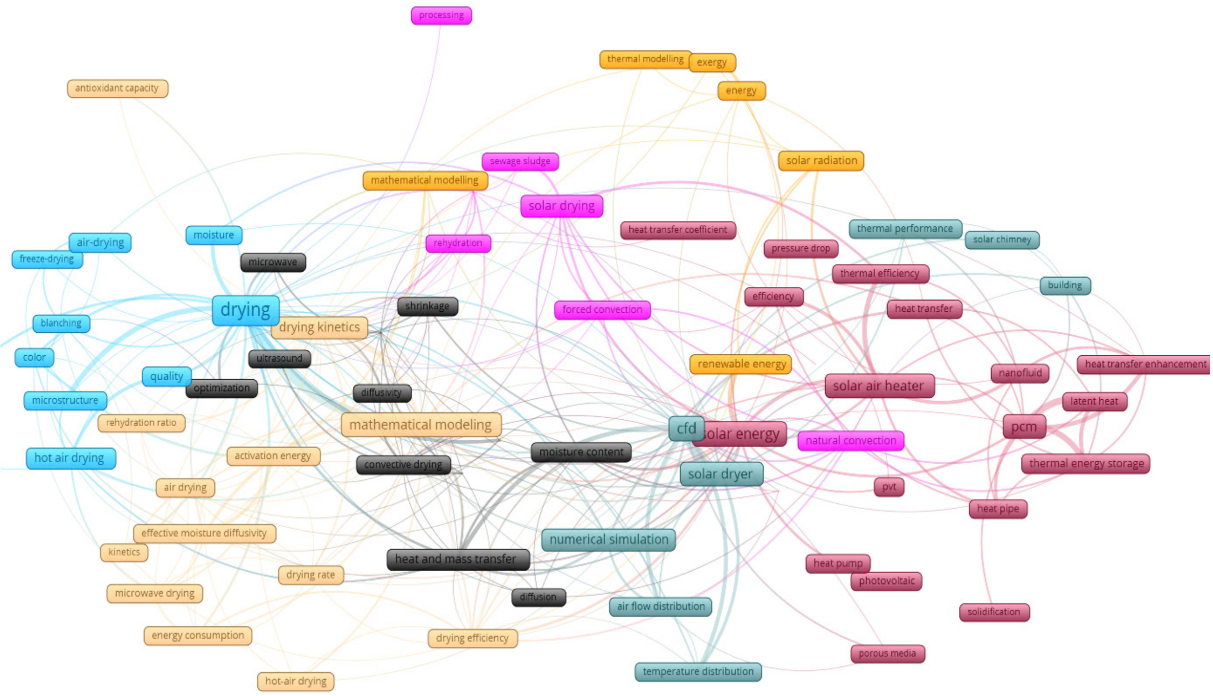

Figure 1.6 Network visualization for the most used words (in papers' title, indexed keywords and abstract). Note: the most used words are classified into four clusters identified by colors. Each cluster includes words that belong to a particular topic.

After analyzing data obtained from VOSviewer, we can observe that numerical simulation and particularly CFD are the most used techniques to study the distribution of air inside the solar dryers because the spot of word CFD is very closed to the spot of the word solar dryer also there is strong (*Figure 1.5*). Furthermore, In terms of numerical simulation, the literature survey indicates that numerous previous numerical studies were performed in order to improve solar dryers' efficiency while the main utilizations of CFD were: i) designing and predicting the airflow temperature distribution within the drying chamber in ISDs *(Chaatouf et al., 2021; Demissie et al., 2019; Khaldi et al., 2017a; Khaldi et al., 2017b)*, ii) studying the effect of the geometric configuration of cabinet dryers *(Amanlou & Zomorodian, 2010; Darabi* *et al., 2015; Ghaffari & Mehdipour, 2015; Lokeswaran & Eswaramoorthy, 2013)*, and iii) improving cabinet solar dryer performances *(Ghaffari & Mehdipour, 2015; Messaoud Sandali et al., 2019)*. Other works have studied the uniformity in the drying chamber. Jain et al. *(Jain et al., 2019)* designed a passive mode domestic solar dryer based on CFD analysis, where ANSYS Fluent 14.0 software was used to design the multi-shelf type solar dryer for domestic use. The numerical simulation and energy analysis were validated using the experimental approach and a 328 K air temperature was achieved inside the dryer. The payback time and carbon credit obtained from the evaluation of energy analysis were 7 years and INR 2055, respectively. In order to study the corn drying process in an ISD, a dynamic numerical model based on CFD has been developed by Sanghi et al. *(Sanghi et al., 2017)*. The developed model allowed drying uniformity visualization where the velocity, temperature, and humidity distributions were verified inside the drying chamber. The simulation study captured, with a good accuracy, the observed stagnation in the airflow of the experimental survey. Güler et al. *(Güler et al., 2020)* counted on a CFD model to design and analyze the effect of using mesh absorber modification in an ISD. The main aim of the study was to improve the energy efficiency of the SAH by integrating iron meshes. As a result, the optimal value of the average dryer efficiency was found to be 23.08%, which was obtained using the dryer with mesh absorber. Four drying chamber designs have been evaluated theoretically for drying leaves using CFD with ANSYS FLUENT software as a working tool in *(Babu et al., 2019)*. After analyzing results, the optimal design that generated a uniform air distribution has been selected. The authors confirmed that the CFD procedure can be employed for evaluating the performance of any similar system. In all the reviewed papers, a good agreement between numerical and experimental results was mentioned by authors. From these aforementioned literature and based on the bibliometric analysis we can conclude that CFD can be the key to optimize the geometric shape and operating parameters with low cost and reduced time compared to physical experiments. Moreover, the new aspect proposed in the current study is to use image processing technique side to side with CFD in order to study and enhance the drying uniformity in solar dryers.

7. Conclusion

Throughout this chapter which collects the different technologies used by researchers to improve the solar dryer designs and enhance the uniformity of the dried products. The shortcomings in the solar drying systems have been highlighted by an extensive bibliometric analysis. Mainly indirect solar dryer type is selected in this thesis as optimal solution to strike a balance between the quality of the dried products and the energy/cost invested. Moreover, the most relevant methodologies that have been used by researchers to develop the solar drying systems are described.

CHAPTER 2 OPTIMIZATION OF SOLAR AIR HEATER FOR DRYING APPLICATIONS

1. Introduction

The detailed literature survey (Chapter 1) revealed that the useful RSM approach showed good results in multi-objective optimization of SAHs but the most cited studies tended to focus on energy analysis and disregarded exergy analysis. Moreover, it has been observed that, although the exergy analysis and the concept of an exergetic improvement potential (IP) are very useful tool for analyzing systems or processes more efficiently, currently very limited data exist considering the IP of solar energy systems *(Fudholi et al., 2013; Mugi & Chandramohan, 2020; Nazri et al., 2019)*. The main objectives of this chapter are:

(1) to develop and experimentally verify the MATLAB code that is used to solve energy and exergy balance equations then to predict drying air temperature, energy-exergy performance, and IP of the finned SAH.

(2) to investigate the effects of aspect ratio (L/W), air duct height, and number of fins on the thermal performance and IP of SAH using second order quadratic equation for outlet temperature, energy efficiency, and IP developed by RSM.

(3) to apply the combined approach of the experimentally validated analytical model and RSM in order to find the optimum design parameters that yield to the best thermal performances of a finned SAH used for drying application.

(4) to perform a multi-objective optimization of SAHs' design for food drying using RSM and regarding three objective functions; namely, thermal efficiency, outlet temperature, and exergetic IP.

(5) to evaluate the IP and sustainability index of the SAH which describe the exergy loss per unit exergy inflow.

2. Materials and methods

2.1. Experimental configuration

The present indirect solar dryer (ISD) was constructed and installed at the laboratory of Control and Computing for Intelligent Systems and Green Energy, Cadi Ayyad University, (Marrakesh, Morocco 31.6°N, 8.0°W). The ISD consists of two main parts: (i) SAH with finned absorber (L=2 m and W=1 m) and (ii) drying chamber where food products are kept on trays. A picture of the test rig is presented in *Figure 2.1*.

Figure 2.1 A picture of the experimental setup.

The SAH is oriented to south and connected to drying chamber at an angle equal to the latitude of the location (i.e 31° with the horizontal) to receive the maximum solar radiation. It consists of a glass cover, absorber plate, and an insulation layer. The absorber is black coated absorber plate made with aluminum to receive maximum amount of solar radiation (absorptivity of 0.95 and emissivity of 0.8). 24 fins are used to extend the surface of contact between the absorber and the flowing air. The fins are longitudinal and parallel, where this type of arrangement is used instead of transversely one to avoid high-pressure drops. The glass cover is with 0.3 cm thick, placed at 5 cm above the absorber in order to reduce the heat loss from the top. The bottom and sides of the SAH are covered with insulation material (4 cm of glass wool) to reduce the thermal energy loss to the ambient. The arrangements of the glass cover, the absorber plat, the insulation material, and the air flow direction are clearly presented in the cross-sectional view of the SAH (*Figure 2.2*).

The drying chamber has a cubic shape (1 m^3) that made from galvanized iron sheet and thermally insulated using 4 cm of glass wool. Usually in a full drying process, the products to be dried are entered through the door (in the back side) then distributed on four galvanized steel mesh trays installed inside the chamber. The hot air coming from the outlet of SAH, passively or by active mode (using a fan), motivate the evaporation of the moisture from the products. Thereby, the reduction of water activity in the dried products increases the stability and reinforces the perishing resistance of the product. A chimney is installed on the drying chamber with an electrical fan used to force the air movement (employed only in the active mode).

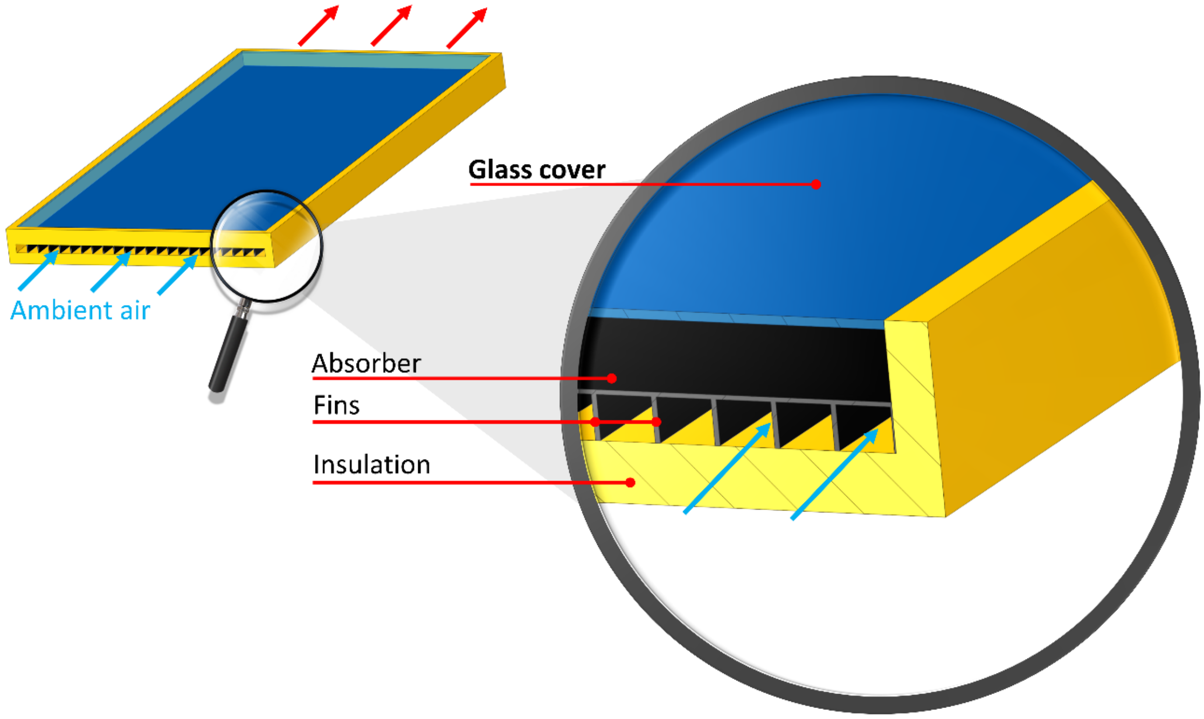

Figure 2.2 Cross sectional view of the SAH.

A data acquisitor, laptop, local weather station, pyranometer, and thermocouples are used for data acquisition during the experiments (*Figure 2.3*). The PT100 type (ref. TM110, KIMO) thermocouples with ±0.5°C of accuracy were used for temperature measurement at the inlet and outlet of the SAH. In order to measure the solar radiation, a pyranometer (Kipp & Zonen SMP10) with a sensitivity of 14.69×10^{-3} mV and uncertainty <1.2 for 1000 W/m², was connected to the test setup and inclined at the same angle of SAH. Weather data such as ambient temperature and wind velocity were measured employing (Wireless Vantage Pro2 ref. 6162CFR) weather station. The accuracy of the station is ± 1°C and ± 0.9 m/s, respectively, for the temperature and velocity sensors.

The experimental tests were performed under passive and active mode for $\dot{m}$ = 150 m^3/h, respectively (20th and 21st September 2019). During the two days of experiments, data for all of the instruments were recorded every 30 min from 10:00 to 16:00 using a data acquisition platform including an automate type cRIO-9030, and a PC.

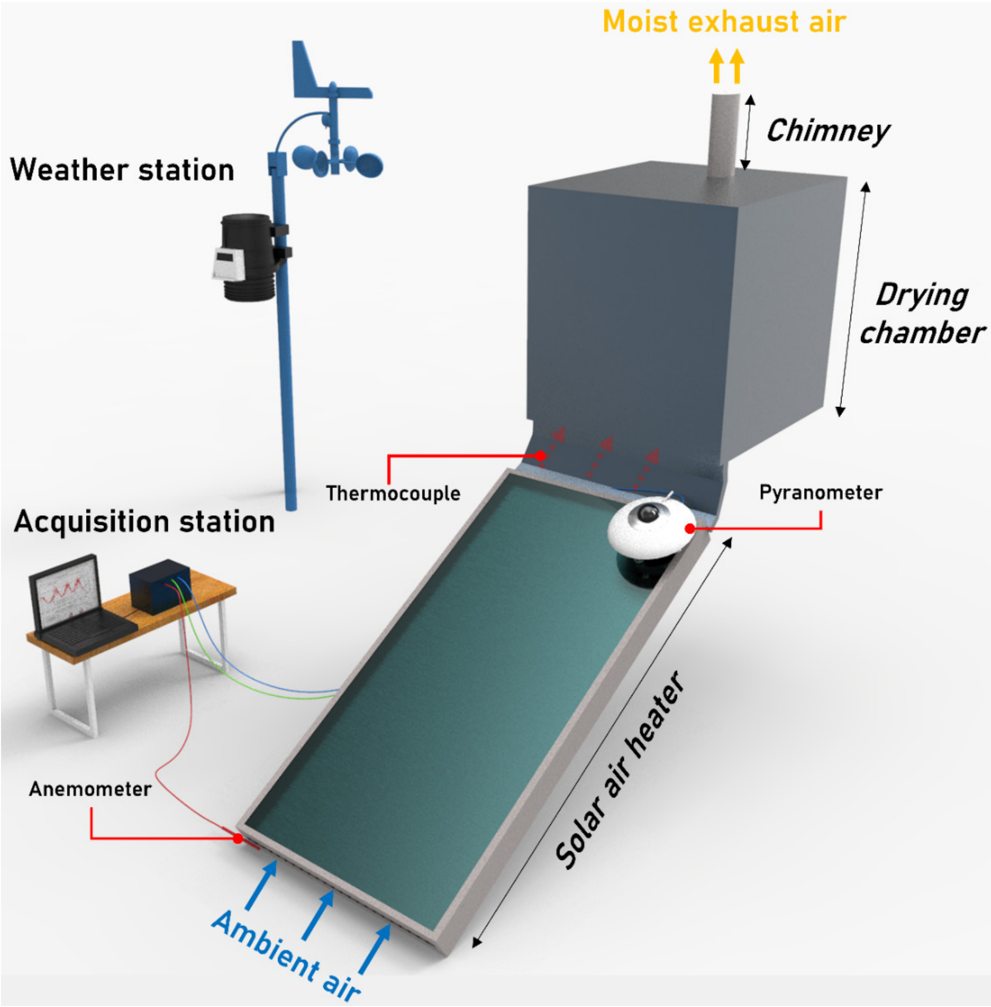

Figure 2.3 Schematic diagram of the experimental setup.

2.1.1. Uncertainty analysis

Errors and uncertainties occur in tests due to the collection of instruments, calibration, observations, environmental factors, preparation of tests and measurements. During the experimental tests, operating temperatures, wind speed, solar radiation were calculated using suitable instruments. The result R is a function offered in the form of independent variables. Let W_R be the uncertainty in the outcome and W_1, W_2, … W_n be the uncertainties in the independent variables. This function can only be used if the uncertainty in independent variables is given with the same oddity:

$$W_R = \left[\left(\frac{\partial R}{\partial x_1} W_1\right)^2 + \left(\frac{\partial R}{\partial x_2} W_2\right)^2 + \ldots \left(\frac{\partial R}{\partial x} W_n\right)^2\right]^{1/2} \qquad 2.1$$

During the experiments, the measured parameters' uncertainties are presented in Table 2.1 (more details of calculation procedure is presented in Appendix A). It is observed that all uncertainties were in an acceptable range.

Table 2.1 Uncertainties of the measurement sensors.

	Unit	Uncertainty
Solar radiation	$W.m^{-2}$	± 1.22
Inlet temperature	°C	± 0.59
Outlet Temperature	°C	± 0.59
Ambient temperature	°C	± 0.59
Air velocity	m/s	± 0.283
Wind Speed	m/s	± 0.92

2.2. Description of theoretical model

The assumptions made in the proposed model are as follows:

i. Temperature of the considered system varies only in drying air direction (*x axis)*, i.e*.,* the temperature variation along *y* direction is neglected (see *Figure 2.4*).
ii. Temperature variation in the same component is negligible.
iii. Heat loss from the SAH edges is ignored *(Duffie & Beckman, 2013)*.
iv. The properties of the solid components are constant.
v. Solar flux is a function of time.
vi. There is no air leakage to or from the system.

The variation of solar radiation flux (G) over time measured during the experiments has been included as a distributive function. For the mathematical modeling, five collector components have been selected namely, glass cover (g), air gap between the absorber and glass (ga), finned absorber plate (abs), flowing air (fluid), and insulation (ins). Total numbers of nodes are 6×N where N nodes are in the *x* direction (*Figure 2.4*).

2.2.1. Energy balance equations

The energy balance equation of each component in the SAH can be described as *(Pérez-Espinosa et al., 2020)*:

$$\rho\delta C\frac{dT}{dt}=q_i-q_o+q_{gen} \quad (2.2)$$

The expression dT/dt indicates the temperature (T) variation over time (t). q_i, q_o and q_{gen} denote respectively inlet, outlet and generated heat flux per unit of area in each control volume.

The multilayer method established by Cadafalch *(Cadafalch, 2009)* was used in the present numerical study. In the analytical model, a glass layer is placed on the top of absorber. The gap between the absorber and glass is filled with air. Below the absorber, there is a flow channel which is thermally insulated by an insulation material. The schematic frontal view of the SAH is presented in *Figure 2.4*. The ambient air enters through the air duct from the front side in *x* direction. Afterwards it flows through the duct, where it acquires heat from the absorber and fins, then it gets out from the other side in the same direction. The air duct is divided into several (n_f-1) sub-ducts by n_f number of fins.

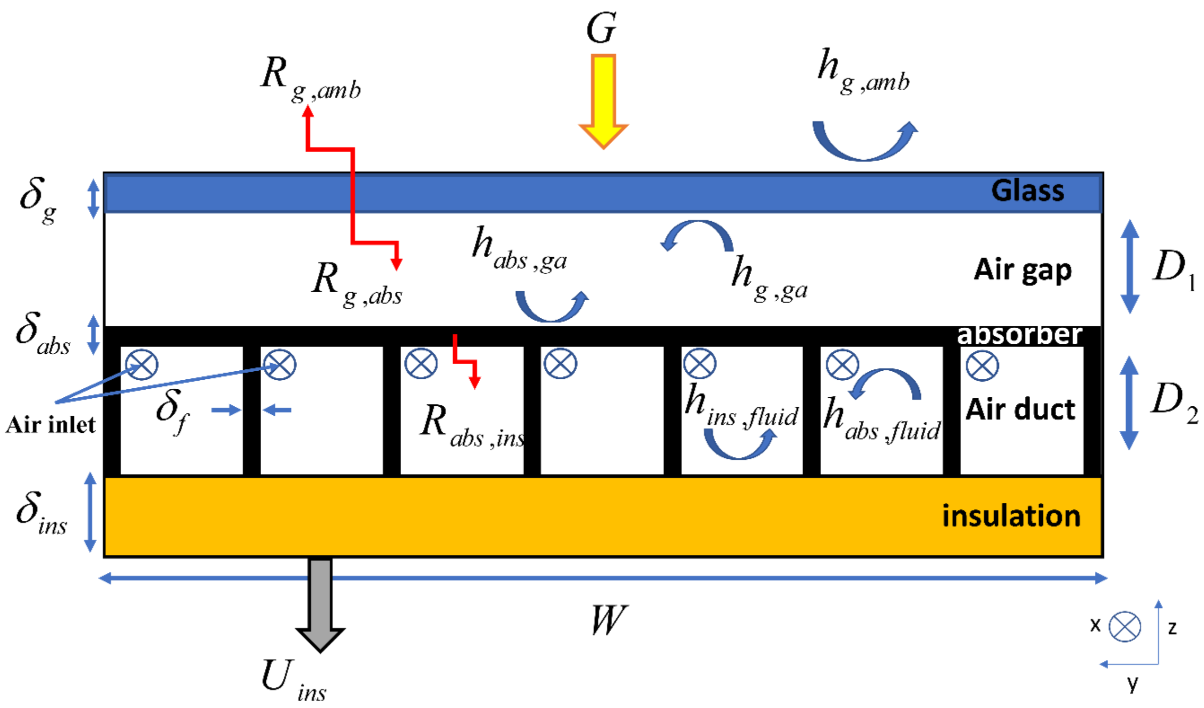

Figure 2.4 Schematic drawing of SAH cross section.

The energy balance equations for different layers are expressed below:

For the glass:

$$\rho_g V_g C_g \frac{dT_g}{dt} = \left[\alpha_g G + h_{g,amb}(T_{amb} - T_g) + h_{g,ga}(T_{ga} - T_g) + R_{g,abs}(T_{abs} - T_g)\right] W\,\Delta X \qquad 2.3$$

For the air gap:

$$\rho_{ga} V_{ga} C_{ga} \frac{dT_{ga}}{dt} = \left[h_{g,ga}(T_g - T_{ga}) + h_{abs,ga}(T_{abs} - T_{ga})\right] W\,\Delta X \qquad 2.4$$

For the finned absorber:

$$\rho_{abs}(D_2\delta_f n_f + \delta_{abs}W)C_{abs}\frac{dT_{abs}}{dt} = \alpha_{abs}\tau_g GW + h_{abs,ga}(T_{ga} - T_{abs})W + R_{g,abs}(T_g - T_{abs})W \\ + h_{abs,fluid}(T_{fluid} - T_{abs})(2D_2(n_f - 1)F + W) + R_{abs,ins}(T_{ins} - T_{abs})W \quad 2.5$$

For the air duct:

$$\rho_{fluid}\delta_{fluid}C_{fluid}W\frac{\partial T_{fluid}}{\partial t} = (W + 2D_2(n_f - 1)\eta_f)h_{abs,fluid}(T_{abs} - T_{fluid}) \\ + Wh_{ins,fluid}(T_{ins} - T_{fluid}) - \dot{m}C_{fluid}\frac{\partial T_{fluid}}{\partial x} \quad 2.6$$

For the insulation:

$$\rho_{ins}V_{ins}C_{ins}\frac{dT_{ins}}{dt} = \begin{bmatrix} R_{abs,ins}(T_{abs} - T_{ins}) + h_{ins,fluid}(T_{fluid} - T_{ins}) \\ + U_{ins}(T_{amb} - T_{ins}) \end{bmatrix} W\,\Delta X \quad 2.7$$

Heat transfer from the absorber to the drying air is calculated by Eq. (2.8) *(Bennett & Myers, 1982)*.

$$\phi_{abs,fluid} = \left[1 + \frac{A_{f,fluid}}{A_{abs,fluid}}\eta_f\right]h_{abs,fluid}A_{abs,fluid}(T_{abs} - T_{fluid}) \quad 2.8$$

In the above equation, $A_{abs,fluid}$ is the contact surface of the absorber with the drying airflow, $A_{f,fluid}$ is the contact surfaces of fins with the drying air. η_f is the efficiency of fins which is estimated by Eq. (2.9) *(Yeh, 2012)*.

$$\eta_f = \tanh\left(D_2\sqrt{\frac{2h_{abs,fluid}}{k_f\,\delta_f}}\right)\Big/\left(D_2\sqrt{\frac{2h_{abs,fluid}}{k_f\,\delta_f}}\right) \quad 2.9$$

2.2.2. Heat transfer coefficients

The proposed formula by Duffie and Beckman *(Duffie & Beckman, 2013)* was used to approximate the radiative heat transfer coefficient between the SAHs' components. The radiation coefficients between pair of glass and absorber, absorber and insulation, and glass and sky are respectively calculated by the following expressions:

$$R_{g,abs} = \frac{\sigma(T_{abs} + T_g)(T_{abs}^2 + T_g^2)}{\frac{1}{\varepsilon_{abs}} + \frac{1}{\varepsilon_g} - 1} \quad 2.10$$

$$R_{abs,ins} = \frac{\sigma(T_{abs} + T_{ins})(T_{abs}^2 + T_{ins}^2)}{\frac{1}{\varepsilon_{abs}} + \frac{1}{\varepsilon_{ins}} - 1} \quad 2.11$$

$$R_{g,amb} = \frac{\sigma\varepsilon_g (T_g^4 - T_s^4)}{(T_{amb} - T_g)} \quad 2.12$$

where T_s stands for the clear sky temperature and predicted by the correlation of Swinbank *(Swinbank, 1963)*:

$$T_s = 0.0552\, T_a^{1.5} \quad 2.13$$

The convective heat transfer coefficient between the glass and ambient is calculated according to McAdams relation *(McAdams, 1954)*. It is given by Eq. (2.14):

$$h_{g,amb} = 5.67 + 3.86\, W_v \quad 2.14$$

The heat transfer coefficient of the insulation layer is calculated as follows:

$$U_{ins} = k_{ins} / \delta_{ins} \quad 2.15$$

The convective heat transfer coefficient between the SAHs' components is determined by Eq. (2.16):

$$h_{i,k} = Nu.k/D \quad 2.16$$

where D denotes the distance between the elements of SAH and Nu expresses Nusselt number which is calculated by the following correlation *(Hollands et al., 1976)*:

$$Nu = 1 + 1.44\left[1 - \frac{1708}{Ra\cos\theta}\right]^{+}\left(1 - \frac{(\sin 1.8\theta)^{1.6} 1708}{Ra\cos\theta}\right) + \left[\left(\frac{Ra\cos\theta}{5830}\right)^{\frac{1}{3}} - 1\right]^{+},\ Ra < 10^5,\ 0 < \theta < 70°,\ H/L \geq 12 \quad 2.17$$

In the above equation, Ra represent Rayleigh number and is defined as follows:

$$Ra = \frac{g\,(1/T)\,\Delta T D^3}{\upsilon \alpha_d} \quad 2.18$$

The mass flow rate of air due to natural convection is calculated by the following expression *(Al-Kayiem et al., 2013)*.

$$\dot{m} = C_d \rho_{fluid} S_o \sqrt{\frac{2gL\sin(\theta)(T_{fluid,mean} - T_{amb})}{\left(1+\left(\frac{S_o}{S_i}\right)^2\right) T_{amb}}} \qquad 2.19$$

Here, S_o and S_i represent respectively the outlet and inlet air duct areas. $T_{fluid,mean}$ is the drying air mean temperature whereas C_d is the discharge coefficient and taken to be C_d =0.6, according to Flourentzou et al. *(Flourentzou et al., 1998)*.

2.3. Performance Parameters

2.3.1. Thermal efficiency

The useful energy gained from the SAH determines the thermal efficiency, where it depends mainly on solar radiation magnitudes and can be expressed as *(Sivakandhan et al., 2020)*:

$$\eta_{en} = \frac{\dot{m}\, C_{fluid}\,(T_o - T_i)}{L\, W\, I} \qquad 2.20$$

2.3.2. Exergy efficiency

The general exergy balance can be expressed as *(E. Kavak Akpinar, 2010; Kalogirou, 2004)*:

$$\sum Ex_{des} = \sum Ex_i - \sum Ex_o \qquad 2.21$$

or

$$Ex_{heat} - Ex_{work} + Ex_{mass,i} - Ex_{mass,o} = Ex_{dest} \qquad 2.22$$

Based on Eq. (2.22), the rate from general exergy balance can be expressed as:

$$\sum\left(1-\frac{T_{amb}}{T_{so}}\right)Q_s - W + \sum m_i \psi_i - \sum m_o \psi_o = Ex_{dest} \qquad 2.23$$

where,

$$\psi_i = (h_i - h_{amb}) - T\,(s_i - s_{amb}) \qquad 2.24$$

$$\psi_o = (h_o - h_{amb}) - T\,(s_o - s_{amb}) \qquad 2.25$$

By substituting Eqs. (2.24) and (2.25) into Eq. (2.23), we obtain

$$\left(1-\frac{T_{amb}}{T_{so}}\right)Q_s - m\left[(h_o - h_i) - T_{amb}(s_o - s_i)\right] = Ex_{dest} \quad 2.26$$

where, Qs presents the quantity of energy absorbed.

$$\left(1-\frac{T_{amb}}{T_{so}}\right)Q_s - m\left[(h_o - h_i) - T_{amb}(s_o - s_i)\right] = Ex_{dest} \quad 2.27$$

Enthalpy and entropy variations of the drying air are expressed respectively as:

$$h_o - h_i = C_{fluid}(T_{out} - T_{in}) \quad 2.28$$

$$s_o - s_i = C_{fluid}\ln\frac{T_{out}}{T_{in}} - R_s\ln\frac{P_{out}}{P_{in}} \quad 2.29$$

Here, P_{in} and P_{out} are the air pressure at the inlet and outlet of SAH, respectively, and R_s is air gas constant (287.058 $J.kg^{-1}.K^{-1}$).

By substituting Eqs. (2.28) and (2.29) into Eq. (2.27), we obtain

$$\left(1-\frac{T_{amb}}{T_{so}}\right)Q_s - mC_{fluid}(T_o - T_i) + mCT_{amb}\ln\frac{T_o}{T_i} - mRT_{amb}\ln\frac{P_o}{P_i} = Ex_{des} \quad 2.30$$

Exergy destruction (Ex_{des}) may be expressed as:

$$Ex_{des} = T_{amb}S_{gen} \quad 2.31$$

By substituting Eq. (2.30) into Eq. (2.31) and disregarding the pressure drop that occurs in the SAH, the entropy generation rate (S_{gen}) is obtained as

$$S_{gen} = \left(\frac{1}{T_{amb}} - \frac{1}{T_{amb}}\right)Q_s + \left[\ln\frac{T_o}{T_i} - \frac{T_o}{T_{amb}} + \frac{T_i}{T_{amb}}\right]mC_{fluid} \quad 2.32$$

To evaluate and optimize energy systems, exergy efficiency is a paramount criterion that can be used. Exergy defines the maximum useful work which can be produced from a system as it reversibly comes into equilibrium with its environment. The exergy efficiency of SAH was evaluated by *(Fudholi & Sopian, 2019)*:

$$\eta_{ex} = 1 - \frac{T_{amb}S_{gen}}{\left(1-\frac{T_{amb}}{T_{so}}\right)(\tau\alpha)LWI} \quad 2.33$$

where, solar temperature T_{so} is taken 5600K.

2.3.3. Improvement potential (IP)

To increase the exergy efficiency of a system or a process, the exergy loss (Ex_{loss}) should be reduced. Exergetic 'improvement potential' (IP) is a useful concept to analyze systems or processes efficiently. For this purpose, we have chosen to use improvement potential as an objective function in the optimization process. IP is described as *(E. Kavak Akpinar, 2010; Fudholi et al., 2013)*:

$$IP = (1-\eta_{ex})Ex_{loss} \tag{2.34}$$

$$Ex_{loss} = Ex_i - Ex_o \tag{2.35}$$

Sustainability analysis is applied using sustainability index (SI) method. The sustainability index of the SAH is obtained through Eq.(2.36) as follows *(Tuncer et al., 2020)*:

$$SI = \frac{1}{1-\eta_{ex}} \tag{2.36}$$

2.4. Numerical solution of the mathematical modeling

The energy balance equations Eqs. (2.3 – 2.7) were solved after discretization of the differential forms using the finite difference method. After equations rearrangement in a matrix form, the time leveled implicit method was used in the solving process. The derivative of temperature over time is solved by forward difference scheme, while the derivative of temperature over position is solved using backward difference scheme. The stability criterion is presented in Eq. (2.44).

$$\frac{dT_m}{dt} = \frac{T_{m,j}^{t+\Delta t} - T_{m,j}^{t}}{\Delta t} \tag{2.37}$$

$$\frac{dT_{fluid}}{dz} = \frac{T_{fluid,z}^{t+\Delta t} - T_{m,z-1}^{t}}{\Delta z} \tag{2.38}$$

2.4.1. Temperature of different components of the SAH

The temperatures of SAH' components are determined by replacing the derivatives shown in Eq. (2.37) and (2.38) by their differential forms in the Eqs. (2.3) – (2.7). So, these equations can be rewritten as follows:

$$T_{g,j}^{t+\Delta t} = \frac{T_{g,j}^{t}}{Y_1\,\Delta t} + \frac{F_1}{Y_1}T_{amb,j}^{t+\Delta t} + \frac{F_2}{Y_1}T_{abs,j}^{t+\Delta t} + \frac{F_3}{Y_1}T_{ga,j}^{t+\Delta t} + \frac{F_4}{Y_1} \tag{2.39}$$

$$T_{ga,j}^{t+\Delta t} = \frac{1}{Y_2 \Delta t} T_{ga,j}^{t} + \frac{F_5}{Y_2} T_{g,j}^{t+\Delta t} + \frac{F_6}{Y_2} T_{abs,j}^{t+\Delta t} \quad 2.40$$

$$T_{abs,j}^{t+\Delta t} = \frac{1}{Y_3 \Delta t} T_{abs,j}^{t} + \frac{F_7}{Y_3} T_{fluid,j}^{t+\Delta t} + \frac{F_8}{Y_3} T_{g,j}^{t+\Delta t} + \frac{F_9}{Y_3} T_{ga,j}^{t+\Delta t} + \frac{F_{10}}{Y_3} T_{ins,j}^{t+\Delta t} + \frac{F_{11}}{Y_3} \quad 2.41$$

$$T_{fluid,j}^{t+\Delta t} = \frac{1}{Y_4 \Delta t} T_{fluid,j}^{t} + \frac{F_{12}}{Y_4} T_{abs,j}^{t+\Delta t} + \frac{F_{13}}{Y_4} T_{ins,j}^{t+\Delta t} + \frac{F_{14}}{Y_4} T_{fluid,j-1}^{t+\Delta t} \quad 2.42$$

$$T_{ins,j}^{t+\Delta t} = \frac{1}{Y_5 \Delta t} T_{ins,j}^{t} + \frac{F_{15}}{Y_5} T_{abs,j}^{t+\Delta t} + \frac{F_{16}}{Y_5} T_{fluid,j}^{t+\Delta t} + \frac{F_{17}}{Y_5} T_{amb,j}^{t+\Delta t} \quad 2.43$$

Where the coefficients F_i and Y_i are presented Appendix B Coefficients of equations.

The ambient temperature value was applied as initial condition for the air inlet and for all the SAH' component (T_g, T_{ga}, T_{abs}, T_{fluid}, and T_{ins}). Mathematically, initial and boundary conditions are $T_m (j, 1) = 298$ K, $T_{amb} (1, k) = 298$ K respectively, where, m represents the SAH element and j is the number of nodes in x direction, and k is the instantaneous time level. The stability criterion is given by Courant-Friedrichs-Lewy (CFL) condition *(Gerald, 2004)*.

$$\Delta t \leq \frac{\Delta x}{v_{fluid}} \quad 2.44$$

where Δx is grid size along SAH length depending on N, and v_{fluid} is the air velocity.

2.4.2. Iterative solution procedure

The discretized form of energy balance equations Eqs. (2.39) – (2.43) were solved using a suitable MATLAB code that was developed by considering the finned SAH system. Thermophysical properties (TPP), design parameters and geometric dimensions (GD) of the experimental SAH are gathered in Table 2.2. The procedures based on iterative method followed to determinate the output parameters such as η_{en}, η_{ex}, T_{out}, IP and SI of the finned SAH are briefly explained below:

(1) Initial values for T_g, T_{ga}, T_{abs}, T_{fluid}, and T_{ins} were assumed.

(2) The assumed values of SAH components and the physical properties (Table 2.2) were used to calculate heat transfer coefficients.

(3) The new values of T_g, T_{ga}, T_{abs}, T_{fluid}, and T_{ins} were determined using Eqs. (2.39) – (2.43) then they were compared with the initial guessed temperatures (old values). The

procedure was repeated until the difference between the new and old values of temperatures were less than 0.001, i.e. the solution procedure reached the convergence.

(4) After convergence, the required temperatures were obtained in addition to the outlet temperature, energy and exergy efficiencies, IP, and SI of SAH were determined using Eqs. (2.20) – (2.36).

The main logical steps that were followed to solve the energy balance equations using the numerical code are summarized in the highlighted section of the diagram in *Figure 2.5*.

Table 2.2 Thermo-physical properties and geometric dimensions of the experimental SAH.

Factor	Value (m)	Factor	Value	Factor	Value
L	2	τ_g	0.90	C_g (J.kg^{-1}.K^{-1})	720
W	1	α_g	0.04	C_{abs}(J.kg^{-1}.K^{-1})	897
D_1	0.05	ε_g	0.85	C_{ins} (J.kg^{-1}.K^{-1})	1000
D_2	0.025	α_{abs}	0.95	ρ_g (kg.m^{-3})	2500
δ_g	0.006	ε_{abs}	0.8	ρ_{abs}(kg.m^{-3})	2689
δ_{abs}	0.0005	k_{ins} (W.m^{-1}.K^{-1})	0.035	ρ_{ins} (kg.m^{-3})	30
δ_{ins}	0.04	k_f (W.m^{-1}.K^{-1})	390		
δ_g	0.001	ε_{ins}	0.6		

2.5. Design optimization

The considerable number of experiments needed to obtain the optimal SAH design is extremely time-consuming, besides from economic point of view, it is not efficient. Furthermore, traditional factor-by-factor parametric optimization study is implicit, and a different optimal design might be produced in the presence of the cumulative impact of all factors. Therefore, RSM approach was coupled to the numerical model to provide an explicit conclusion. In the present work, the design of experiments (DoE) technique is used to determine the optimized combination of SAH geometrical variables which attains the best possible performances for agri-food drying applications. The overall optimization process encompasses the initial design sampling through Box Behnken Design (BBD); followed by the simulation of all the design matrix using the validated analytical model; the optimization process based on RSM regression models and the desirability function *(Benhamza et al., 2018)*. The detailed optimization procedure is depicted in a flowchart in *Figure 2.5*. Moreover, similar fixed operating conditions (OC) were applied to simulate all the SAHs designs (Table 2.3**)**.

Table 2.3 Operational conditions used in the analysis.

Factor	value	Factor	value

G (W.m^{-2})	900	θ (degree)	30
T_{amb} (°C)	25	Wv (m.s^{-1})	5

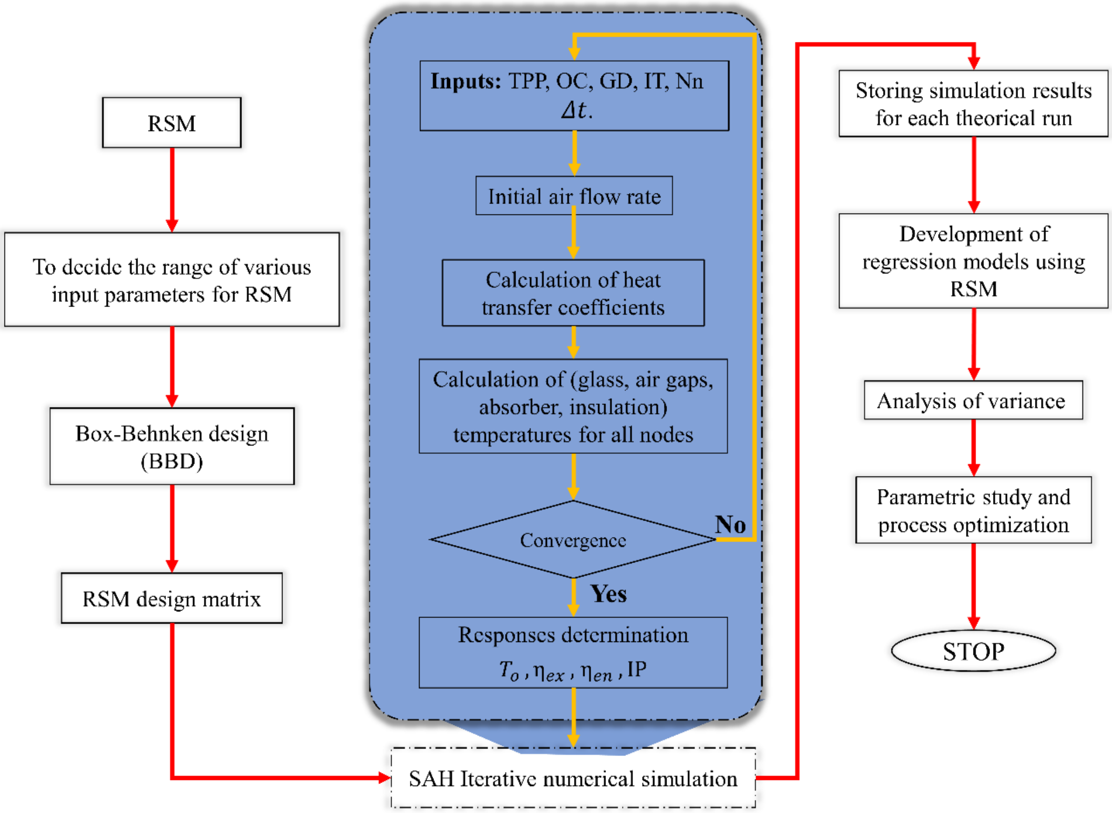

Figure 2.5 Flow chart of optimization process using RSM along with SAH numerical model.

In the first stage, the Box and Behnken Design (BBD) generated a minimum density design point grid spanning the multivariable design space. Factors of interest are aspect ratio L/W, air duct height D_2 and number of fins n_f. The ranges of variability of the three factors are given in Table 2.4. Design points were generated (17 design), five replications of center points were utilized to estimate a precise prediction of errors and testing were conducted in a randomized order. Table 2.5 shows the BBD matrix of the virtual experiments.

Secondly, in order to calculate the output parameters, the generated design points were solved by the validated analytical model using MATLAB software. In this stage, all the numerical experiments using the MATLAB code were carried out under: (1) steady state; (2) fixed solar radiation G= 900 W.m^{-2}, (3) T_{amb}=25 °C.

Subsequently, the results obtained by simulating 17 geometric configurations were injected into the RSM calculation to generate a regression model for each response (outlet temperature, energy efficiency and IP).

Table 2.4 Factors and levels of experimental design.

Factors	Level		
	-1	0	+1
L/W	1	2.5	5
D_2 (m)	0.02	0.11	0.2
n_f	0	30	60

Table 2.5 Design points generated from RSM.

Design points	A: L/W	B: D_2 (m)	C: Ns	T_{out} (°C)	η_{en} (%)	IP (W)	η_{ex} (%)
1	1	0.11	60	42.98	57.84	1716.98	1.743
2	3	0.11	30	43.90	62.18	569.49	1.965
3	5	0.11	60	48.52	66.18	936.26	2.575
4	3	0.2	0	33.10	32.55	588.87	0.453
5	1	0.2	30	36.75	56.37	1740.64	1.128
6	3	0.11	30	43.90	62.18	569.49	1.965
7	5	0.02	30	76.36	36.48	928.92	2.956
8	3	0.02	0	61.21	28.82	573.09	1.685
9	5	0.2	30	40.73	67.01	953.19	1.776
10	1	0.11	0	36.08	28.44	1763.34	0.538
11	3	0.2	60	38.91	72.27	572.87	1.702
12	3	0.02	60	73.79	43.84	551.96	3.387
13	3	0.11	30	43.90	62.18	569.49	1.965
14	3	0.11	30	43.90	62.18	569.49	1.965
15	1	0.02	30	65.25	33.46	1701.36	2.161
16	5	0.11	0	38.80	30.44	975.89	0.712
17	3	0.11	30	43.90	62.18	569.49	1.965

The RSM 2nd order regressing models are used to establish the mathematical relationship between the control factors (L/W, D2 and, n_f) and responses (T_{out}, η_{en}, IP). The general form of every response quadratic model is presented in Eq. (2.45).

$$\begin{aligned} Rs &= a_0 + a_1 A + a_2 B + a_3 C + a_{11} A^2 + a_{22} B^2 + a_{33} C^2 \\ &+ a_{12} AB + a_{13} AC + a_{23} BC \end{aligned} \qquad 2.45$$

where "Rs" demonstrates one of the studied responses (T_{out}, η_{en} or IP), and A,B,C are input factors.

Finally, a multi-objective optimization has been performed by using the desirability function (*Des(x)*). The target objective of the optimization process was to identify a set of specified factors' levels which maximizes energy efficiency and improvement potential (IP) in a specific range of temperature suitable for drying food and agriculture products. The desirability function (*Des(x)*) is presented by Eq. (2.46).

$$Des(x) = (Y_1 \times Y_2 \times Y_3 \cdots Y_n)^{1/n} \quad 2.46$$

where *n* is being the total number of dependent parameters (*Y*) *(Giri & Prasad, 2007; Myers et al., 2016)*. Also, *Des(x)* vary between 0 ≤ *Des(x)* ≤1 and represents how well the dependent parameters are matched with the specified level of independent variables *(Benhamza et al., 2018)*. Desirability of 1.0 indicates that the obtained solution can satisfy the requirement. However, it is not essential to obtain a desirability value of unity since the value entirely depends on how closely the upper and lower levels are defined relative to the actual optimum.

2.6. Statistical analysis

Analysis of variance was performed to identify the significance and fitness of RSM models as well as the impact of significant individual factors (L/W, D_2 and n_f) and their interaction on the responses (outlet temperature, energy efficiency, and IP). The probability of error value (P-value) was utilized as a tool to inspect the significance of each regression coefficient that also exhibited the interaction effect of each cross variable. A statistical software package, Design Expert (Version 11) was used to analyze the SAH data, to generate 3D graphs of responses, and to perform RSM for the numerical optimization.

3. Results and discussion

3.1. Experimental and validation results

In order to verify the accuracy and reliability of the numerical model used for the finned SAH analysis, the experimental results of active and passive modes are compared with those obtained from the analytical model. The experiments were performed during two days (20th and 21st September 2019). The passive mode has been tested in the first day, and the active mode with 150 m^3/h flow rate was tested in the second day. In the first day, the experiments were performed in passive mode (natural convection) during the period (10 am - 4 pm). The predicted and experimentally measured outlet temperature, also the weather conditions in that day are presented in *Figure 2.6*. It was observed that the ambient temperature varies between 24 °C and 32 °C. A maximum outlet temperature of 61 °C was reached at 13 pm corresponding to the maximum solar radiation (900 W/m^2). In the second day, the experiments were performed during the period of 10 am to 4 pm in the active mode with 150 m^3/h flow rate. The predicted and experimentally measured outlet temperature, also the weather conditions in that day are presented in *Figure 2.7*. It was observed that the ambient temperature varies between 15 °C and

25 °C. A maximum outlet temperature of 41 °C was reached at noon correspond the maximum solar radiation (880 W/m^2).

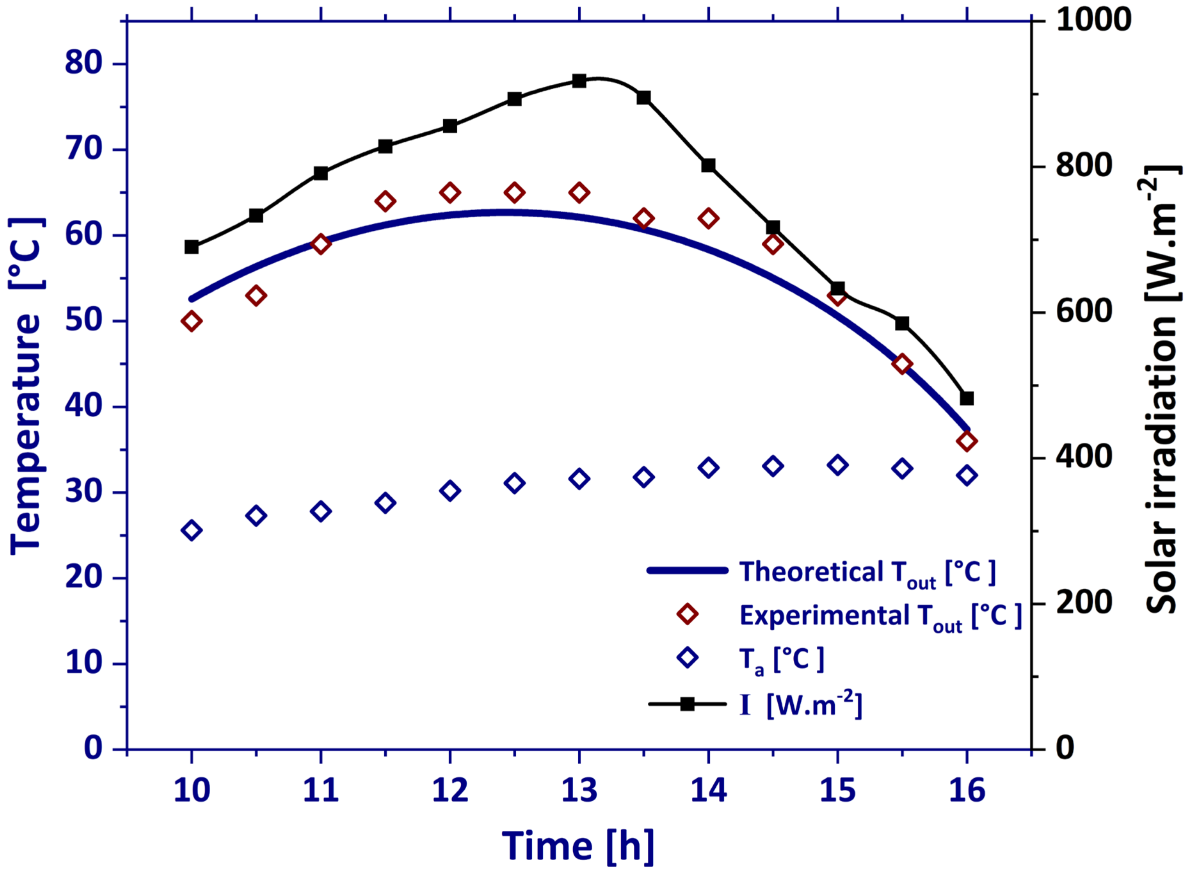

Figure 2.6 Predicted and measured Tout (10 am to 4 pm) for passive mode (the mass flow varied naturally between 43-114.76 m^3/h).

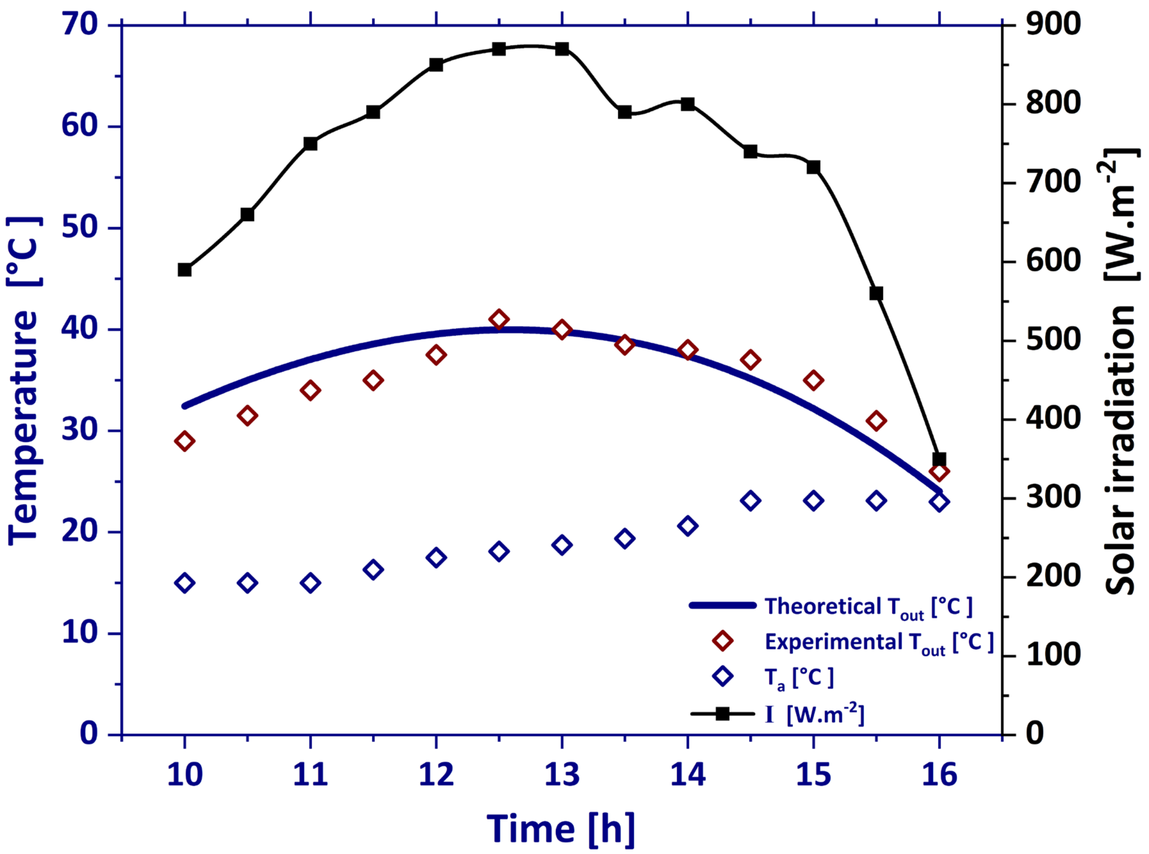

Figure 2.7 Predicted and measured T_{out} temperature (10 am to 4 pm) in active mode (150 m^3/h).

The obtained results show that the predicted and the experimental values are compatible, which highlights the ability of using the analytical model to accurately predict the SAH performances. The deviation between the numerical and experimental results ranges between 4.33% and 7.16% with an average of 5.745%, which can be compared to average errors of 3% and 9% in Refs. *(Heydari & Mesgarpour, 2018)* and *(Abhay et al., 2018)*, respectively.

3.2. Analysis of variance

The design optimization was based on Box and Behnken Design (BBD), where a quadratic mathematical model was developed for every response variable. This design is a good design for RSM because: (i) it estimates the parameters of the quadratic model; (ii) it detects the lack of fit of the model; and (iii) its ability of using blocks *(Ferreira et al., 2007)*.

The studied responses in this study were outlet temperature, thermal efficiency and IP. Analysis of variance is applied to validate the precision of these models. *Figure 2.8* compares thermal efficiency and IP with the predicted results by RSM models and exhibits that prediction errors between the predicted and actual values are very small.

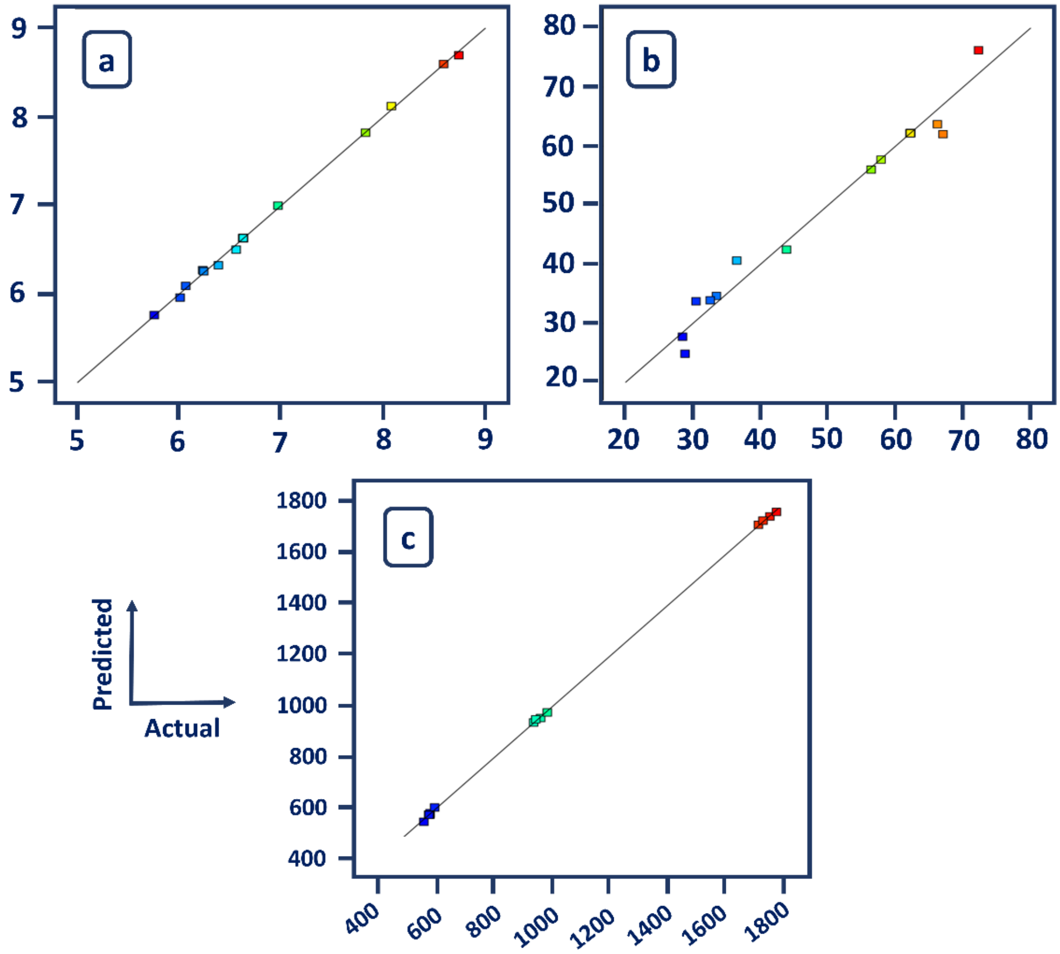

Figure 2.8 Predicted versus actual values for the RSM models (a) outlet temperature (b) thermal efficiency (c) IP with the analytical data. The 45° straight line illustrates a perfect fit.

F-value, P-value, mean squares, the degree of freedom (DoF), and sum of squares are statistical parameters to check the model accuracy. In addition, from a statistical viewpoint, determination of F-value estimates the variance of data about the mean and P-values confirm the model. F-value larger than unity indicates more precision of parameters and P-value smaller than 0.05 approves the suitability of model. The analysis of variance of the outlet temperature is reported in Table 2.6. It is seen that the F-value of model is 784.99 and the model P-values is less than 0.0001, which exhibits the accuracy and suitability of the model. For the problem under consideration, A, B, C, B^2 and C^2 are major model terms, where A, B and C represent the factors L/W, air duct height D_2 and number of fins n_f, respectively. On the other hand, the other model terms, namely AB, AC, BC and A^2 are insignificant. The agreement between the "Predicted R-Squared" (0.9874) and "Adjusted R-Squared" (0.9975) values is reasonable. "Adeq precision" which indicates the signal to noise ratio enables comparing the range of predicted values at design points with the mean prediction error. Since large values of this parameter is desirable, four being minimal *(Majdi et al., 2019)*, the attained signal to noise ratio in this study (88.899) is very satisfactory. Thus, this model can be utilized to explore the optimal conditions in the design space.

Table 2.6. Analysis of variance of outlet temperature.

Source	Sum of Squares	df	Mean Square	F-value	P-value
Model	12.90	8	1.61	784.99	< 0.0001
A-L/W	0.3253	1	0.3253	158.38	< 0.0001
B-Air duct height	9.67	1	9.67	4707.52	< 0.0001
C-Number of fins	0.8042	1	0.8042	391.56	< 0.0001
AB	0.0290	1	0.0290	14.13	0.0055
AC	0.0088	1	0.0088	4.27	0.0726
BC	0.0198	1	0.0198	9.63	0.0146
B^2	1.93	1	1.93	940.56	< 0.0001
C^2	0.1674	1	0.1674	81.52	< 0.0001
Residual	0.0164	8	0.0021		
Lack of Fit	0.0164	4	0.0041		
Cor Total	12.91	16			
Pred R-squared: 0.9874		Adj R-squared: 0.9975			Adeq Precision: 88.8989

Table 2.7 presents the analysis of variance for thermal efficiency. The F-value (42.47) exhibits the suitability of the model. The P-value of model, which is less than 0.0001, indicates that the model is meaningful. Regarding the thermal efficiency model, B and C are the significant model terms while AB and AC are insignificant model terms. The difference between the "Pred R-Squared" and "Adj R-Squared" is in an acceptable range since the difference is less than 0.2 *(Qader et al., 2019)*. The signal to noise ratio "Adeq Precision" of 22.922 exhibits an appropriate signal to noise ratio. Thus, the model can be employed for optimization of thermal efficiency.

Table 2.7. Analysis of variance of thermal efficiency.

Source	Sum of Squares	df	Mean Square	F-value	P-value
Model	3901.86	9	433.54	42.47	< 0.0001
A-L/W	71.89	1	71.89	7.04	0.0328
B-Air duct height	915.83	1	915.83	89.71	< 0.0001
C-Number of fins	1796.34	1	1796.34	175.95	< 0.0001
AB	14.53	1	14.53	1.42	0.2717
AC	10.05	1	10.05	0.9843	0.3542
BC	152.47	1	152.47	14.93	0.0062
A^2	164.42	1	164.42	16.11	0.0051
B^2	243.49	1	243.49	23.85	0.0018
C^2	438.92	1	438.92	42.99	0.0003
Residual	71.46	7	10.21		
Lack of Fit	71.46	3	23.82		
Cor Total	3973.32	16			
Pred R-squared: 0.7975		Adj R-squared: 0.9570			Adeq Precision: 22.9225

The analysis of variance for IP response is given in *Table 2.8*. It is seen from the table that the F-value of IP model is 29225.45 which means that the model is significant. In this case, A, B, C, A^2, B^2, C^2 can be considered as significant model terms. Moreover, interactions between the factors A, B and C are described by the model terms AB, AC and BC. We can conclude from *Table 2.8* that AB, AC and BC are insignificant. A very satisfactory agreement between the "Pred R-Squared" (0.9996) and "Adj RSquared" (0.9999) is attained. The "Adeq Precision" ratio of IP model (418.152) is remarkably larger than the desirable value (4), and it indicates a sufficient signal to noise ratio. Thus, the model can be used to optimize the IP also.

Table 2.8. Analyses of variance of IP.

Source	Sum of Squares	df	Mean Square	F-value	P-value
Model	876.57	9	97.40	29225.45	< 0.0001
A-L/W	233.36	1	233.36	70023.92	< 0.0001
B-Air duct height	0.3350	1	0.3350	100.54	< 0.0001
C-Number of fins	0.4870	1	0.4870	146.15	< 0.0001
AB	0.0015	1	0.0015	0.4546	0.5218
AC	0.0018	1	0.0018	0.5443	0.4846
BC	0.0032	1	0.0032	0.9667	0.3583
A^2	638.25	1	638.25	1.91E+05	< 0.0001
B^2	0.0387	1	0.0387	11.63	0.0113
C^2	0.0831	1	0.0831	24.93	0.0016
Residual	0.0233	7	0.0033		
Lack of Fit	0.0233	3	0.0078		
Cor Total	876.59	16			
Pred R-squared: 0.9996		Adj R-squared:0.9999		Adeq Precision: 418.1524	

The quadratic equations presenting the variation of the outlet temperature, thermal efficiency, and IP in terms of coded factors (A, B and C) are provided below:

$$\sqrt{T_{out}} = 6,63 + 0.2016\times A - 1.10\times B + 0.3171\times C - 0.0852\times AB + 0.0468\times AC - 0.0703\times BC + 0.6764\times B^2 - 0.1991\times C^2 \quad 2.47$$

$$\eta_c = 62.19 + 3\times A + 10.70\times B + 14.98\times C + 1.91\times AB + 1.59\times AC + 6.17\times BC - 6.25\times A^2 \quad 2.48$$

$$\sqrt{IP} = 23.86 - 5.40\times A + 0.2046\times B - 0.2467\times C - 0.0195\times AB - 0.0213\times AC + 0.0284\times BC + 12.31\times A^2 - 0.0959\times B^2 + 0.1405\times C^2 \quad 2.49$$

where A, B, and C stand for the L/W, air duct height and, number of fins, respectively.

These quadratic models obtained by RSM facilitate the studying the effects of design parameters on the responses by plotting a 3D response surface that show effect of two input parameters in a response.

3.3. Effect of length to width ratio, air duct height and number of fins on IP

The obtained results from *Figure 2.9* to *Figure 2.11* revealed that the air duct height and number of fins do not have significant effects on the IP. Contrariwise, it was founded that IP varied from 551 to 1763 with the variation of L/W from 1 to 5. Furthermore, the L/W parameter affects the IP negatively in the range (1 to 3) and positively for the designs with L/W between (3 and 5). Moreover, we can notice from *Figure 2.9* that the maximum IP value is 1763 W, where it is achieved for L/W = 1, D_2 = 0.2 m. Despite the fact that there was some inconsistency in behavior of improvement potential and by taking into account that IP is related to exergy efficiency and exergy loss as presented in Eq. (2.34), these findings compare well with Gupta et al. *(Gupta & Kaushik, 2008)* where they observed that the exergy output rate does not show monotonous trend, on the contrary to energy based results. Instead, an optimal air inlet temperature and mass flow rate exist depending on the aspect ratio and duct depth. Furthermore, the present work focused on the multi-optimization of the SAH based on three objective functions, outlet temperature, energy efficiency and IP, however to fully explain the IP behavior, a future extensive study is preferable focusing on the investigation of the effect of geometrical parameters on IP and all various exergy destructions and losses like exergy destruction between plate and sun, exergy destruction due to friction, exergy losses to the surrounding and optical exergy loss because the IP is highly related to these parameters. A recent study focusing on the abovementioned parameters has been conducted by Saravanakumar et al. *(Saravanakumar et al., 2020)*. However, only one objective function (exergy efficiency) was investigated in the optimization procedure.

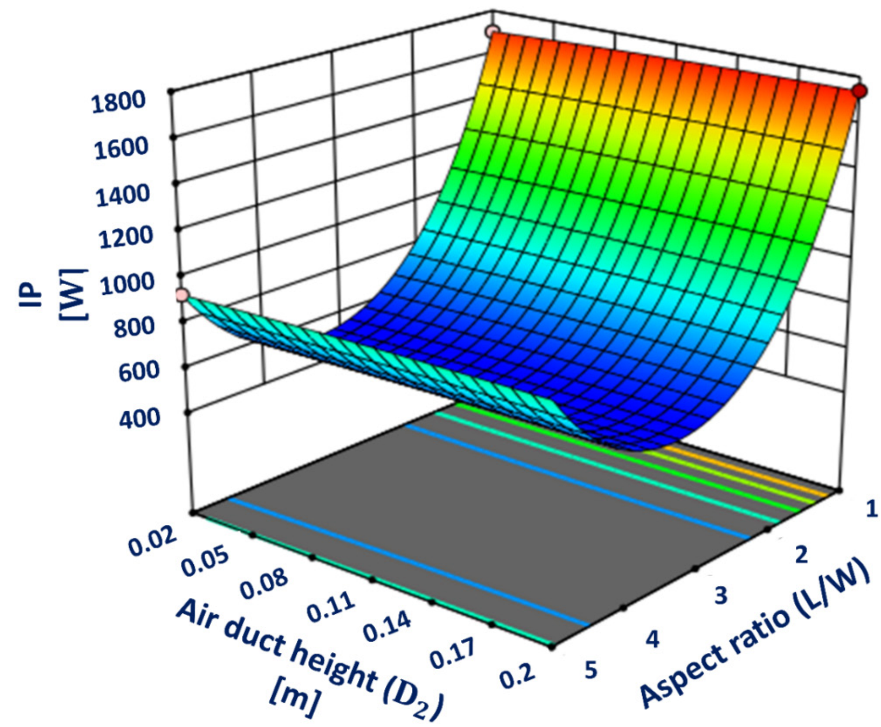

Figure 2.9 Effect of length to width ratio and air duct height on IP.

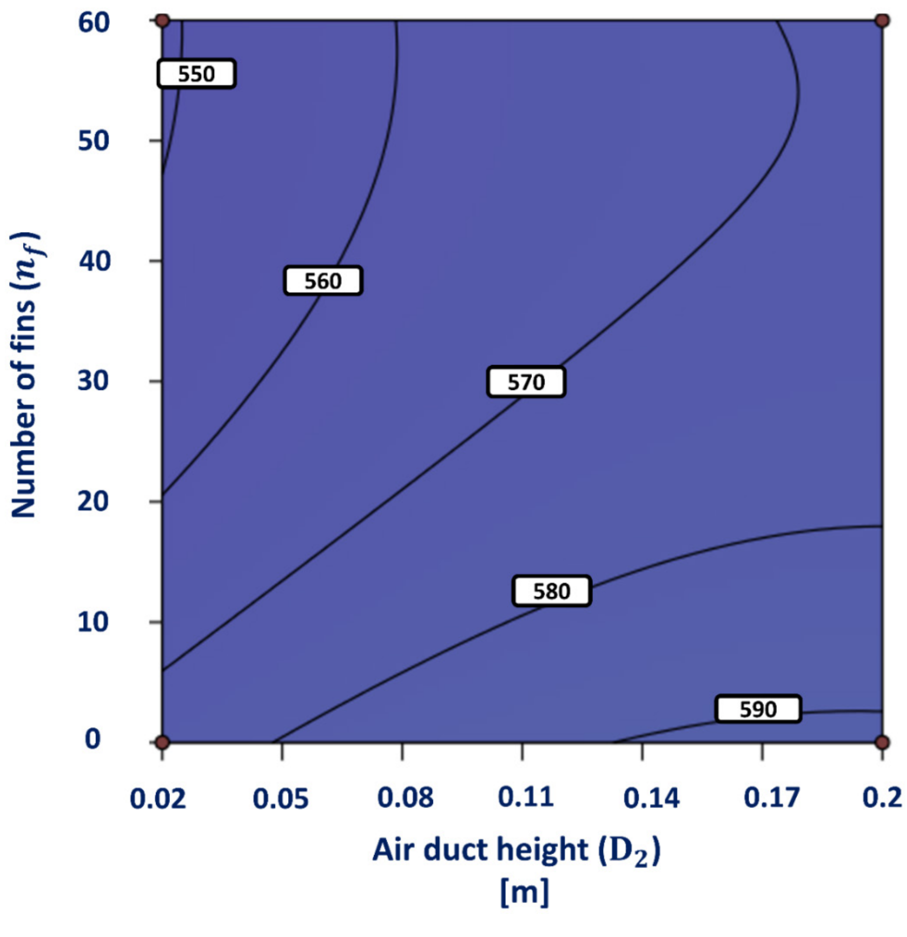

Figure 2.10 Effect of number of fins and air duct height on IP.

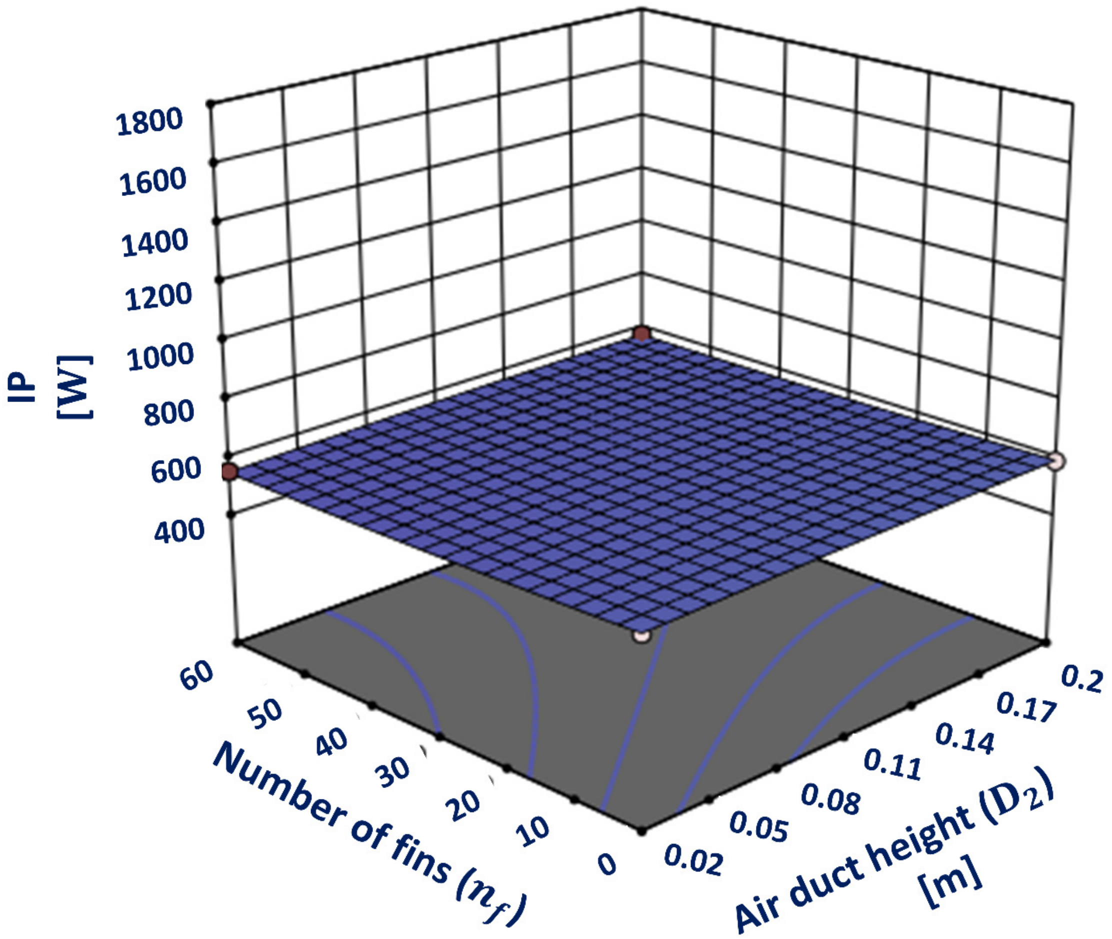

Figure 2.11 Effect of number of fins and air duct height on IP.

3.4. Effect of length to width ratio, air duct height and number of fins on outlet temperature

The outlet temperature of the finned SAHs designs is predicted for an aspect ratio (L/W) varied from 1/1 to 5/1, air duct height (D_2) from 0.02 to 0.2 m and number of fins (n_f) from 0 to 60 as shown in Table 2.4. *Figure 2.12* and *Figure 2.13* which demonstrate the influence of length to width ratio, air duct height and number of fins on the outlet temperature. The outlet temperature increases when decreasing air duct height and increasing aspect ratio (*Figure 2.12*). Hence in connection with *Figure 2.13*, increasing the number of fins results in an increase correspondingly in the outlet temperature by 8 °C and 10 °C for a collector with L/W ratio equal to 1/1 and 5/1, respectively. Increasing number of fins leads to an increase in the heat exchange surface, thus the heat transfer rate. Based on RSM model the maximum outlet temperature theoretically is approximately 76 °C for L/W=5, D_2 = 0.02 m and n_f = 30.

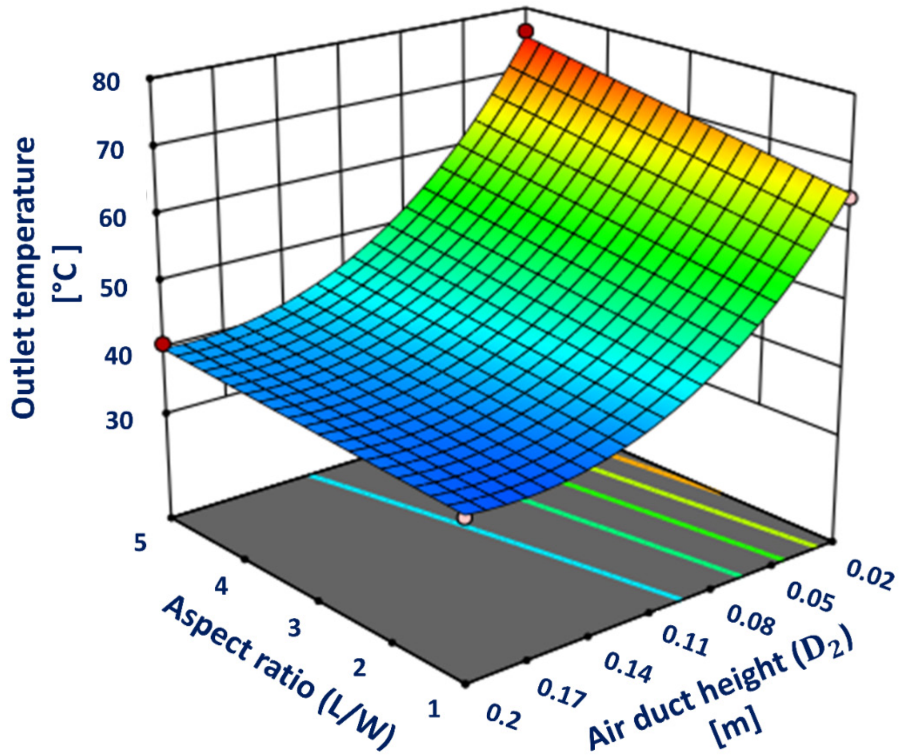

Figure 2.12 Effect of length to width ratio and air duct height on outlet temperature.

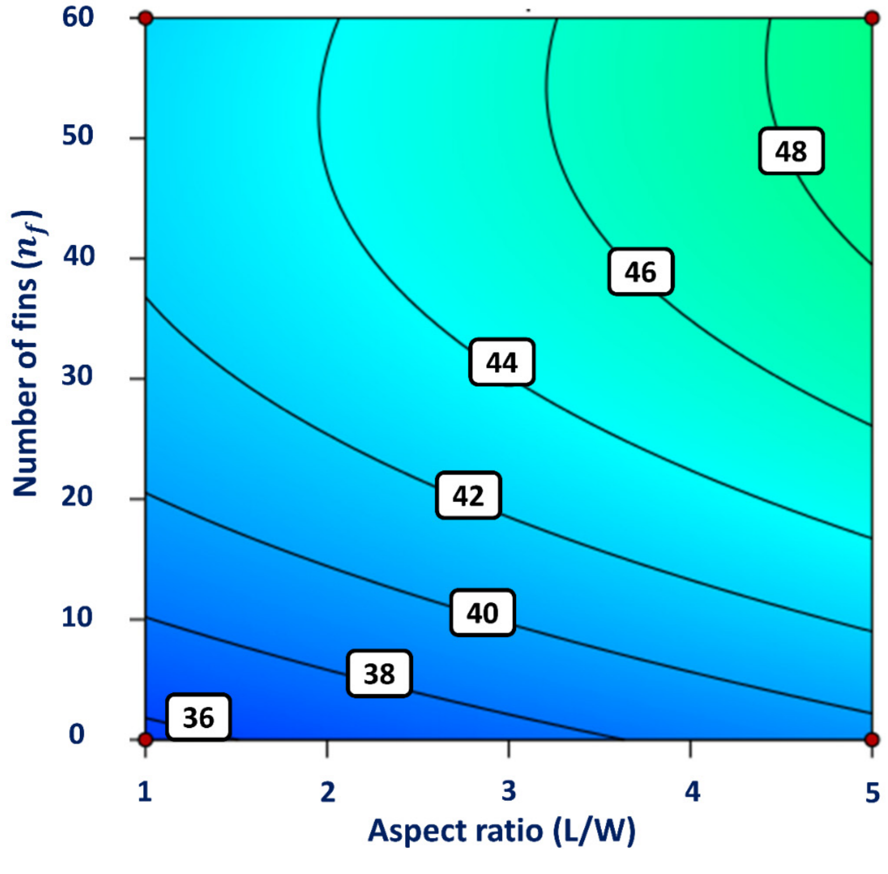

Figure 2.13 Effect of number of fins and length to width ratio on outlet temperature.

3.5. Effect of length to width ratio, air duct height and number of fins on thermal efficiency

Thermal efficiency of the finned SAHs was tested numerically by varying fins number (n_f) and air duct height (D_2) from 0 to 60 and from 0.02 m to 0.2 m respectively (Table 2.4). The previous variation effect was highlighted by plotting D_2 and n_f against thermal efficiency (*Figure 2.14*). We can observe that the n_f has a positive impact when D_2 takes its maximum value, while increasing D_2 considerably increases the thermal efficiency. In addition, a high number of fins increases heat transfer by convection due to the extended surface. Likewise, the thermal efficiency (η_e) can be enhanced by increasing the airflow rate (Eq. (2.48)). The mass flow passed by the collector depends on the airflow section that equal to W × D_2 therefore, varying D_2 has a direct impact on η_e.

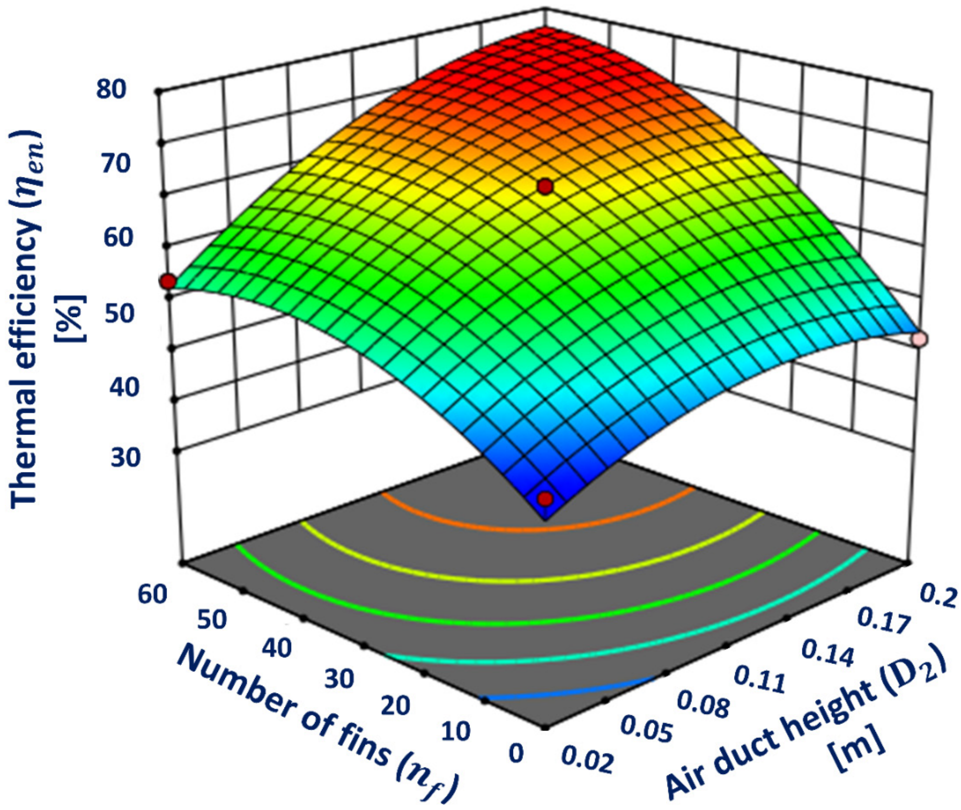

Figure 2.14 Effect of air duct height and number of fins on thermal efficiency.

The SAH thermal efficiency was predicted while varying L/W from 1/1 to 5/1 and number of fins from 0 to 60, and keeping the air duct height constant. *Figure 2.15* presents the effect of length to width ratio on thermal efficiency. It is observed that varying length to width ratio does not have a significant influence on thermal efficiency. Furthermore, the maximum thermal efficiency (72.27%) is obtained for L/W = 3, D_2 = 0.2 m and n_f = 60.

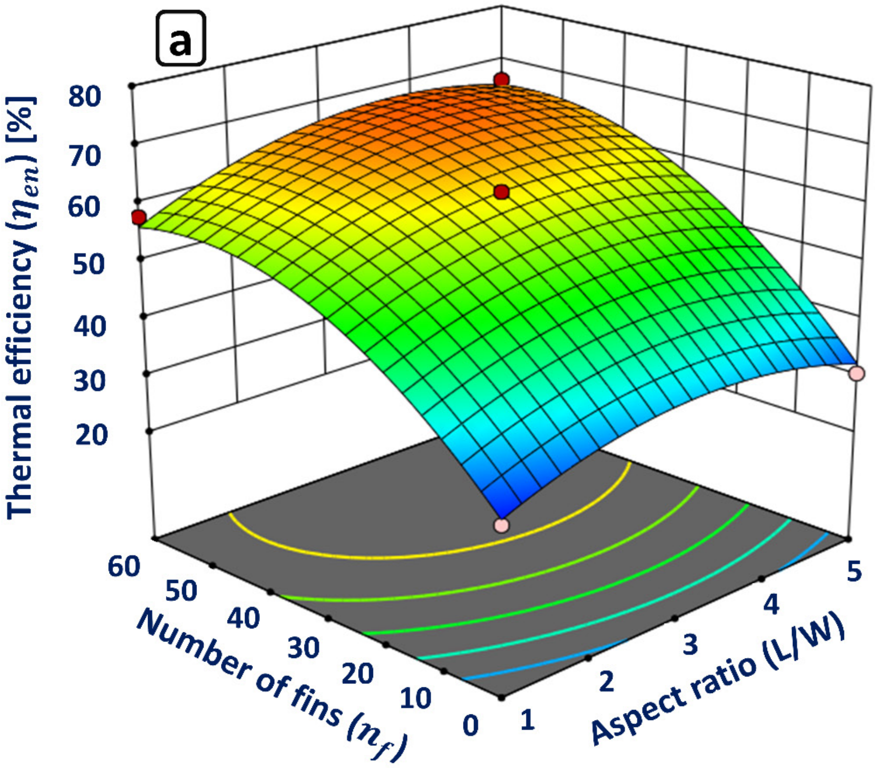

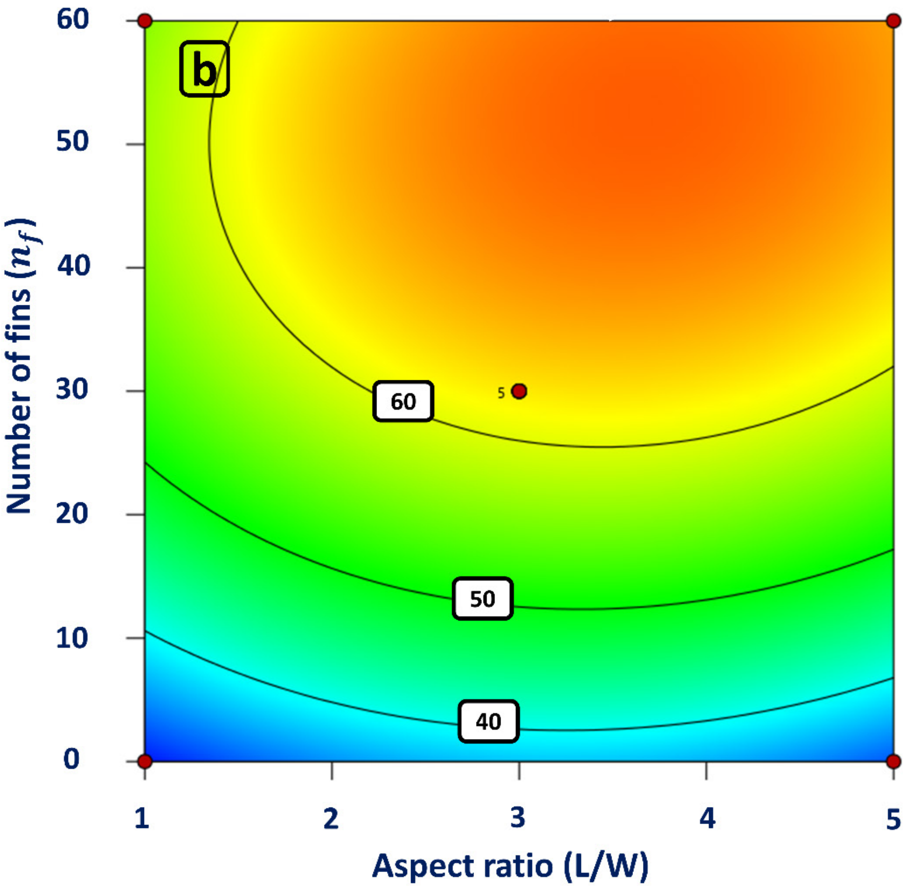

Figure 2.15 Effect of length to width ratio on thermal efficiency a) 3D response surface b) 2D contours.

3.6. SAH Optimization results

To check the desirability for output responses, L/W, air duct height, and number of fins were set to be as in range (Table 2.10), whereas thermal efficiency and IP are optimized to be at maximum level but outlet temperature is set to be in the range of 50 - 75°C according to the maximum allowable temperature for different food products (e.g. potatoes, apricot, apples, bananas, garlic, onion and carrot) as shown in Table 2.9.

The ramp function and bar graphs of desirability are shown in *Figure 2.16* and *Figure 2.17*, respectively. *Figure 2.16* presents the optimal solution of design parameters to get the desired values of outlet temperature, thermal efficiency, and IP. The ranges of the related design factors and responses are presented in Table 2.10. It is seen from *Figure 2.16* that the optimal values of input parameters are L/W=1.28, the air duct height of 0.067 m, and number of fins of 49. In order to display the desirability of the results, a bar graph is used where the variable from 0 to 1 indicates the proximity of the output to the desired output. Therefore, the bar graph reveals how each input factor is optimally set to satisfy the requirements. The values of desirability function for outlet temperature, thermal efficiency, and IP are 1, 0.0799, and 0.3725, respectively (*Figure 2.17*). Furthermore, control factors (L/W, air duct height, and number of fins) are specified to be in-range of the optimization, thus the desirability function is equal to 1. The Des values of control factors, response variables, and overall optimization combined desirability are presented in the same figure. the associated optimal values of responses and the values of the baseline design for G = 900 W/m^2 are given in

Table 2.11. The values of outlet temperature, thermal efficiency, and IP for the optimal design of the SAH with fins operating on natural convection were predicted as 52, 51.78 °C and 1397.34 W, respectively. Moreover, the thermal efficiency and IP of the optimal design obtained by RSM have been compared with the results of the baseline design (not optimized) obtained by the analytical model in *Figure 2.18*. It is seen from the figure that the optimal design improved the thermal efficiency by 15.76% and IP by 19.5%. Also, the sustainability index of the optimal design has been evaluated. And values of 1.0185 and 1.023 have been estimated for the baseline design and the optimal design, respectively.

Table 2.9 Maximum allowable temperature for different crops.

Crop	Maximum allowable Temp. (°C)	Refs.
Corn	50	*(Sharma et al., 2009)*
Apricot	65	*(Sharma et al., 2009)*
Onion, Garlic	55	*(Sharma et al., 2009)*
Bananas, dates	60	*(Boubekri et al., 2010; Mennouche et al., 2017)*
Chilies	65	*(Sharma et al., 2009)*
Apples	70	*(Sharma et al., 2009)*
Potatoes, Green	75	*(Chouicha et al., 2013)*

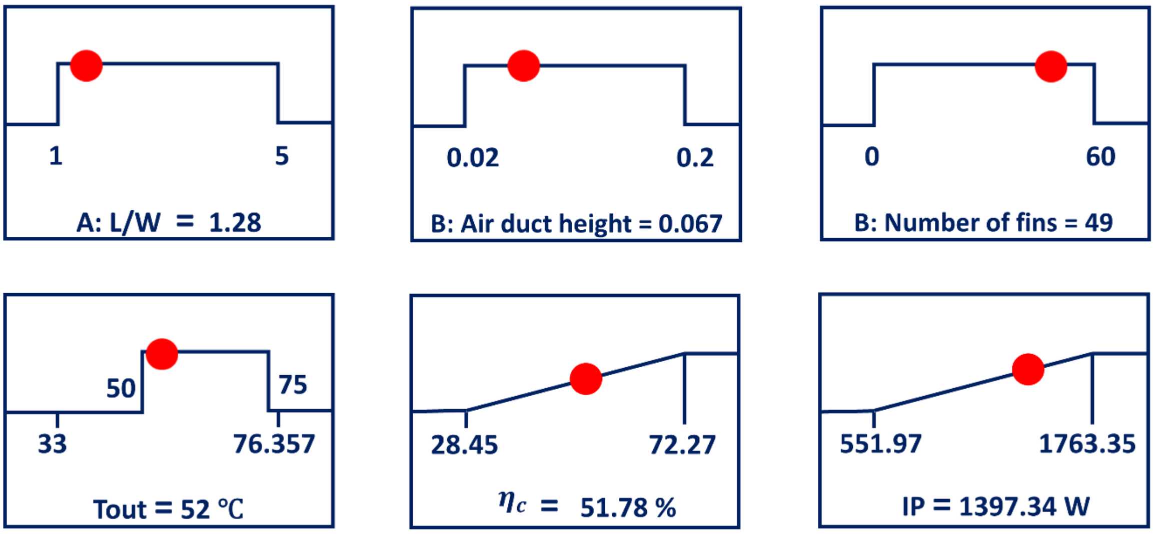

Figure 2.16 Ramp function graph of desirability of the SAH.

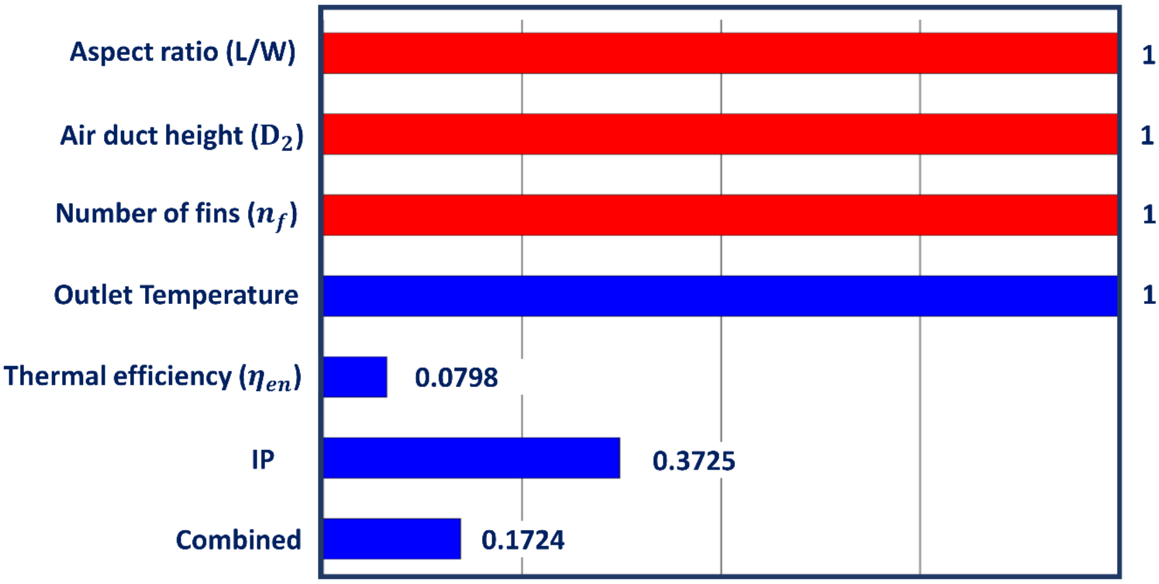

Figure 2.17 Bar graph of desirability for SAH with fins.

Table 2.10 Ranges of input parameters and responses.

Parameter	Goal	Lower limit	Upper limit
L/W	In range	1	5
Air duct height (m)	In range	0.02	0.2
Number of fins	In range	0	60
Outlet temperature (°C)	In specified range [50-76]	33.10	76.36
Thermal efficiency (%)	Maximum	28.45	72.27
IP (W)	Maximum	551.97	1763

Table 2.11 Optimal values of input parameters and responses for G=900 W/m2.

Parameter	Goal	Baseline design	Optimum values
L/W	In range	2	1.28
Air duct height (m)	In range	0.03	0.067
Number of fins	In range	24	49
Outlet temperature (°C)	In specified range [50-75]	61.16	52
Thermal efficiency (%)	Maximum	44.73	51.78
IP (W)	Maximum	1171	1397.34
Desirability	Maximum	-	0.1724

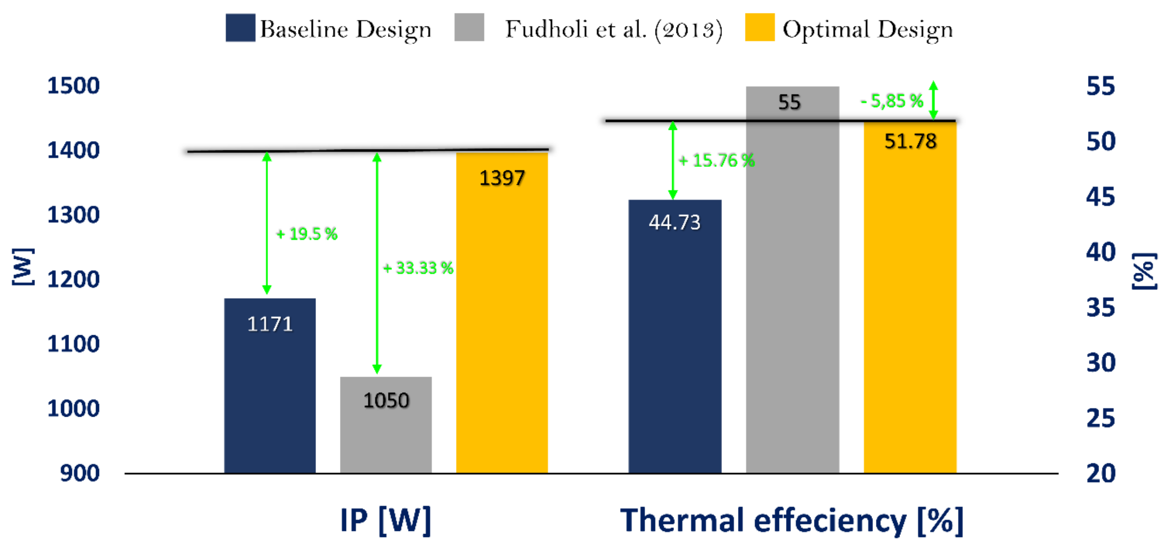

Figure 2.18 Comparison of the actual study and previous results.

3.6.1. Validation of RSM model

The optimal design parameters were considered in an additional numerical simulation, then the obtained results were compared to the RSM results (*Table 2.12*). From the validation test, it is noticed that the error between the numerical results and RSM predictions is about 0.31%, 6.30% and 7.83% for respectively the thermal efficiency, outlet temperature, and IP. Consequently, the reasonable accordance between the two results confirm the precise prediction of RSM model.

Table 2.12 Comparison of simulated responses with RSM results for the optimum design (L/W = 1.28, D_2 = 0.067 and n_f = 49).

	Outlet temperature (°C)	Thermal efficiency (%)	IP (W)
Simulation result	49	51.62	1516
RSM Result	52	51.78	1397.4
Error (%)	6.30	0.31	7.83

3.6.2. Comparison with similar studies based on thermal efficiency and IP

Finally, the optimal design SAH has been examined by comparing its performances to those reported by Fudholi et al. *(Fudholi et al., 2013)* and Karim and Hawlader *(Karim & Hawlader, 2006)*. The comparison' results with *(Fudholi et al., 2013; Karim & Hawlader, 2006)* are presented in Table 2.13. Karim and Hawlader *(Karim & Hawlader, 2006)* studied the performance of SAHs with different absorbers flat plate, finned and V-groove collector. The variation of collector efficiency with the flow rate was studied, and authors found that at 0.04 kg.s^{-1} the thermal efficiency was 52% for the simple pass SAH system. On the other hand, Fudholi et al. *(Fudholi et al., 2013)* reported that the thermal efficiency of double pass SAH system was 55% where the IP was 1050 W for the same flow rate. Compared to the obtained results in this study as shown in *Table 2.13*, the thermal efficiency is approximately similar to those shown in *(Fudholi et al., 2013)*,*(Karim & Hawlader, 2006)* for the same flow rate and superior to *(Naphon, 2005)*, *(Kabeel et al., 2018)*. Furthermore, it was found that the optimal design's IP of simple pass SAH is 33% higher than that of the double pass SAH investigated in *(Fudholi et al., 2013)*.

Table 2.13 Comparison of current study with previous work results (mass flow rate is 0.04 kg.s^{-1}).

SAH type	Thermal efficiency (%)	IP (W)	Refs.
Double pass SAH	55%	1050	*(Fudholi et al., 2013)*
Simple pass SAH	52%	-	*(Karim & Hawlader, 2006)*
Double pass SAH	40% for 45 fins 42% for 50 fins 46% for 55 fins	-	*(Naphon, 2005)*
Simple pass SAH	44% for finned (8 cm) 40% for finned (5 cm) 40% for finned (3 cm)	-	*(Kabeel et al., 2018)*
Baseline design (Present study)	44.7%	1171	-
Optimal design (Present study)	51.8%	1397	-

4. Conclusion

An effective procedure of Response Surface Methodology (RSM) together with numerical model has been used to study and evaluate the effect of geometric parameters on the performances of the solar air heater (SAH). The SAH is equipped with a fined absorber and connected to a drying chamber for the agri-food products drying applications. A numerical model based on energy balance equations has been developed and checked by a series of experimental tests. Energy and exergy efficiencies as well as improvement potential (IP) were examined as a function for aspect ratio L/W (varied from 1/1 to 5/1), air duct height D_2 (which varies from 0.02 m to 0.2 m) and number of fins n_f (in the range of 0 to 60 fins). The range of parameters are the most frequently encountered range in the bibliography. RSM with the Box and Behnken Design model was utilized to optimize the performance of SAH system with respect to the objective functions, namely outlet temperature, energy efficiency, and IP.

The main obtained results can be summed up as follows:

- A SAH numerical model based on energy balance equations has been established and experimentally validated. The delivered results are in a good agreement with the experimental test results where the mean relative error is 5.745%.
- Analysis of variance confirmed that the RSM regression models are with a high degree of accuracy, therefore they can be used to optimize the SAH design and operating conditions.
- The determined optimal conditions are: 1.28 for the ration L/W, 0.067m for the air duct height and 49 for number of fins on the absorber. This optimal design improved the energy efficiency and the IP of the SAH by 15.76% and 19.33%, respectively.
- The values of outlet temperature, thermal efficiency, and IP for the optimal design of SAH with fins under natural convection were predicted as 52 °C, 51.78% and 1397.34 W, respectively.
- The sustainability index of 1.0185 and 1.023 has been estimated for the baseline design and the optimal design, respectively.

The SAH with these geometric parameters has been designed, and currently it is being tested for drying grapes.

CHAPTER 3 DESIGN OPTIMIZATION OF INDIRECT TYPE SOLAR DRYER

1. Introduction

The improvement in thermal performance and thermal uniformity of the indirect solar dryer (ISD) depends significantly on the design parameters. Relevant design variables include geometric parameters that control the drying operation, such as height, width, tilt angle, position of the chimney and the shape of the drying chamber. To optimize and provide detailed and accurate results, almost all of the parameter probabilities must be examined which requires a considerable number of CFD simulation. Therefore, in this chapter we have used coupled methodology between DoE method and CFD simulation for multi-objective optimization purpose. For the implementation of this technique, we will use the CFD software ANSYS®18.1 FLUENT combined with JMP 14 software. The experimental validation of the numerical model with a suitable grid and turbulence model is investigated. In the current chapter, commercial CFD software ANSYS FLUENT has been used to establish a validated numerical model of an ISD. The Navier-Stokes equations have been solved for this specific problem based on experimental boundary conditions where the experimental and numerical results are compared.

2. Material and methods

2.1. Experimental procedure

Several experiments were carried out, on a typical clear sky day, in order to study the physical behavior of an ISD working on passive mode. The dryer was previously designed and constructed at the laboratory of new and renewable energies in Arid zones (L.E.N.R.E.Z.A) at the University of Ouargla, Algeria (31.9° N, 5.3° E). Ouargla city has an important annual solar radiation that means between 2080 kWh/m^2/year and 2160 kWh/m^2/year *(Settou et al., 2021)*. The ISD has been used for agri-food products drying experiments. It consists of a double pass solar air heater (SAH) to generate heated air, drying chamber and a chimney placed at the top of drying chamber to ensure air motion by natural convection (*Figure 3.1*).

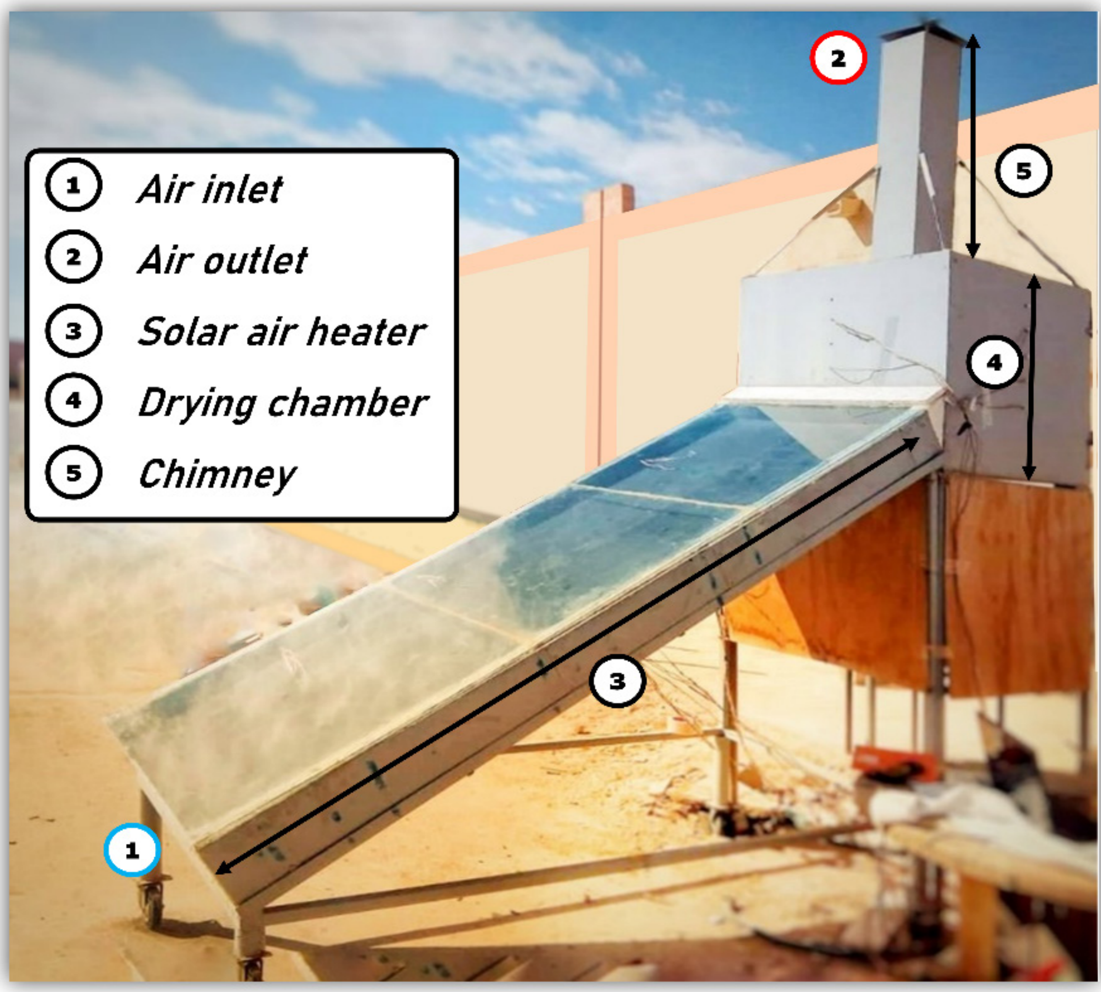

Figure 3.1 Experimental setup of the solar dryer.

The SAH comprises two parallel channels separated by a metallic absorber painted with black. This type of SAHs is more effective compared to a single pass due to allowing more heat transfer rate *(Lingayat et al., 2020)*. The upper channel is covered with a glass layer whereas the bottom channel and sides are thermally insulated. The outlet of the SAH is connected directly to the cubic drying chamber from the front side to save thermal energy wasted in case the SAH connected using an intermediate channel. The coming air from the SAH enters the drying chamber with a high enthalpy and triggers the water evaporation inside the product after absorbing the thermal energy carried by air. Thereby, the reduction of water activity in the product increases the stability and reinforces the perishing resistance of products.

Two PT100 (ref. TM110, KIMO) thermocouples with ±0.5°C of accuracy were used for temperature measurement at the outlet of the SAH and at the center of drying chamber. In order to measure the solar radiation, a pyranometer (SLM018 c-E) with a sensitivity of <3% ± 1 digit from 100 to 1000 W/m^2 was connected to the test setup and inclined at the same angle of SAH.

An anemometer (Testo 416) with ± 0.2 m/s + 1.5% of mv of uncertainty was used to measure drying air and wind velocity. All the specifications of the solar dryer are described in Table 3.1 and

Table 3.2. A clear sky typical day was chosen to carry out the experiments. The solar dryer was exposed to solar irradiation during the day, whereas the chosen period for the comparison was from the sunrise until the maximum radiation hour (8:00 – 13:00).

The experimental tests were performed in a typical clear sky day (April 21th 2019) and the solar dryer was tested under natural convection (passive mode) with no-load condition. An automate type cDAQ-9174 connected to PC with a data acquisition platform was used for recording all the instruments data every 30 min from 8:00 to 13:00. A schematic diagram of the experimental setup with the measurement instruments is presented in *Figure 3.2*.

Table 3.1 Specifications of the basic components of the solar dryer.

Component	Specifications
SAH type	Double pass
Dimensions of SAH	2 m × 1 m
SAH tilt angle	31° (With horizontal)
Drying chamber	The ISD was tested under no load
Dimensions of the drying chamber	1 m × 1 m ×1 m

Table 3.2 Thermophysical properties.

Properties	Air	Glass	Stainless steel
Density, (kg/m^3)	1.18	2500	7850
Thermal conductivity (W.m^{-1}.K^{-1})	0.0242	0.81	15
Specific heat (J/kgK)	1006.43	840	460
Viscosity (N.s/m^2)	1.7894E-5	-	-

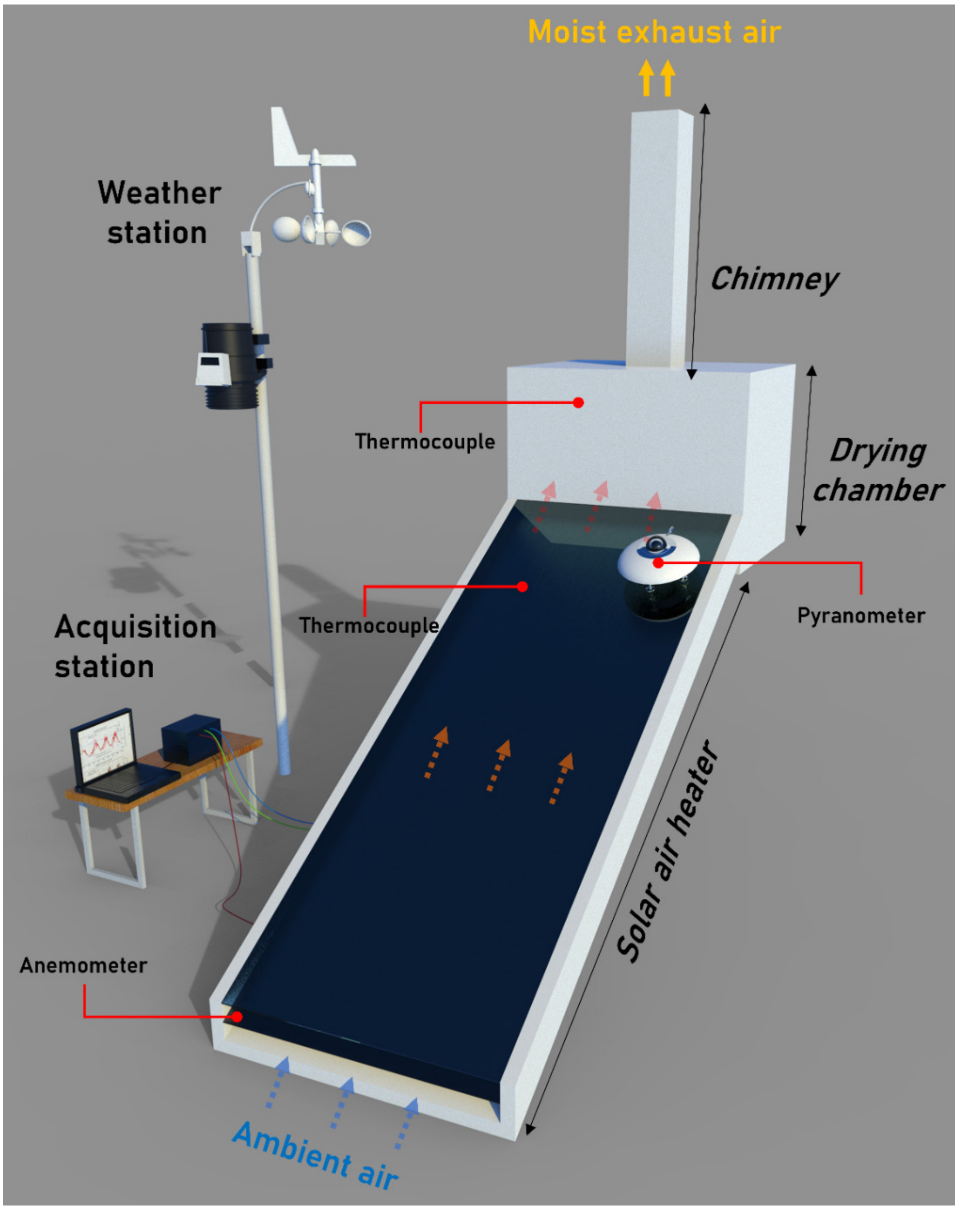

Figure 3.2 Schematic diagram of the experimental setup.

2.1.1. Experimental uncertainties

Errors and uncertainties occur in tests due to the collection of instruments, calibration, observations, environmental factors, preparation of tests and measurements. During the experimental tests, operating temperatures, wind speed, and solar radiation were calculated using suitable instruments. The result R is a function offered in the form of independent variables. Let W be the uncertainty where the subscripts R and 1, 2, … n denote the uncertainty in the outcome and in the independent variables, respectively. This function can only be used if the uncertainty in independent variables is given with the same oddity:

$$W_R = \left[\left(\frac{\partial R}{\partial x_1} W_1 \right)^2 + \left(\frac{\partial R}{\partial x_2} W_2 \right)^2 + ... \left(\frac{\partial R}{\partial x} W_n \right)^2 \right]^{1/2} \quad 3.1$$

During the experiments, the measured parameters' uncertainties are presented in Table 3.3. It is observed that all uncertainties were in an acceptable range.

Table 3.3 Associated uncertainty for the measurement sensors.

Parameter	Unit	Uncertainty
Solar radiation	$W.m^{-2}$	± 1.22
Inlet air temperature	°C	± 0.62
Outlet air Temperature	°C	± 0.62
Ambient temperature	°C	± 0.59
Air velocity	m/s	± 0.30
Wind Speed	m/s	± 0.30

2.2. Numerical procedure

The simulation techniques used in this numerical study are explained in the upcoming sections, where details of the practical domain, meshing, equations and boundary conditions are presented separately. The numerical solution procedure is summarized in *Figure 3.3*.

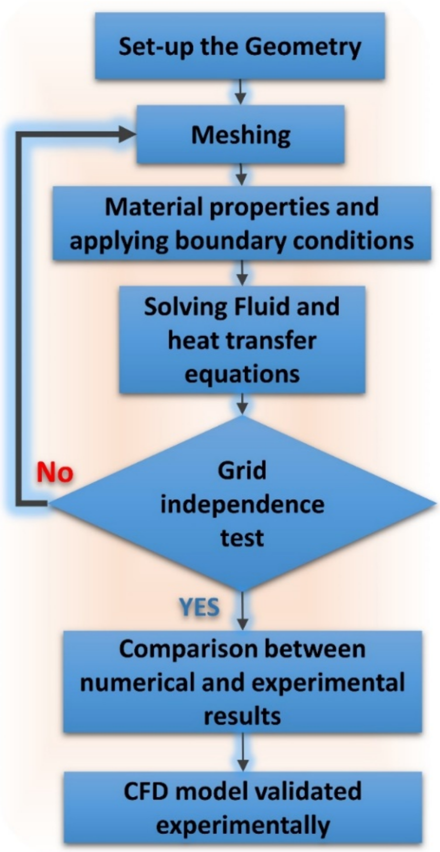

Figure 3.3 numerical simulation procedure.

2.2.1. Solution domain

An ISD is considered for this numerical analysis. This type of solar dryers contains drying chamber, SAH, and the chimney. 3D volumes of these physical parts have been simplified into 2D solution domains. Sandali et al. *(Messaoud Sandali et al., 2019)* suggested the use of 2D flow model to improve a direct type solar dryer using geothermal source, besides a 2D model has been used to increase SAH operating time using phase change materials *(Sandali et al., 2017)*. A 2D numerical model has been test using phase change materials in solar air heater system *(Benhamza & Settou, 2016)*. Also a direct type solar dryer with integrated porous medium is simulated by *(Sandali et al., 2018)*. The same drying system has been tested experimentally by *(T. Hadibi et al., 2021)*. Similarly, an ISD was developed numerically based on a 2D domain by Khaldi et al. *(Khaldi et al., 2017a; Khaldi et al., 2017b)*. The model has been used for studying the behavior of the drying system, where the effect of a reversed absorber on the airflow uniformity was investigated. In another study, transient heat transfer in solar dryers has been modeled by *(Tegenaw et al., 2019)*. The numerical modeling was based on a 2D axisymmetric simplified domain with excluding the relatively thin components of the drying cabinet from the flow domain. In all these scientific contributions cited before, the authors compared the numerical results with those obtained by physical experiments and a good agreement was observed. Therefore, the complexity of 3D models can be avoided in our investigation study by using a 2D CFD flow model to study the dynamic and thermal behavior of the solar dryer.

2.2.2. Governing equations

In this study, the CFD analysis was performed using ANSYS FLUENT 18.1 software. The finite volume method was utilized for the discretization of the mass, momentum and energy equations. The solving process was based on the following assumptions: (i) the fluid flow is supposed to be 2D incompressible in steady state; (ii) the turbulent flow is fully developed and monophasic; (iii) the thermophysical properties of the solid materials are constants; (iv) the effect of moisture product on the temperature distribution is negligible; (v) the viscous dissipation flow of the heat is insignificant; (vi) the Boussinesq approximation is utilized to account the air density change with the temperature and given by:

$$\rho = \rho_0 \left[1 - \beta \left(T - T_0 \right) \right] \qquad 3.2$$

where ρ_0 , T_0 and β denote, respectively, the reference density, reference temperature, and thermal expansion coefficient of the fluid.

Fluid flow and heat transfer phenomena in the ISD are governed by the continuity, momentum and energy equations, which are presented below in the Cartesian tensor system:

The continuity equation:

$$\nabla\left(\rho\vec{v}\right)=0 \tag{3.3}$$

The momentum equation:

$$\rho\vec{v}+\nabla\vec{v}=-\nabla\vec{P}+\nabla\ddot{\tau}+\rho\vec{g} \tag{3.4}$$

Energy equation:

$$\rho c_p\vec{v}+\nabla T=k\nabla^2 T+\vec{\nabla}.\ddot{\tau}\vec{v} \tag{3.5}$$

Where ρ is density, $\vec{v}$ vector of velocity, $\nabla=\frac{\partial}{\partial x}+\frac{\partial}{\partial y}$, p is the static pressure, $\ddot{\tau}$ is the Reynolds stress tensor, c_p is the specific heat, and k is thermal conductivity.

To model the turbulence flow the *k-ε* model, RSM and RNG have been used for different experimental applications *(Potgieter et al., 2020)*. In the current investigation, the RNG k-ε turbulence model is used to characterize the turbulence in the computational model as suggested by *(Abhay et al., 2018; Alimohammadi et al., 2020; Güler et al., 2020; Khanlari et al., 2020)*.

Turbulence kinetic energy (*k*) and dissipation rate of turbulent kinetic (*ε*) equations are given by Eqs. (3.63.6) and (3.7), respectively.

$$\nabla.\rho\kappa\vec{v}=\nabla.\left(\mu+\frac{\mu_t}{\sigma_\kappa}\right)\nabla\kappa+G+B-\rho\varepsilon_\kappa \tag{3.6}$$

$$\nabla.\rho\varepsilon\vec{v}=\nabla.\left(\mu+\frac{\mu_t}{\sigma_\varepsilon}\right)\nabla\varepsilon+C_{1\varepsilon}\frac{\varepsilon}{\kappa}G+C_{1\varepsilon}(1-C_{3\varepsilon})B-\left(C_{2\varepsilon}\rho+\frac{C_\mu\eta^3\left(1-\eta/\eta_0\right)}{1+\beta\eta^3}\right)\frac{\varepsilon^2}{\kappa} \tag{3.7}$$

Here, empirical values of $C_{n\varepsilon}$ constants in Eq.(3.7) are $C_{1\varepsilon} = 1.42$, $C_{2\varepsilon} = 1.68$, $C_{3\varepsilon} = 0.0845$.

SIMPLE algorithm was applied to couple pressure and velocity. The gradient was computed using Least Squares Cell-Based method, second order scheme is used for the discretization of pressure equation. Momentum equations, energy, turbulence kinetic energy, and turbulent dissipation rate equations were discretized by the second order upwind scheme. The convergence criteria was 10^{-4} for the continuity, momentum, k, and ε equations whereas it was 10^{-6} for the energy convergence.

2.2.3. Boundary conditions

The quasi-steady state computational domain has been modeled to obtain temperature and velocity distributions within the 2D domain. A representative schematic of the boundary conditions is shown in *Figure 3.4*. For both inlets of SAH, a pressure inlet with zero-gauge pressure condition was prescribed. The air enters with 307.7 K since this value represents the ambient temperature obtained from the experiments. The pressure outlet condition is set at the exit of computational domain. Regarding turbulence at the inlet, a turbulence intensity and a turbulent viscosity ratio equal to 5% and 10, respectively, were used. No-slip condition was considered over the solid walls that surround the fluid. Since the experimental solar dryer is thermally well-insulated by polystyrene, the heat loss from the solar dryer edges was neglected and therefore, adiabatic wall condition was adopted to all the boundary walls.

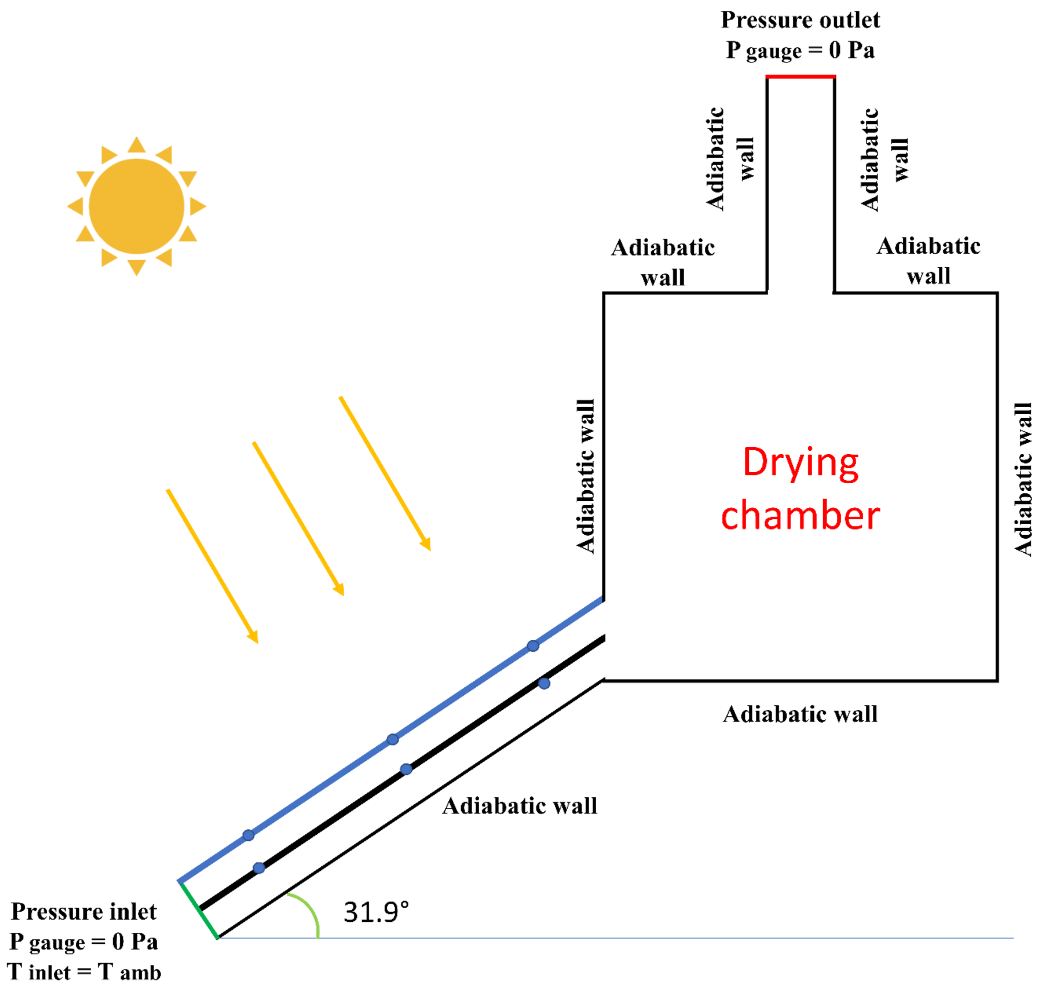

Figure 3.4 Boundary conditions.

2.2.4. Mesh generation

In order to obtain an accurate CFD model, a proper mesh for the system should be selected and before solving the problem, all the ISD parts were considered for the meshing process *(Iranmanesh et al., 2020)*. In the first stage of mesh checking, the statistical criteria (skewness) with additional checking variable (aspect ratio) have been used in this paper to check the quality of grid. Generally, the skewness values are ranged between zero and one, the best mesh and worst mesh are for skewness equal to 1 and 0, respectively *(Brandl et al., 2015; Karmare & Tikekar, 2009)*. Moreover, the optimum value for aspect ratio might be regarded to be less than 5 *(Ranjbaran et al., 2014)*. The mesh with fine elements was considered for the solar dryer volume where the average skewness obtained from evaluation reports of the meshing process was 0.13 which is suitable for the analysis of any modification of the solar dryer.

The second stage was based on verifying the grid independence in order to obtain an accurate CFD model. A non-uniform mesh of the studied domain has been generated. The solution domain has been discretized on several elements' sizes. The grid independence test is carried out for different numbers of nodes, namely 58454, 103699, 145744, 286892, 360193, 409944, and 911580. And the solar dryer outlet velocity has been calculated for every grid. Variations of V_{out} with number of nodes are shown in *Figure 3.5*. A very small difference is observed in outlet velocities (V_{out}) obtained by 409944 and 911580 nodes. As the percentage changes, the values of V_{out} are minimum (1.23%) for 409944 and 911580. Thus, for all the remaining cases the mesh with 409944 nodes is used in the numerical simulations. Other mesh parameters are indicated in Table 3.4.

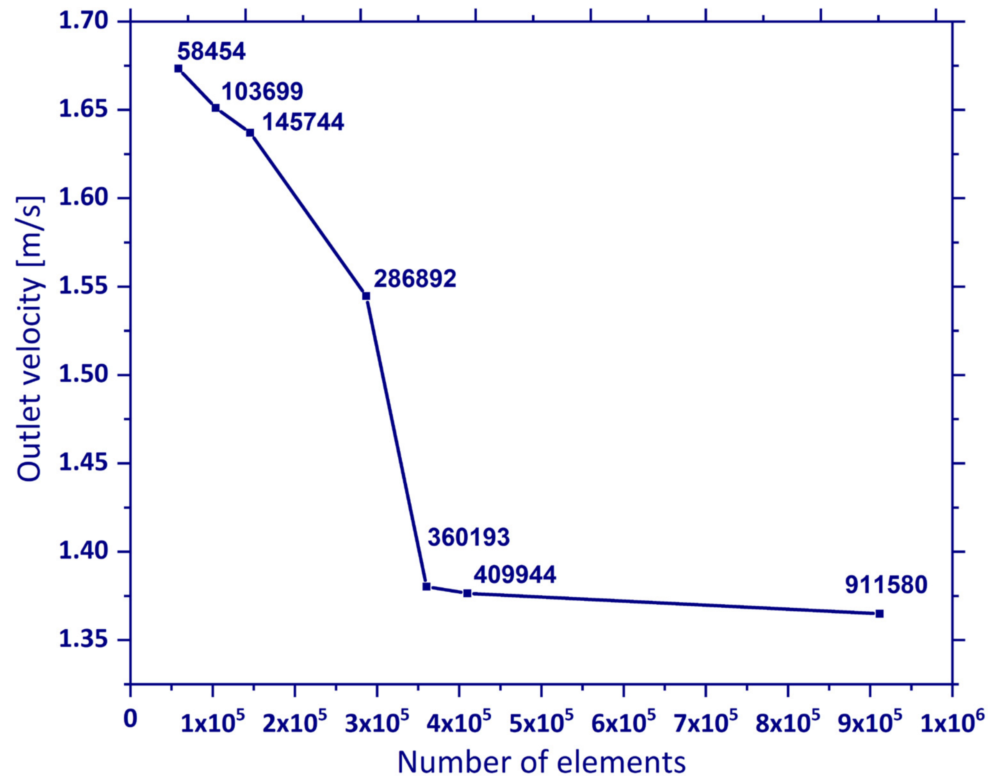

Figure 3.5 Outlet Air velocity versus the number of grid nodes.

Table 3.4 Mesh parameters and properties.

Parameter	Value/quality
Element size	0.0015 m
Mesh metric	Skewness and aspect ratio
Number of elements	409944
zones	Chimney, drying chamber, SAH
Skewness	0.13
Standard deviation (Skewness)	0.17
Aspect ratio	1.08
Standard deviation (Aspect ratio)	0.1
Element quality	0.87
Standard deviation (Element quality)	0.16

2.3. Optimization Procedure

Initially, the choice of these variables (length, width, position, angle of inclination of the chimney and the shape of the chamber) is due to their direct effect on the uniformity of the thermal and dynamic fields. The standard deviation of temperature, outlet speed, and average temperature in the drying chamber were defined as output parameters (Responses) on the JMP 14.

The program JMP 14 is an optimization module which derives the optimal design variables according to the constraints of design and of the objective function. In this method, several criteria (such as "maximize", "minimize" or "determine target value") are used to find a geometric design that achieves optimal thermal and dynamic fields across multiple output parameters.

The overall optimization process encompasses the initial sampling to proceed to the design of experiments (DoE) method, followed by the appropriate interpolation technique using a response surface method (RSM) *(Benhamza et al., 2021; Benhamza et al., 2018; Mecheri et al., 2019)*.

Finally, the data from the previous two steps are analyzed to achieve the design of the optimal ISD. The detailed optimization procedures are described in the form of a flowchart on the *Figure 3.6*.

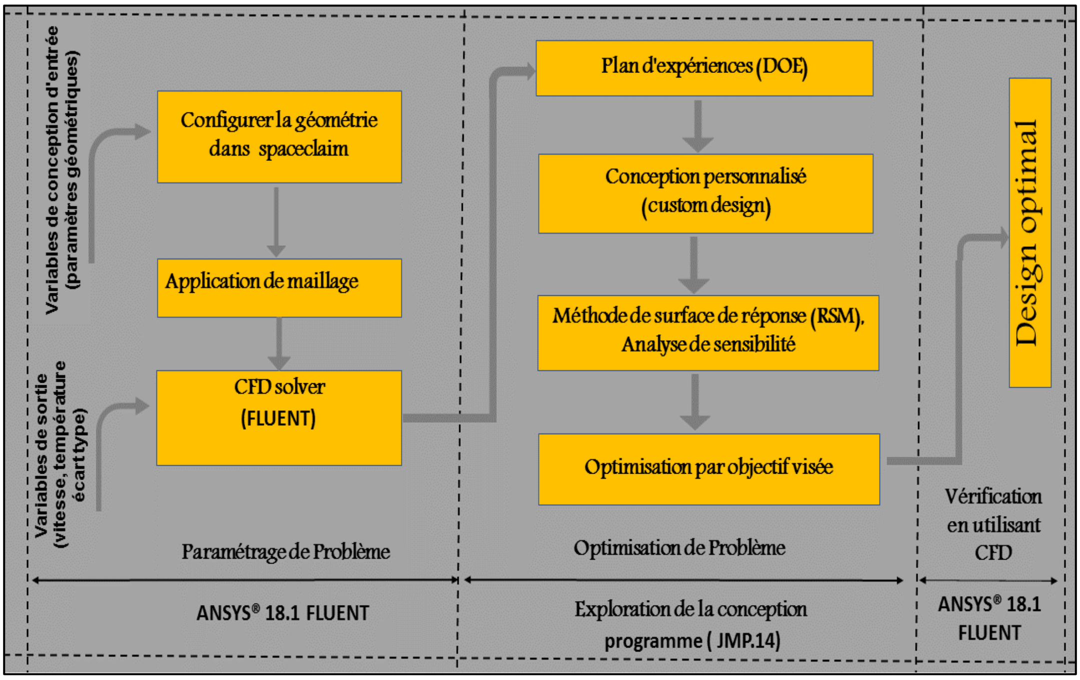

Figure 3.6 Optimization procedure chart

- Responses selecting (standard deviation, Average T, and Outlet velocity).
- Selecting factors of interest (Geometrical parameters: A.Chimney length, B.Chimney width, C.Chimney angle, D.chimney position, E. Drying chamber shape).
- Levels of Factors.
- Selection of the suitable design of experiments.
- Optimization using RSM.
- Obtaining responses for every virtual design using ANSYS FLUENT.
- To analyze the results using response surfaces in order to find the optimal design.

2.3.1. RSM methodology

The design selected in this chapter is Custom design which allow to combine between the advantages of the RSM and screening designs, where in RSM designs only continuous type of factors is acceptable

Custom Designs

Use the Custom Design platform to construct optimal designs that are custom built for your specific experimental setting. Generally, a custom design is more cost-effective than a design obtained using alternative methods. You can perform the following tasks:

- Enter factors of many different types.
- Specify constraints on the design space.
- Indicate which effects are necessary to estimate and which are desirable to estimate, if possible, given the number of runs.
- Specify a number of experimental runs that matches your budget.

The Custom Design platform constructs a wide variety of designs, including these special design types: Screening, Response Surface, Mixture, Random Block, Split Plot, Split-Split-Plot, and Two-Way Split Plot.

Use the Custom Design platform as your primary tool for constructing a wide range of experimental designs. You can construct a variety of design types and fine tune them to your specific experimental needs and resource budget.

Custom Design provides more options and control than the Screening, Response Surface, Full Factorial, and Mixture Design platforms. The designs that you construct are created specifically to meet your goals. This eliminates the struggle to find a classical design that only comes close to meeting your goals.

The flexible special-purpose designs that you can construct using Custom Design include:

- Screening designs, including supersaturated screening designs
- Response surface designs, including those with categorical factors
- Mixture designs, including those with process factors, and mixture of mixture designs
- Designs that include covariates or that are robust to linear time trends
- Fixed and random block designs
- Split-plot, split-split-plot, and two-way split-plot (strip-plot) designs

The advantage of this method lies in the fact that the number of experiments to be carried out is limited and must be as small as possible, however these experiments must be structured and organized. A mathematical modeling can correspond to the experimental model which is expressed. This makes it possible to relate the variation of the factors studied to the variation of the measured response Y = f (X1; X2;... Xk). Thus this mathematical model allows a deeper interpretation of the phenomena. It has predictive qualities and makes research directions more reliable.

The theory of this method and of the different experimental designs is dealt with in detail in several books in French and English; Jacques Goupy's book entitled "Introduction to experimental designs" is a highly recommended book which explains the method with several application examples. Today's software makes it easy to build all plans and perform the most complex calculations quickly and without any difficulty. The widely recognized software that deals with the method are: JMP, STATGRAPHICS, DESIGN EXPERT and MINITAB.

In this study, the RSM algorithm was applied to derive the optimal design based on the sets of targets represented in the average drying chamber temperature, temperature standard deviation, and outlet velocity.

a. Drying chamber average temperature

For proper drying of food products we seek a drying temperature within the range of 50 to 75. ***(Sumit Tiwaria, (2018)).*** More details of the suitable temperature for drying agrifood.

b. Standard deviation

In statistics, Standard deviation is a measure of the dispersion of values in a statistical sample or probability distribution. It is defined as the square root of the variance or, equivalently, as the root mean square of the deviations from the mean. It is usually written with the Greek letter σ ("sigma"):

$$\sigma = \sqrt{\frac{1}{n}\sum_{n=1}^{n}(x_i - \bar{x})^2} \qquad 3.8$$

Standard deviations are generally used to synthesize the numerical results of a repeated experiment. In both probability and statistics, it is used to express other important concepts such as the correlation coefficient, the coefficient of variation or the optimal Neyman distribution.

In our part of the study this statistical parameter is used as a response to investigate the temperature uniformity in the drying chamber. After the CFD simulation of each design of the virtual designs obtained from the DoE. Using the post-CFD software we all the temperatures have been exported from the existing nodes to the drying chamber, then along with the temperature standard deviation is calculated with EXCEL. The temperature standard deviation in this case is the average of the sums of the distances between the temperatures of the nodes and the average temperature. After this definition it is clear that the minimum standard deviation represents the uniform distribution of temperature.

c. Outlet velocity

The improvement of the dynamic fields has a great influence on the drying operation that is why we have chosen the output speed as a response to be optimized in this study.

2.3.2. Factors and levels

The study consisted of developing a design of experiments aimed at optimizing the responses presented above. Several parameters were studied to determine their influence on the responses. These parameters are the height, the air gap, the tilt angle of the chimney, as well as the shape of the drying chamber and the position of the chimney. For each of the continuous factors and categorical factors, the variation levels (low and high) -1 and +1 have been defined and are presented in the Table 3.5.

Table 3.5 Factors and levels of experimental design

Factors	Variables	Level -1	Level +1
Continuous			
01	Chimney length [cm]	30	120
02	Chimney width [cm]	5	15
03	Chimney angle [°]	30	90
Discrete			
04	Chamber shape	Cubic chamber	shape 2
05	Chimney position	Left Center	Right

2.3.3. Experimental Design matrix

Table 3.6 Design points generated from RSM

Run	Factor 1 A:Chimney length	Factor 2 B:Chimney width	Factor 3 C:Chimney angle	Factor 4 D:Chamber shape	Factor 5 E:Chimney position
1	75	15	90	shape 2	Right
2	30	15	60	shape 2	Left
3	30	10	30	Cubic chamber	Left
4	30	15	30	shape 2	Center
5	30	5	90	shape 2	Center
6	120	15	90	Cubic chamber	Right
7	75	15	60	Cubic chamber	Left
8	120	5	60	Cubic chamber	Left
9	120	5	30	shape 2	Center
10	75	10	60	shape 2	Center
11	30	5	60	Cubic chamber	Center
12	75	5	30	Cubic chamber	Right
13	120	15	90	shape 2	Center
14	120	10	90	shape 2	Left
15	120	5	90	shape 2	Right
16	30	10	60	Cubic chamber	Right
17	120	15	30	shape 2	Left
18	30	15	90	Cubic chamber	Center
19	30	15	30	Cubic chamber	Right
20	75	10	90	Cubic chamber	Center
21	30	5	90	Cubic chamber	Left
22	30	5	30	shape 2	Right
23	75	5	60	shape 2	Left
24	120	15	30	Cubic chamber	Center
25	120	10	30	shape 2	Right
26	75	10	60	Cubic chamber	Left
27	75	10	60	Cubic chamber	Right
28	75	10	60	shape 2	Right
29	75	10	60	shape 2	Left

3. Results and discussion

3.1. Experimental and validation results

In order to verify the accuracy and reliability of the CFD model that has been used for the solar dryer analysis, the results of numerical modeling are compared with those obtained experimentally. *Figure 3.7* and *Figure 3.8* exhibit the temperatures of SAH outlet and inside the drying chamber that obtained from experiences versus the predicted values by the CFD model. A good agreement between the predicted and the experimental values is observed with the mean relative error ranged between 3.5 – 8.96% for the SAH outlet temperature and between 0.1 – 6.42% for the drying chamber temperature, which can be compared to the average errors of 3% and 9.02% mentioned by *(Heydari & Mesgarpour, 2018)* and *(Abhay et al., 2018)*, respectively. These deviations were attributed to the used boundary conditions, i.e. adiabatic boundary condition on the surrounded insulated walls. Furthermore, during the experimentations, some leakage may occur through duct joints.

Remarkable temperature differences in the solar dryer components are noted in the experimental and numerical results corresponding with the solar intensity, i.e. the temperature elevates linearly in all solar dryer components with the increase of the solar intensity. In the connection with *Figure 3.7*, it is observed that the double pass SAH increased the air temperature by 20 °C, and the SAH's outlet temperature reaches a maximum value of 55°C at 800 W/m^2 solar intensity. The maximum temperature observed in the drying chamber center was 54 °C.

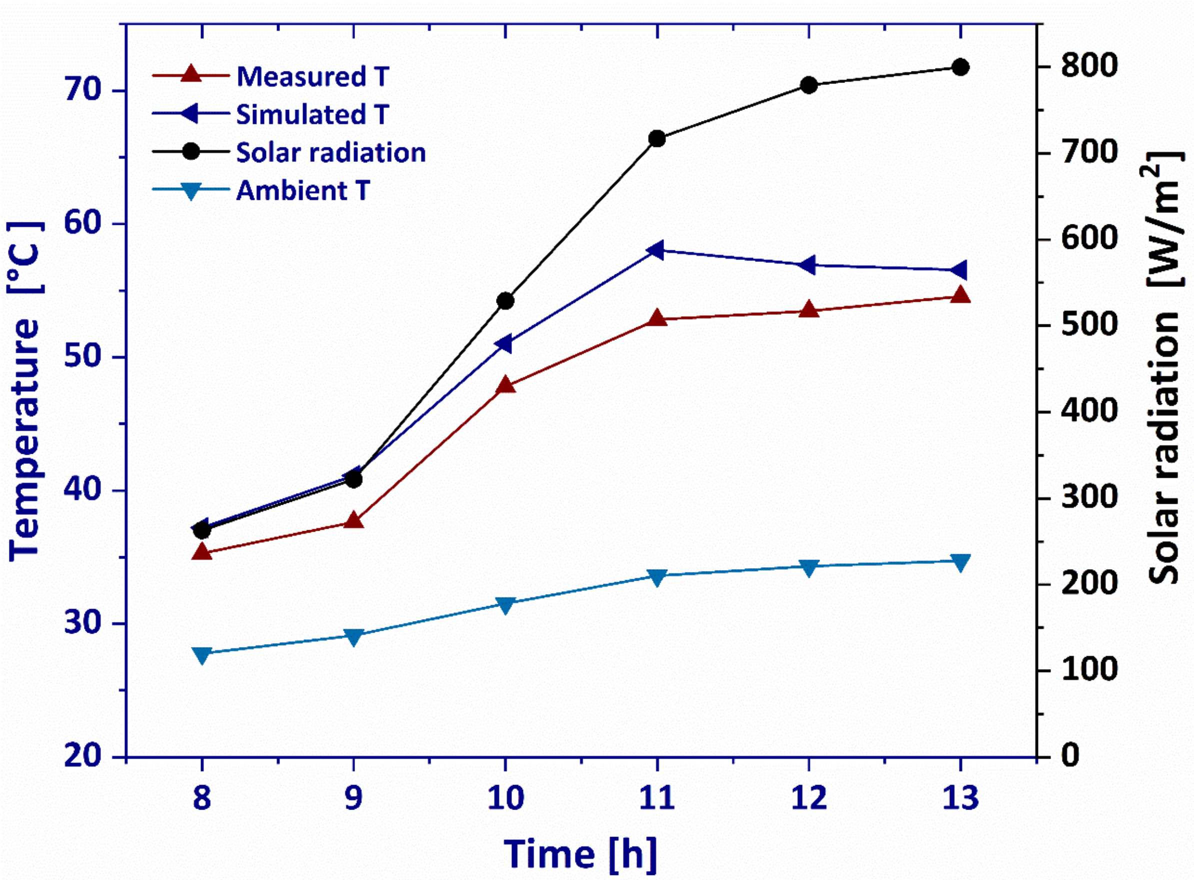

Figure 3.7 Measured and simulated SAH outlet temperature.

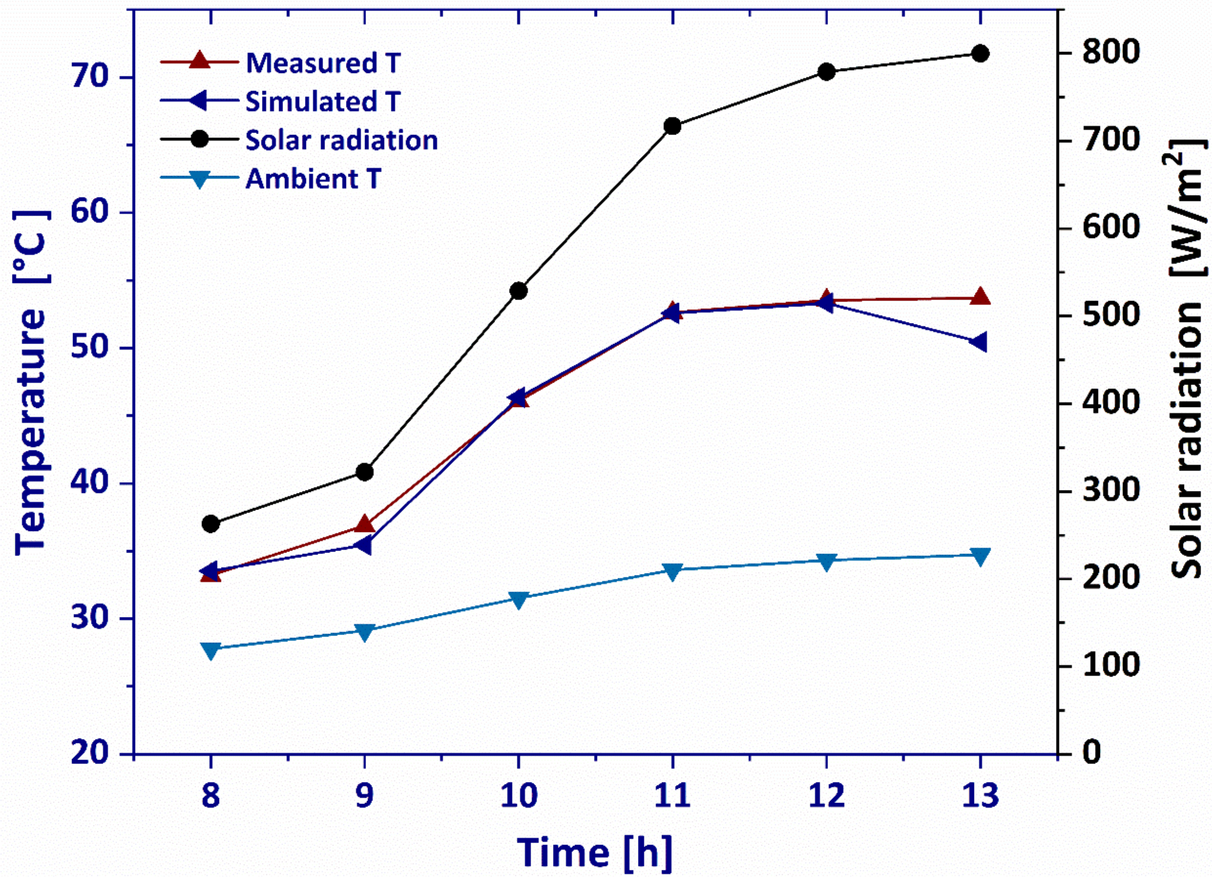

Figure 3.8 Measured and simulated drying chamber temperature.

3.2. Analysis of variance

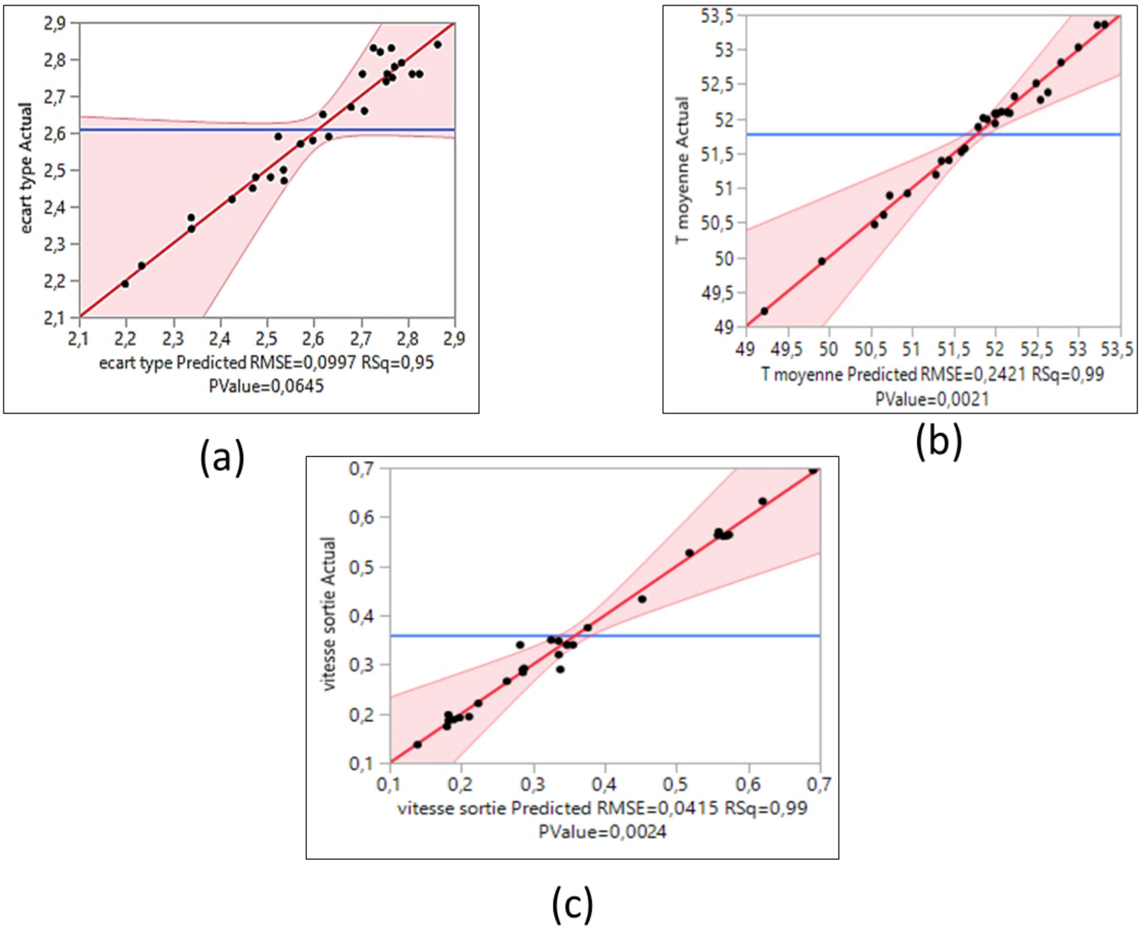

Figure 3.9 Predicted versus actual values for the RSM models (a) Standard deviation (b) Average temperature (c) Outlet velocity with the analytical data. The 45° straight line illustrates a perfect fit.

The *Figure 3.9* shows a linear relation between these values which testifies to the good adequacy between the answers which can be obtained by the experimental model and those which could be predicted by the mathematical relation proposed starting from the MPE. Moreover, we can obtain the response surfaces for each of the responses and which will be presented later.

The analysis of the results of these experiments on the three responses standard deviation (Y1) and mean temperature (Y2) and output speed (Y3) could be carried out using the JMP software.

It can be seen from the linear regression coefficient (R2) calculated on the responses Y1 and Y2 and Y3 shown in *Figure 3.9* that the model studied is satisfactory. In fact, this coefficient being greater than or equal to 0.9, this indicates that more than 90% of the variables are explained by the model.

3.3. Pareto chart

The Pareto chart in Figures Figure 3.10 to Figure 3.12 shows all the effects of the parameters and their interactions in decreasing order of importance. The sign (+) indicates a positive contribution of the effect, while the sign (-) indicates a negative contribution *(BADACHE, 2013)*.

In the case of the standard deviation, we have only two main effects (shape of the rectangular chamber, the position of the chimney in the center) and three interactions (central position with the rectangular shape, the angle of inclination with rectangular shape and height of the chimney with the air gap).

And in the case of the average temperature, there are three main effects (the shape of the rectangular chamber and the position of the chimney to the left and the air space) and four significant interactions (height of the chimney with the position in the center , height with the rectangular shape, air gap with the position of the chimney in the center, the angle of inclination with the central position).

Term	Orthog Estimate
forme de la chambre[rectangle]	0,0801570
position[centre]*forme de la chambre[rectangle]	-0,0788039
angle incline*forme de la chambre[rectangle]	0,0703029
hauteur de chimene*lame d air	-0,0654579
position[centre]	-0,0520168
angle incline*angle incline	0,0376395
lame d air*lame d air	-0,0343755
lame d air*position[centre]	0,0324392
hauteur de chimene*position[gauche]	-0,0319447
hauteur de chimene(30,120)	0,0259811
lame d air*angle incline	0,0226358
hauteur de chimene*position[centre]	0,0158174
hauteur de chimene*forme de la chambre[rectangle]	-0,0151869
angle incline(30,90)	-0,0145939
lame d air(5,15)	-0,0120657
angle incline*position[centre]	0,0099692
hauteur de chimene*hauteur de chimene	-0,0094542
angle incline*position[gauche]	0,0046230
position[gauche]*forme de la chambre[rectangle]	0,0043840
hauteur de chimene*angle incline	-0,0031171
lame d air*forme de la chambre[rectangle]	0,0029577
lame d air*position[gauche]	-0,0006914
position[gauche]	0,0003556

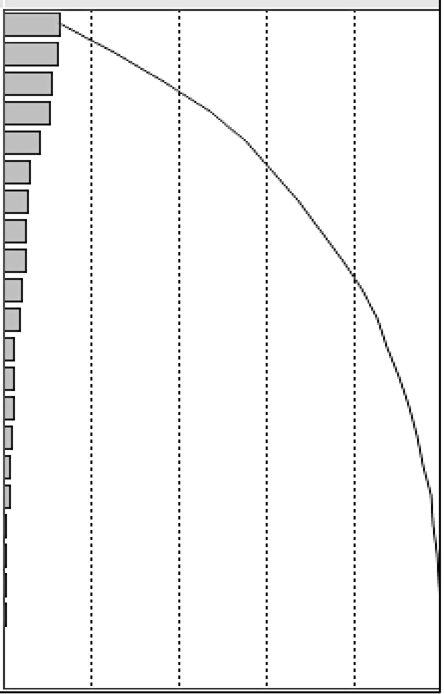

Figure 3.10 Pareto chart for the Standard deviation

And concerning the case of the speed at the exit of the chimney we notice two necessary effects (the air space which clearly affects both the height of the chimney and the rectangle shape with less effect) and three significant interactions (the tilt angle with the shape of the rectangular chamber, the height of the fireplace with the tilt angle, and the position of the fireplace to the left with the tilt angle).

Note: all interactions that have a very weak effect can be eliminated.

Term	Orthog Estimate
forme de la chambre[rectangle]	-0,5102195
position[gauche]	-0,3775863
lame d air(5,15)	-0,3611026
hauteur de chimene*position[centre]	-0,3171513
hauteur de chimene*forme de la chambre[rectangle]	-0,2455492
lame d air*lame d air	-0,2116087
lame d air*position[centre]	-0,1971218
angle incline*position[centre]	0,1557706
position[centre]	0,1143521
position[gauche]*forme de la chambre[rectangle]	-0,1084941
lame d air*forme de la chambre[rectangle]	-0,0660536
lame d air*angle incline	0,0656719
angle incline*forme de la chambre[rectangle]	-0,0628799
angle incline*position[gauche]	-0,0615727
position[centre]*forme de la chambre[rectangle]	-0,0526347
hauteur de chimene(30,120)	-0,0454485
angle incline(30,90)	0,0399675
lame d air*position[gauche]	-0,0328541
hauteur de chimene*angle incline	-0,0176467
hauteur de chimene*lame d air	-0,0164660
angle incline*angle incline	0,0149141
hauteur de chimene*position[gauche]	0,0115501
hauteur de chimene*hauteur de chimene	0,0076832

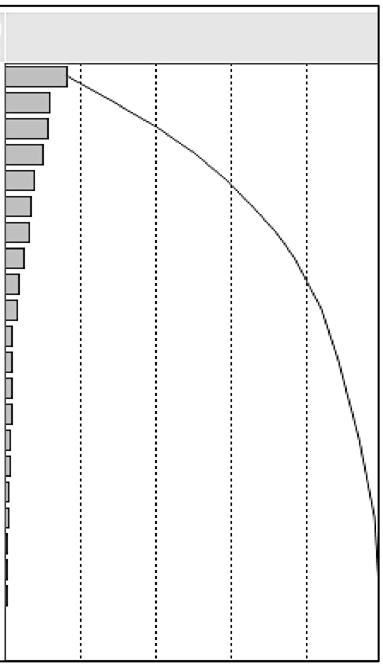

Figure 3.11 Pareto chart for the average temperature

Term	Orthog Estimate
lame d air(5,15)	-0,1421265
hauteur de chimene(30,120)	-0,0269618
lame d air*lame d air	0,0265085
forme de la chambre[rectangle]	-0,0232475
angle incline*forme de la chambre[rectangle]	0,0217841
hauteur de chimene*hauteur de chimene	0,0181863
hauteur de chimene*angle incline	0,0163097
angle incline*position[gauche]	-0,0126358
position[gauche]	0,0114184
angle incline(30,90)	-0,0099177
angle incline*angle incline	-0,0094809
lame d air*position[centre]	0,0090831
angle incline*position[centre]	-0,0074510
position[gauche]*forme de la chambre[rectangle]	0,0066030
lame d air*forme de la chambre[rectangle]	0,0056765
lame d air*position[gauche]	-0,0055913
hauteur de chimene*forme de la chambre[rectangle]	0,0052293
hauteur de chimene*position[gauche]	-0,0039808
lame d air*angle incline	0,0031628
hauteur de chimene*position[centre]	-0,0027984
hauteur de chimene*lame d air	-0,0021461
position[centre]	-0,0010008
position[centre]*forme de la chambre[rectangle]	0,0009371

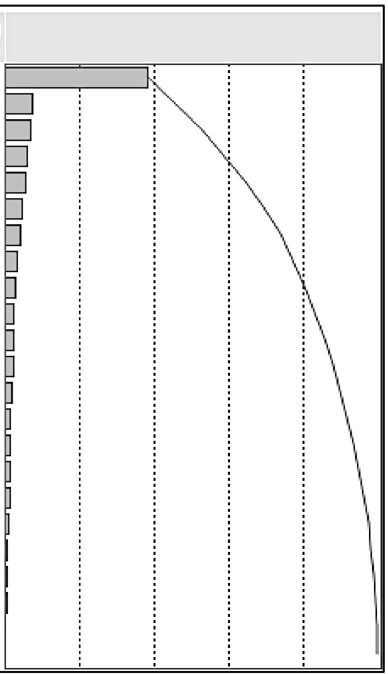

Figure 3.12 Pareto chart for the outlet Velocity

3.4. Effect of Chimney length, Chimney width and Chimney angle on standard deviation

The models predicted by the JMP software make it possible to plot response surfaces; (*Figure 3.13* and *Figure 3.14*) as an example. The response surface represents the variation of a response as a function of two influencing factors. We recall that we will seek to minimize the value of the standard deviation in all the simulations performed.

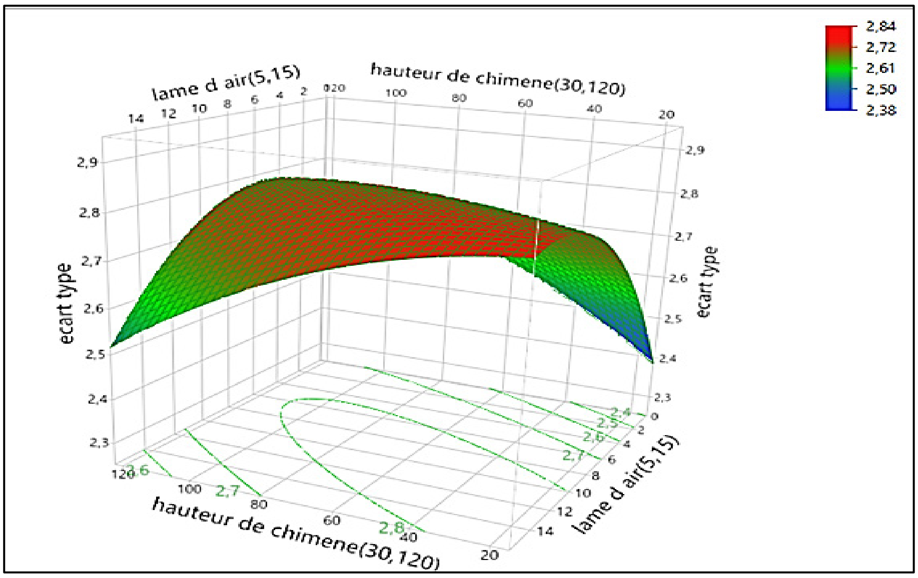

Figure 3.13 Effect of Chimney length, Chimney width on the standard deviation

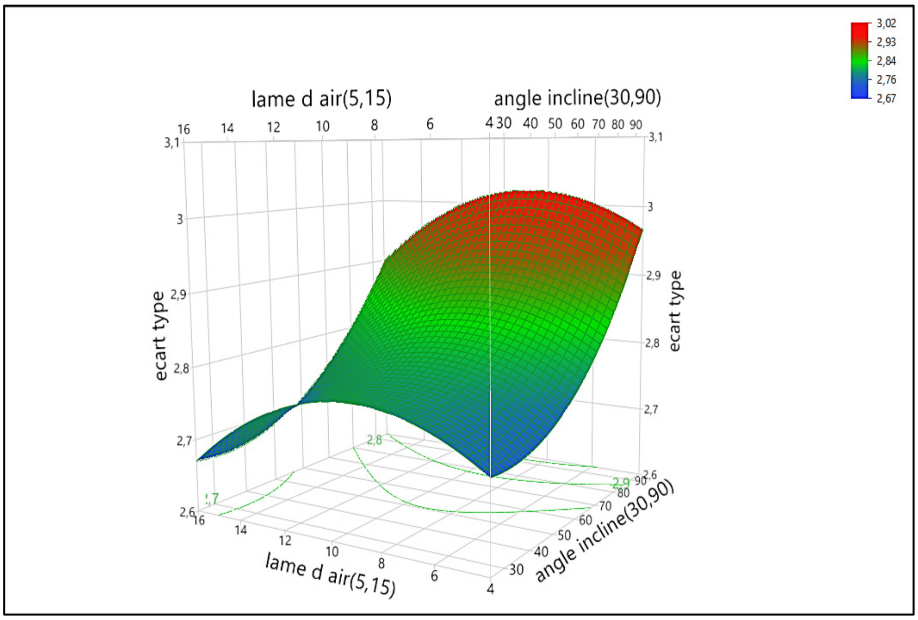

Figure 3.14 Effect of Chimney angle on the Standard deviation

The temperature standard deviation has a minimum value between 2.4 and 2.5 when the height and air gap of the chimney are simultaneously either at level +1 or at level -1. On the other hand, it takes its maximum value 2.84 for the +1 air gap level with the minimum height.

The blue area represents the best values of the tilt angle for a homogeneous temperature distribution in the drying chamber, so we conclude from the previous curve that the optimal tilt angle is 30 °.

3.5. Effect of Chimney length, Chimney width and Chimney angle on average temperature

It can be deduced from the curve illustrated in *Figure 3.15* that the minimum values of the air gap and the length of the chimney give the best value of the average temperature in the drying chamber. What is represented by a red area of the response surface.

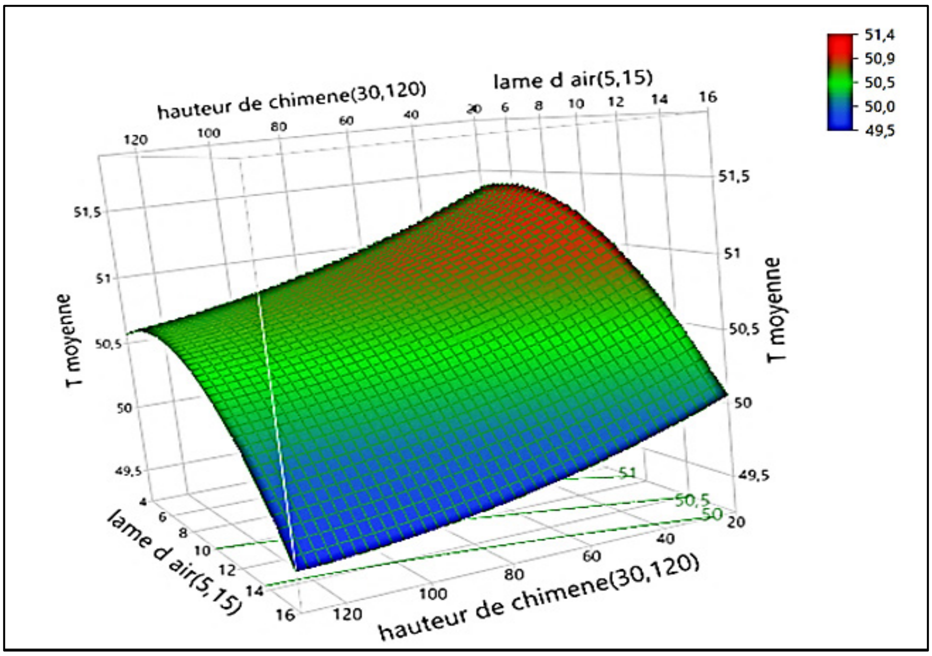

Figure 3.15 Effect of chimney length, chimney width on the average temperature

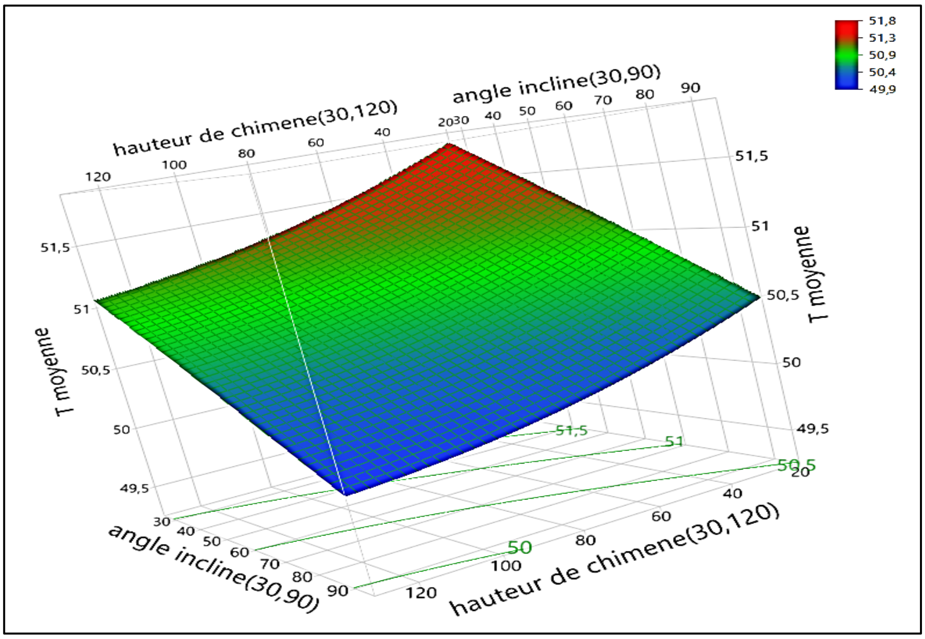

Figure 3.16 Effect of chimney angle on average temperature in the drying chamber

The curve shown in *Figure 3.16* shows that the tilt angle of the chimney does not have a significant effect on the average temperature in the drying chamber because minimizing the angle can increase the temperature by a value of approximately 0.75 ° C for level +1 of the chimney height, while for level -1 of the latter the temperature can be increased with 1.5 °C.

3.6. Effect of Chimney length, Chimney width and Chimney angle on outlet velocity

The *Figure 3.17* shows that the maximum value of the outlet speed is obtained when the values of the height and the air gap and the chimney blade are minimum. In fact, the extraction speed directly affects the drying time where, increasing the speed at the exit speeds up the drying process.

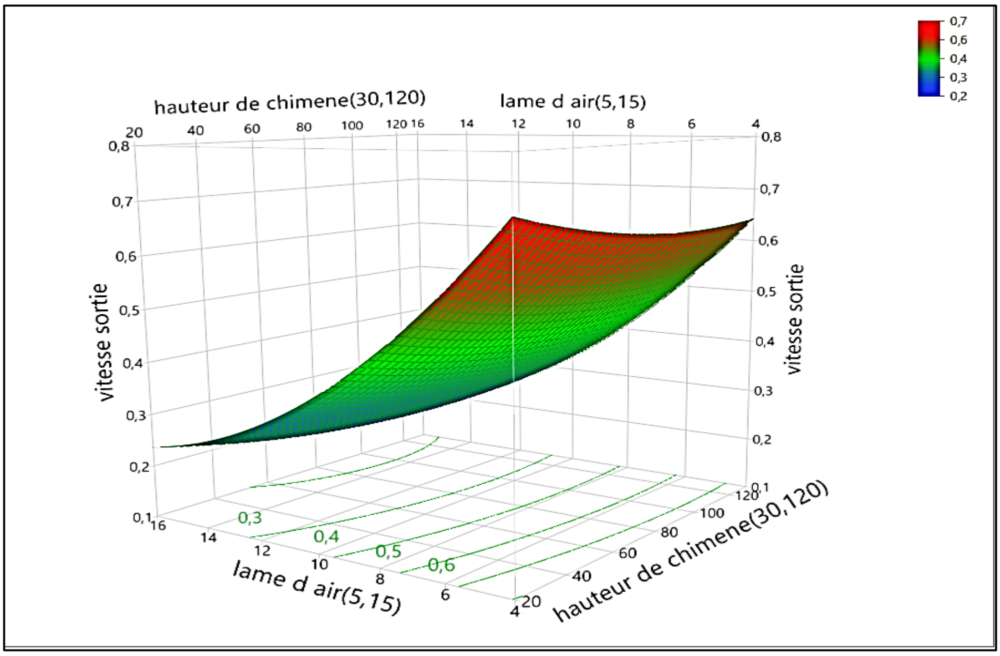

Figure 3.17 Effect of Chimney length, Chimney width on the Outlet velocity

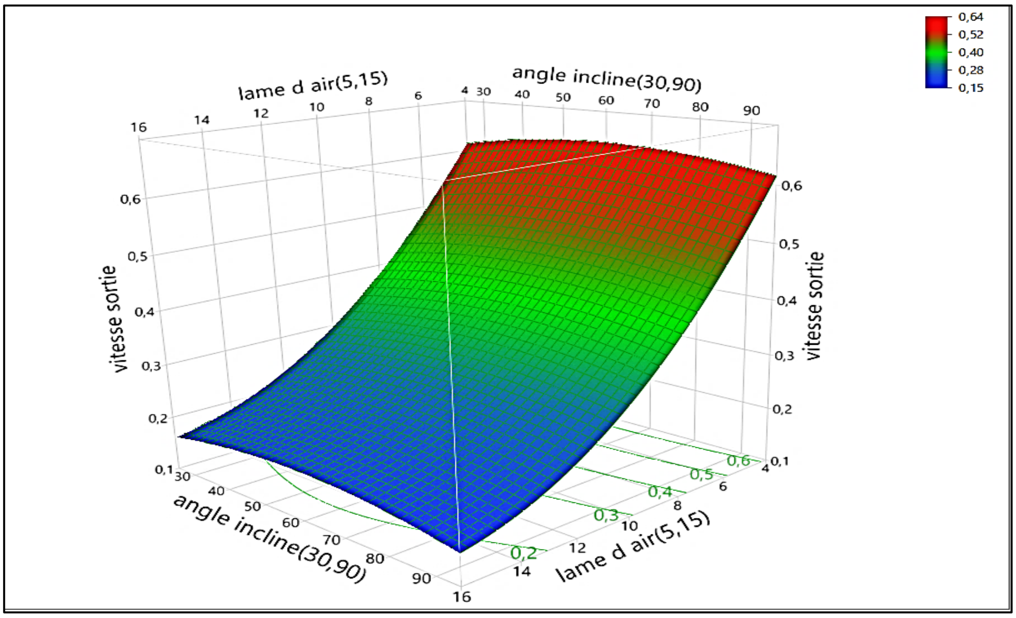

Figure 3.18 Effect of chimney angle on the Outlet velocity

We notice from the curve in that the bank angle does not significantly affect the exit speed.

4. Optimum design of the solar dryer

After the results extracted by the DoE and after having linked the probabilities of the factors for the best value of the desired responses, we found three shapes that provided an improvement over the real shape of the indirect solar dryer manufactured by the LENREZA laboratory. In order to verify the extent of improvement; three answers were chosen. The first is the speed at the exit since it directly affects the duration of the drying where the second parameter is the standard deviation of the temperature in the drying chamber, which leads to a greater uniformity of the distribution of the drying temperature. for its minimum value. As well as the relative increase in the average temperature (third response) in the drying chamber which positively affects the drying operation. This is explained by the following (Table 3.7 and Table 3.8):

length, width, position and angle of inclination of the chimney and the shape of the chamber

Table 3.7 Optimal values of input parameters and responses

Paramètre de géométrie	Goal	Baseline design	Candidate N° 1	Candidate N° 2	Candidate N° 3
Air duct thickness (m)		0 ,085	0.05	0.05	0.05
Chimney height (m)		1.00	0.2	0.3	0.4
inclination angle of the chimney		90	52	52	45
Chimney position		Center	Center	Center	Center
Drying chamber shape		Cubic chamber	Shape 2	Shape 2	Shape 2

Table 3.8 Three optimal candidates with regard to the desired objectives.

	Baseline design	Candidate N°1	Candidate N°2	Candidate N°3
Standard deviation	2.74	2.37	2.51	2.48
Average temperature (°C)	51.37	51.81	51.73	52.39
Output velocity (m/s)	0.38	0.660	0.661	0.66

4.1. Simulation of the optimal designs

Candidate N°1

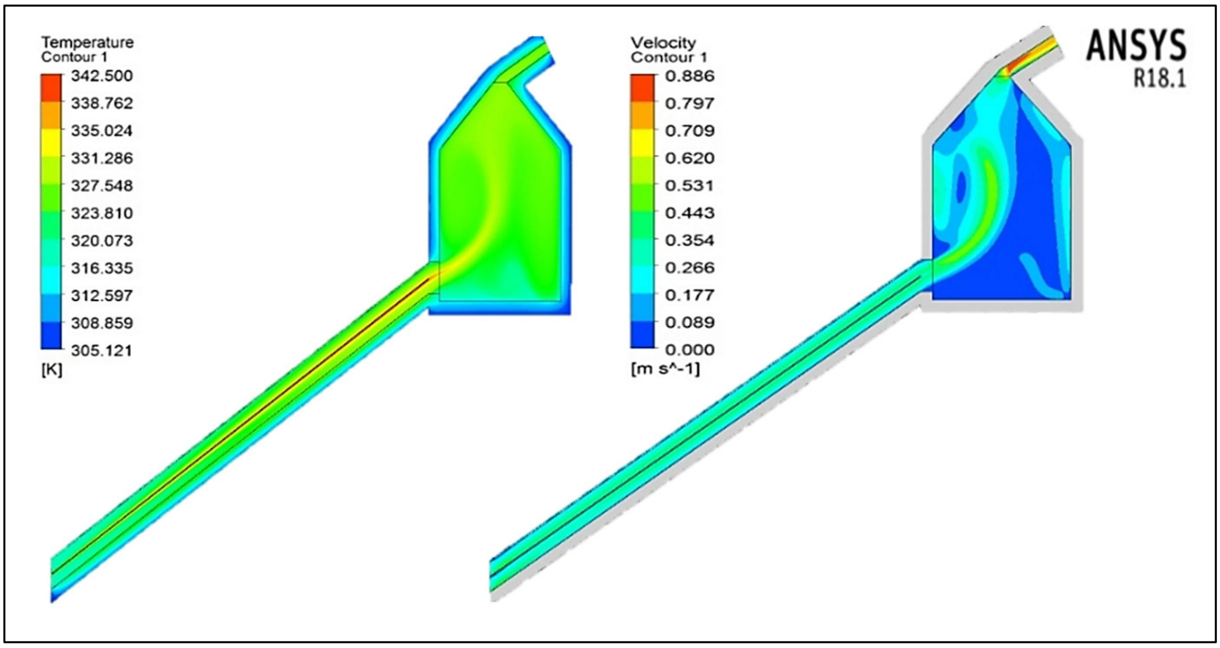

Figure 3.19 Temperature and velocity distributions inside the optimal design N°1

Candidate N°2

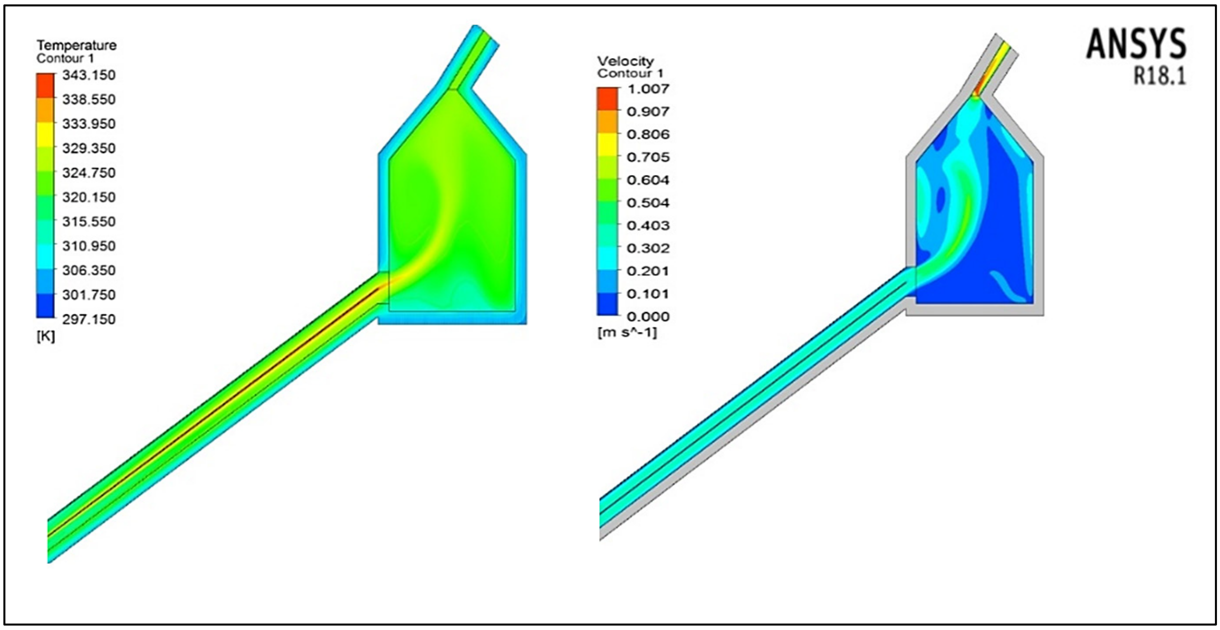

Figure 3.20 Temperature and velocity distributions inside the optimal design N°2

Candidate N°3

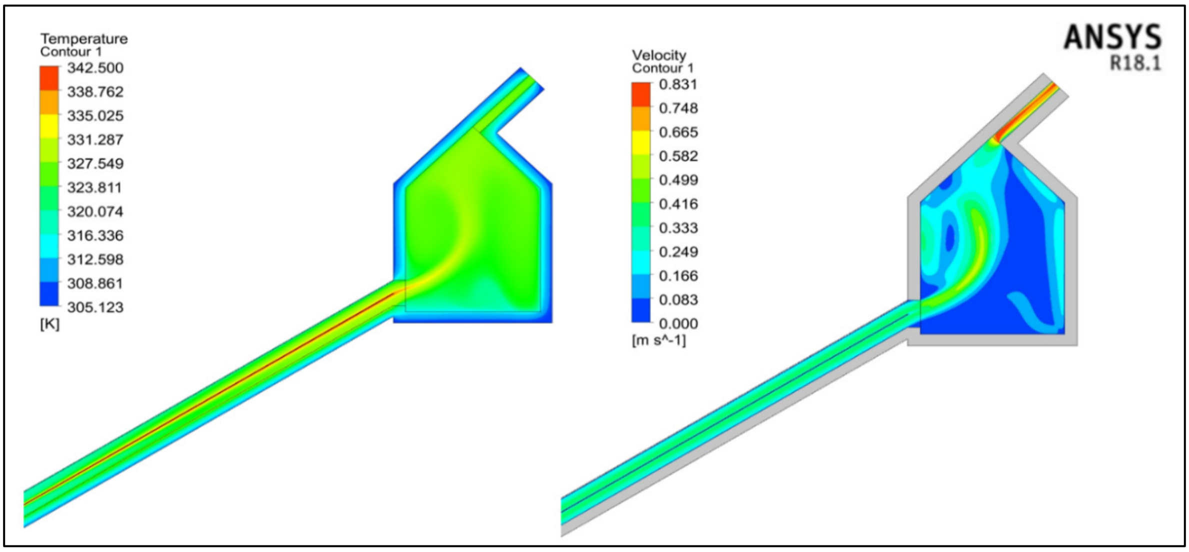

Figure 3.21 Temperature and velocity distributions inside the optimal design N°3

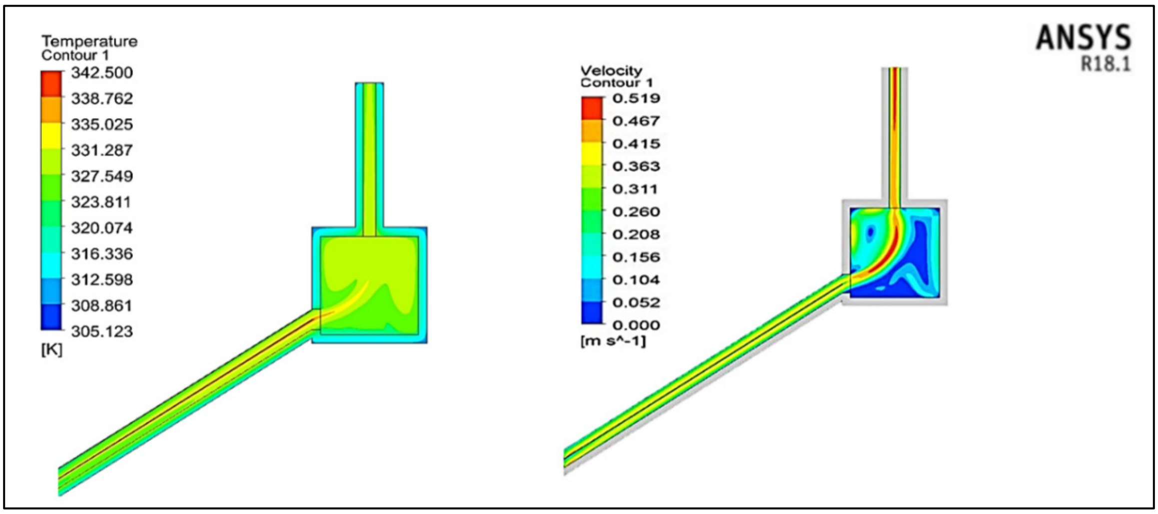

Figure 3.22 Temperature and velocity distributions inside the baseline SD design

The FiguresFigure 3.19 Figure 3.20 ,and Figure 3.21 represent the contours of the temperature distribution and the speed of the optimal designs. In these figures it is clearly illustrated the difference in distribution and the value of the speed compared with the real state (*Figure 3.22*) and we notice that the curves have similar values. We also note that the design # 3 has a higher temperature compared to other N°1, N°2 designs.

5. Conclusion

In the current chapter, a two-dimensional quasi-steady numerical model based on CFD was developed and validated experimentally. Moreover, the drying uniformity, temperature, and velocity of drying air was studied numerically. The importance of using DoE methodology side to side with CFD in order to carry out a parametric study on the drying chamber was highlighted.

The Results from the numerical model established herein demonstrate reasonable agreement with the results obtained from the experimental investigation. The effect of five parameters on the uniformity of air distribution was investigated. The shape of the chamber and the position of the chimney are the main variables. While the height and angle of inclination of the fireplace have a secondary influence.

Following the optimization process developed on the JMP software, the final result obtained for the optimal conditions allowing to maximize the average temperature and the speed at the exit of the chimney is such that: the air gap 0.05m; the height of the chimney 0.2 m; the chimney tilt angle 52 ° with a centrally positioned chimney and a 45 ° angled drying chamber. The optimal design was compared with the original design and relative improvement in the outlet speed were observed where it reached 0.66 m / s. The standard deviation was 2.37 and the average drying temperature was 52.39 ° C. Note here that the results of the tests previously carried out in the LENREZA laboratory for the actual condition of the dryer, gave an output speed of 0.38 m/s, a standard deviation of 2.74 and an average temperature of 51.37 °C.

CHAPTER 4 DRYING UNIFORMITY ANALYSIS WITHIN AN INDIRECT SOLAR DRYER USING IMAGE PROCESSING

1. Inroduction

This chapter aimed to test the ability of using image processing technique side to side with the CFD simulation of the air flow inside the drying chamber in order to enhance drying uniformity of solar dryers. Therefore, the experimentally validated numerical model of the ISD (presented in the previous chapter) has been used to obtain the air flow distribution for different geometries and operating conditions. The effect of air mass flow rate and as well as the effect of exploiting solar chimney connected to drying chamber, have been investigated. To compare the drying uniformity of active mode and passive mode with adding a solar chimney to enhance air motion inside the drying chamber image processing to achieve uniform velocity and temperature distributions throughout the drying chamber. image processing technique is proposed in order to cover the shortcomings of the standard deviation parameter.

2. Material and methods

2.1. Problem solution procedure

The main followed steps to carry out this parametric study process using image processing and CFD were the experimental tests, CFD modeling and parametric study (*Figure 4.1*) where the detailed followed steps are:

1. The experimental tests have been performed in a typical clear sky day.
2. The experimental conditions have been applied as boundary conditions to solve the governing equations (please see *Section 2.1* in *CHAPTER 3*).
3. The grid independence test has been checked after drawing the IDS, defining inputs and parameters, meshing and solving the governing equations.
4. The numerical model has been validated based on the experimental results.
5. The effect of adding a passive chimney and the effect of four mass flow rates on the drying air distribution is tested by solving energy balance and Navier-stokes equations using ANSYS FLUENT software.
6. The CFD results has been analyzed using Digital image processing as it provides precise comparative way compared to the visual reading of contours of velocity and temperature distribution.
7. The Optimum ISD design and operating that ensure the uniform distribution were selected based on the previous step.

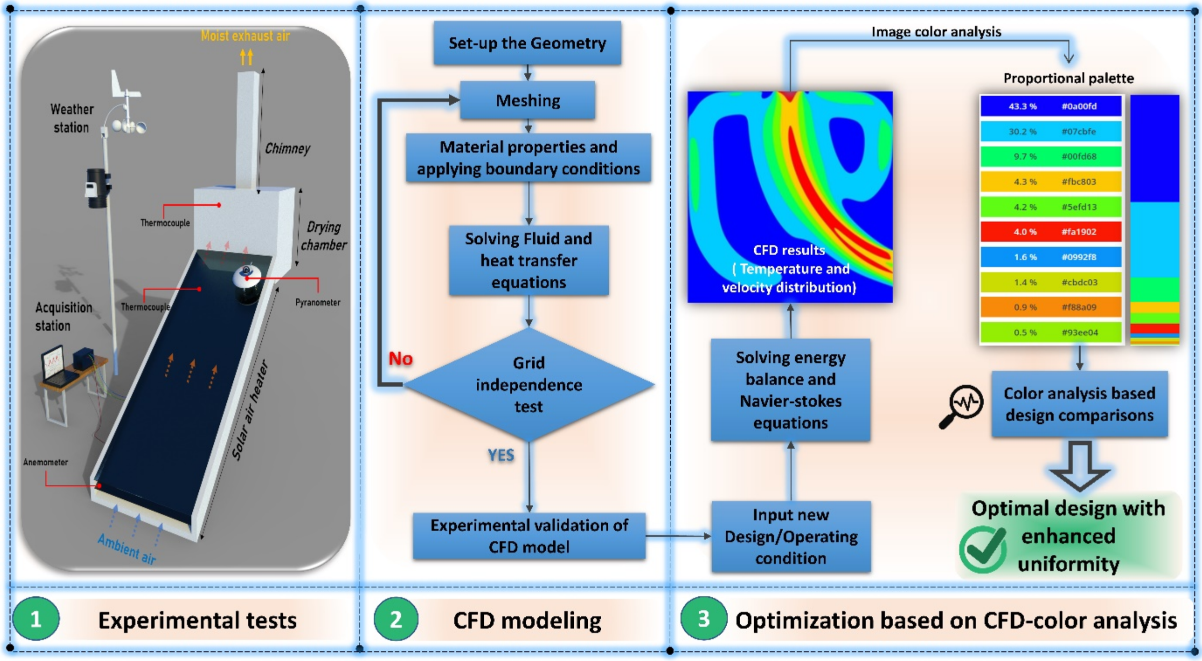

Figure 4.1 Flow chart of the CFD simulation and the optimization process.

2.2. Image processing

After carrying out the numerical parametric study using the validated CFD model, an image processing technique has been used as a tool to define the best design and operating conditions. This proposed technique was based on the analysis of the CFD results, mainly image processing of the images of temperature air flow distributions inside the drying chamber. For this purpose, Multicolor Engine software has been used to calculate the percentage of each specific color in the image. The parametric study process and the selection procedure of the best design based on image processing of the CFD results is presented as flow chart in *Figure 4.2*.

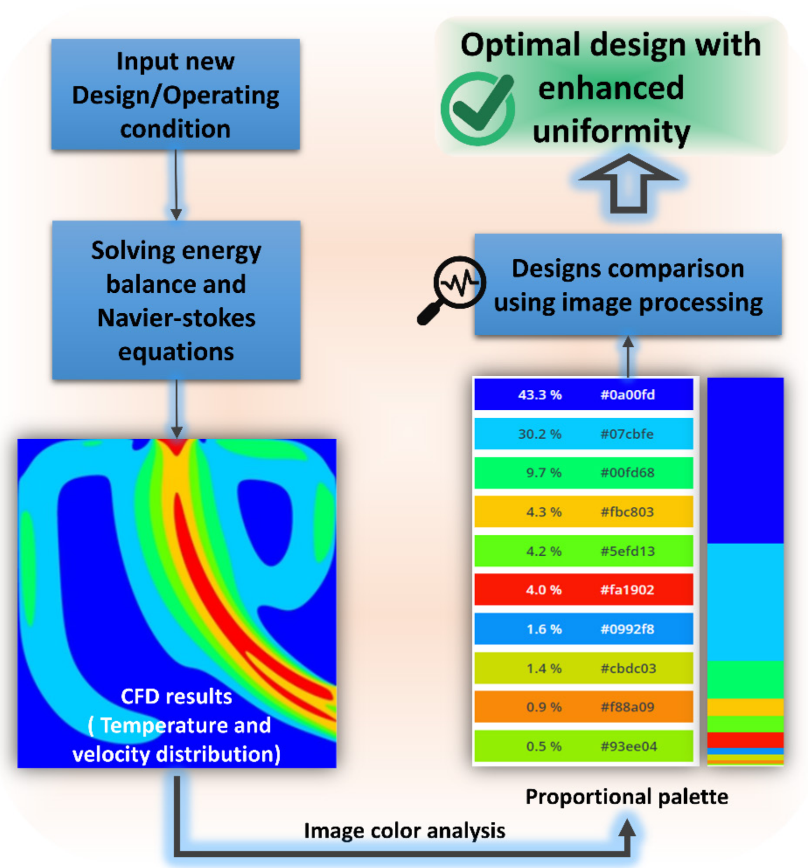

Figure 4.2 Image processing of the CFD results.

MulticolorEngine is an application programming interface API developed by TinEye (an image search and recognition company that is expert in computer vision, pattern recognition, neural networks and machine learning). It analyzes the pixels in the images to extract the color in each individual pixel, then the similar colors are classified after identifying the dominant colors in the image. For each color, a similarity rank, a weight factor, and a color class are returned along with the RGB values. The weight specifies the importance of a color relative to all other colors in the image. For example, if several colors are extracted from a single image, a weight of 23.0 means that the associated color covers 23.0% of the image, and the rest colors together cover 77.0% of the image. This technique also could be programmed using MATLAB, Python or any other programming language. However, in this study this software has selected because it free and trusted by Adobe, Agence France-Presse and other international companies (https://labs.tineye.com/color/) *(Poveda, 2020)* furthermore, it offers several advantages such as: 1) It is fast, accurate and scales to any size image collection. 2) it Extracts color palettes from individual images or sets of images; 3) it ignores solid and transparent backgrounds in images.

To increase the accuracy of the results obtained from the image processing, the images to be analyzed are plotted using the CFD results and extracted in similar conditions. (5 colors varied from blue to red) the minimum velocity to the max velocity in the numerical simulation.

3. Results and discussion

This section has been ordered as follows; firstly, the CFD model validation with experimental results has been provided. Next, the results of the mass flow rate effect and those of replacing the ordinary chimney by a solar one have been discussed separately. Finally, the image processing of CFD results for all configurations has been presented in the last section in order to judge the best configuration that enhanced the drying uniformity.

3.1. Mass flow rate effect

In the drying chamber the heated air evaporates the water inside the product after absorbing the thermal energy carried by the air. In natural convection ISDs the air passes through drying chamber due to the buoyancy effect. Alternatively, in the forced convection ISDs blowers or fans are used to improve the airflow rate *(Mugi & Chandramohan, 2020)*.

To investigate the effect of forced convection on the drying uniformity, the CFD simulation has been carried out for the witness solar dryer with natural convection and three configurations for the forced convection with different mass flow rates, namely, $\dot{m}$=0.0141, 0.0636, and 0.0872 kg.s^{-1} *(Vijayan et al., 2016; Vijayan, Arjunan, & Kumar, 2020; Vijayan, Arjunan, Kumar, et al., 2020)*. Thus, in the simulation software, the drying air circulation has been forced using a virtual fan with possibility of variation in air flow where it is placed in the outlet of the solar dryer, the temperature distribution and airflow velocity fields for all the configurations were predicted, and the results are discussed in this section.

To ensure best comparison between the simulated solar dryers, the temperature distribution was shown for the same selected range (308 K- 343K). *Figure 4.3* demonstrates the influence of the applied mass flow rates on the temperature distribution inside the ISD, where the best temperature uniformity was observed for $\dot{m}$ = 0.0141 kg.s^{-1}. Moreover, the average temperature in the drying chamber is higher in case of using forced convection compared to natural convection. An average temperature of T = 319 K was obtained for the natural convection, whereas for the forced convection, the obtained temperatures were T = 335, 330 and 327 K for the mass flow rate of $\dot{m}$ = 0.0141, 0.0636, and 0.0872 kg.s^{-1}, respectively.

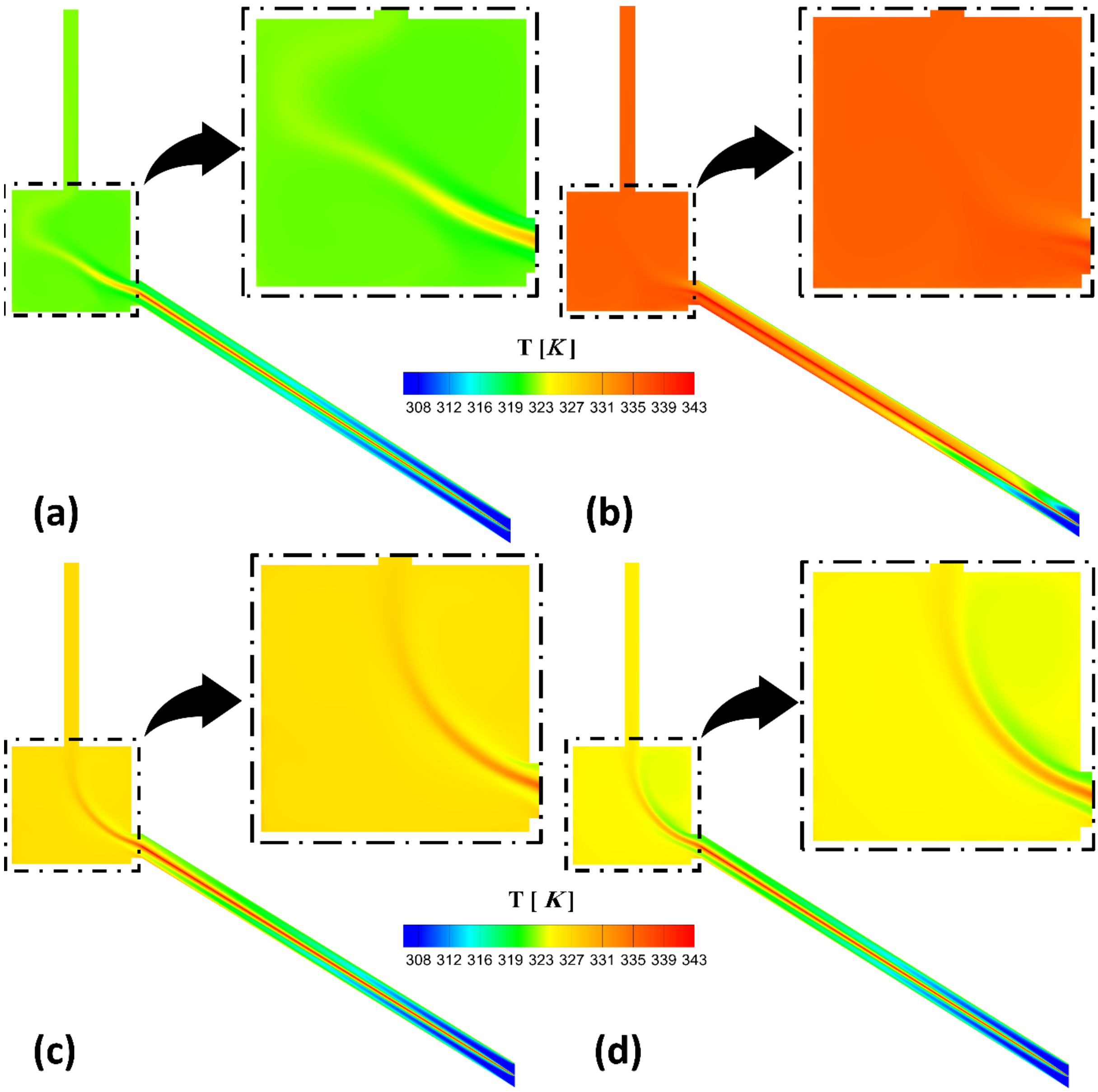

Figure 4.3 Temperature distribution (a) natural convection (b) forced convection with $\dot{m}$ = 0.0141 kg.s^{-1} (c) FC with $\dot{m}$ = 0.0636 kg.s^{-1} (d) FC with $\dot{m}$ = 0.0872 kg.s^{-1}.

The drying uniformity is related also to the air flow velocity fields in the drying chamber. The effect of a) natural convection versus forced convection with b) $\dot{m}$ =0.141 kg.s^{-1}, c) $\dot{m}$ =0.0636 kg.s^{-1} and d) $\dot{m}$ =0.0872 kg.s^{-1}) is shown in *Figure 4.4*. The maximum velocity inside the drying chamber was V= 1.2 m/s for the natural convection, while for the forced convection it was V=0.16, 0.533 and 0.718 m/s for the air flow of $\dot{m}$ = 0.141, 0.0636, and 0.0872 kg.s^{-1}, respectively. On the other hand, the minimum velocities were found to be 0.1, 0.02, 0.05, and 0.1 m/s for the SD with natural convection, SD with $\dot{m}$ = 0.141, $\dot{m}$ = 0.0636 and $\dot{m}$ = 0.0872 kg.s^{-1}, respectively.

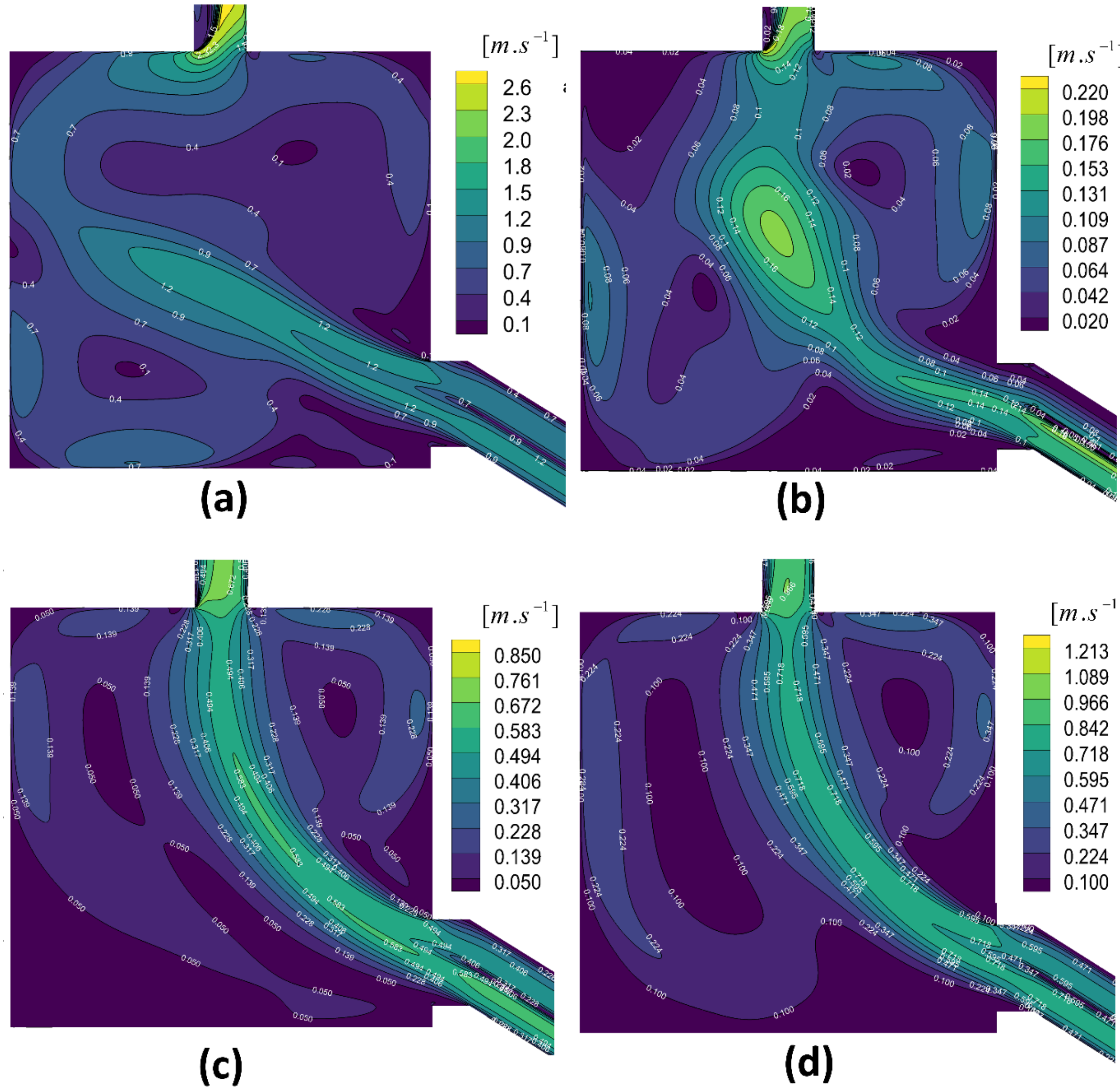

Figure 4.4 Velocity distribution (a) natural convection (b) forced convection with $\dot{m}$ = 0.0141 kg.s^{-1} (c) forced convection with $\dot{m}$ = 0.0636 kg.s^{-1} (d) forced convection with $\dot{m}$ = 0.0872 kg.s^{-1}.

3.2. Solar chimney effect

The effects of using solar chimney on the temperature and airflow velocity distributions in the drying chamber are shown in *Figure 4.5* and *Figure 4.6*, respectively. It is observed from *Figure 4.5* that the maximum drying chamber temperature was 326K for the SD with solar chimney and 319K for SD with ordinary chimney. Therefore, using solar chimney improves the drying air temperature by 7 degrees. In addition, the velocity fields were in the ranges of 0.1 - 1.2 m/s for the SD with ordinary chimney and 0.243 m/s - 0.971 m/s for the SD with solar chimney, as shown in *Figure 4.6*. It is remarked that replacing the ordinary chimney by a solar one may enhance the air flow velocity inside the drying chamber by increasing the minimum velocity from 0.1 to 0.243 m/s.

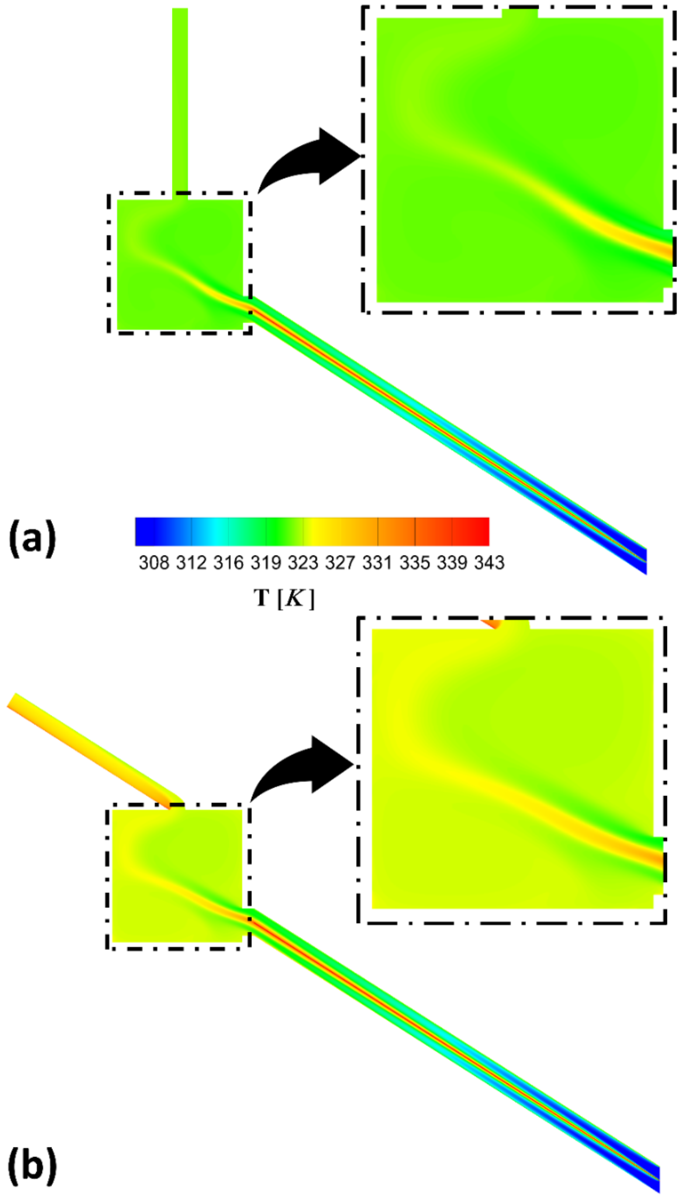

Figure 4.5 Temperature distribution (a) ordinary chimney (b) solar chimney.

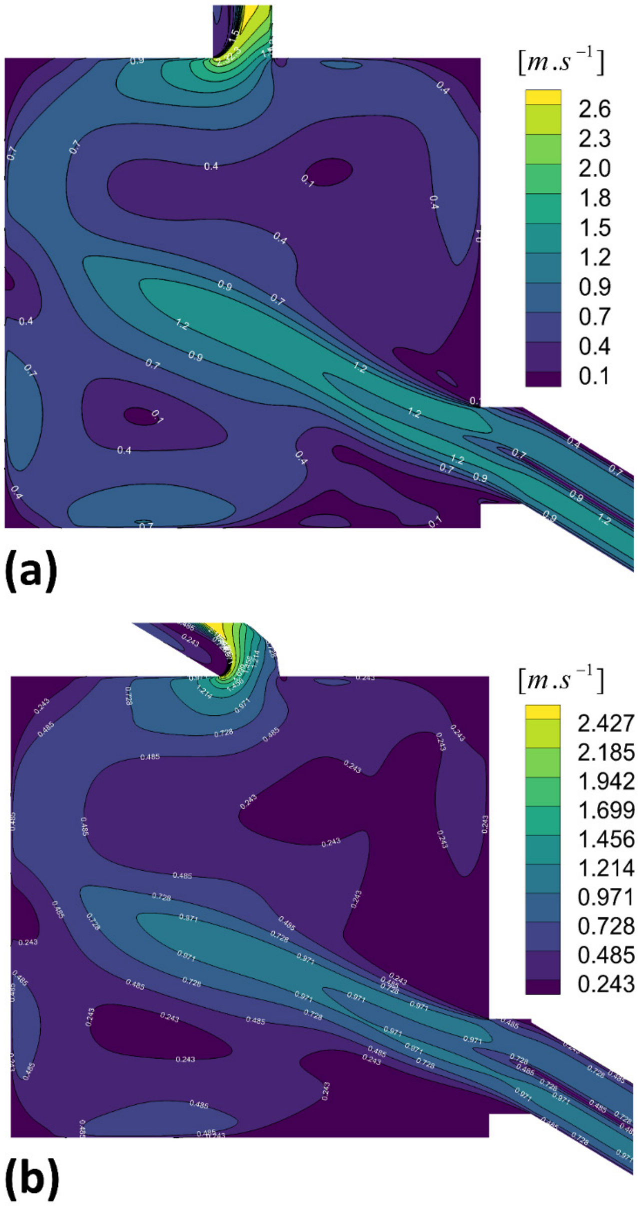

Figure 4.6 Velocity distribution (a) ordinary chimney (b) solar chimney.

3.3. Uniformity analysis using image processing

To define the best SD configuration that ensures uniform drying of the agri-food products, image processing method is used as a precise way compared to the visual reading of contours of velocity and temperature distributions obtained from the CFD software. In this section the image processing procedure was used for the selection purpose between the five studied configurations (SD with passive ordinary chimney, SD with passive solar chimney and SD operates in active mode at three mass flow rates $\dot{m}$=0.0141, 0.0636 and 0.0872 kg.s^{-1}). The results of images processing presented in this section were obtained based image processing of five contours of temperature distribution and five contours of velocity fields inside the drying chamber. Every design has been analyzed individually for both temperature and velocity fields and the percentage of each specific color in the image has been calculated as presented in the section 2.2 of this Chapter.

An example of extracted color palette using image processing of one of CFD results images is presented in *Figure 4.7* where the source image is the image of temperature distribution obtained from ANSYS fluent, the color map regions are the colors after treatment by MulticolorEngine where the similar colors are approximated, the proportional palette represents the proportion of each color in the image. This analysis was applied to the all the figures of air temperature distribution and velocity fields for the all the studied configurations. The image processing results are summarized in Table 4.1, however, the additional details are presented in *Appendices C* and *D*.

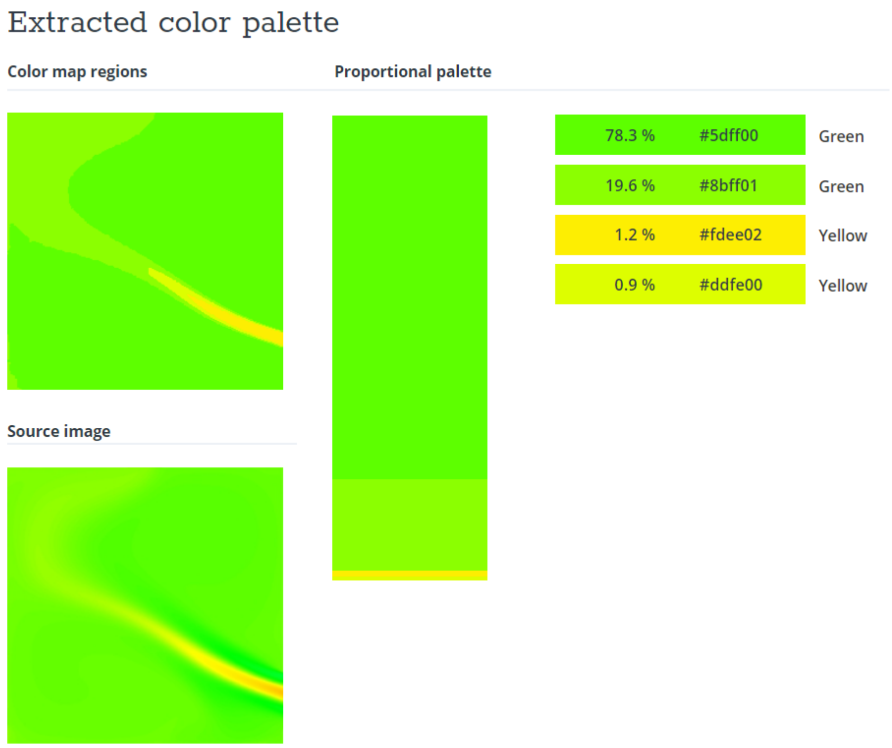

Figure 4.7 Sample of extracted color palette for naturel convection with ordinary chimney.

Table 4.1 Temperature and velocity uniformity study using image processing.

Modification	Temperature uniformity %		Velocity uniformity %	
	1st dominated color (%)	2nd dominated color (%)	1st dominated color (%)	2nd dominated color (%)
Natural with ordinary chimney	78.3	19.6	42.7	40
Natural with solar chimney	41	37.2	55.9	31.5
$\dot{m}$=0.0141 (kg.s^{-1})	100	0	38.8	26.5
$\dot{m}$=0.06 (kg.s^{-1})	98.6	1.2	40.2	35.5
$\dot{m}$=0.08 (kg.s^{-1})	78.5	17.8	43.3	30.2

The obtained results show that the temperature uniformity in the ISD with ordinary chimney is more uniform by 37.3% compared to the ISD with solar chimney, however the velocity uniformity is better for the ISD with solar chimney. It was also observed that the temperature uniformity decreases with increasing the mass flow rate, where an excellent temperature uniformity has been obtained for the mass flow rate of $\dot{m}$= 0.0141 kg.s^{-1} with 100% of uniform air distribution, followed by $\dot{m}$= 0.06 kg.s^{-1} with 98.6%, and $\dot{m}$= 0.08 kg.s^{-1} with 78.5%. Moreover, using forced convection enhanced the uniformity inside the drying chamber where the temperature uniformity increased by 21.7% for $\dot{m}$= 0.0141 kg.s^{-1} and 20.3% for $\dot{m}$=0.06 kg.s^{-1}, while a negligible enhancement was obtained for the air flow rate of $\dot{m}$=0.08 kg.s^{-1}.

However, concerning velocity uniformity, the results show that the applied modifications (solar chimney / forced convection) did not significantly ameliorate the airflow uniformity where two regions of velocity were observed with varying proportions of uniformity from a SD configuration to other. Moreover, the rate of the first dominated color was almost the same for the five tested designs.

One of the reasons of the non-uniformity observed in the air velocity is the drawback of this drying chamber design, mainly number of drying chamber inlets and outlets. Therefore, the validated CFD model could be used in future separate optimization studies on number and positions of drying chamber inlets and outlets.

As a result, to choose the best design, both of the temperature and velocity uniformities should be checked. The velocity uniformity proportions were almost the same in all the studied designs. Therefore, choosing the best design among the studied configurations depends only on the temperature uniformity. The image processing of temperature contours shows that the mass flow rate of $\dot{m}$=0.0141 kg.s^{-1} ensures the best uniformity, followed by $\dot{m}$=0.06 kg.s^{-1} while the design with negligible preference (+1.4%) was the case of $\dot{m}$=0.0141 kg.s^{-1}. Thus, as the difference is very small between these two designs and as increasing $\dot{m}$ reduces the drying time *(Akbulut & Durmuş, 2010)*, we can consider the design with ordinary chimney and $\dot{m}$=0.06 kg.s^{-1} as optimal operating condition that provides a uniform and best quality of dried products in reduced time.

4. Conclusion

In the current chapter, the uniformity of the drying air inside indirect solar dryer was investigated using a new approach based on image processing and computational fluid dynamics. Moreover, the impact of changing the ordinary chimney by a solar one on the air motion inside the solar dryer and the effect of different mass flow rates on the drying uniformity were investigated.

The main achievements obtained are listed as follows:

- Results from the numerical model established herein demonstrate reasonable agreement with the results obtained from the experimental investigation.
- Replacing the ordinary chimney with a solar chimney improves the drying air temperature by 7 degrees but the temperature uniformity is better by 37.3% for the solar dryer with ordinary chimney.
- The forced convection increased the average temperature by 16 K for $\dot{m}$ = 0.0141 kg.s^{-1}, 11 K for $\dot{m}$ =0.0636 kg.s-1, and 8 K for $\dot{m}$ = 0.0872 kg.s^{-1}.
- The temperature uniformity has been improved by 21.7% for $\dot{m}$= 0.0141 kg.s^{-1} and by 20.3% for $\dot{m}$=0.06 kg.s^{-1}, while a negligible increase was noted for $\dot{m}$=0.08 kg.s^{-1}.
- CFD along with image processing proved the $\dot{m}$=0.06 kg.s^{-1} as the optimal operating condition that enhances the drying uniformity and drying temperature.
- The findings of this study clearly highlighted the potential of the image processing and CFD techniques to select best solar dryer design that improves drying uniformity of agri-food products. This proposed approach would help also laboratories and industrials in the design of new dryers for other similar applications such brick drying.

To sustain the balance between population growth and food supply, food losses during harvesting and marketing should be minimized. The quality and quantity of agricultural produce suffer due to poor processing methods and shortage of storage facilities. Many developing countries suffer considerable losses on the agricultural front.

Solar drying is one such ancient technique of food preservation. Solar dryers of various sizes, capacities and designs are available for drying applications in agricultural industries. Indirect type solar dryer (ITSD) is one of the prominent dryers used to dry food products.

Optimization and parametric studies can be costly and time consuming if carried out by physical experiments. Numerical models however offer a more flexible and less expensive tool to carry out such studies. This thesis has aimed to optimize the geometry of the indirect solar dryer using validated models which accounts for a wide range of the key factors affecting the solar dryer performances. In addition, the numerical models have been coupled with a multi-objective optimization method in order to study the combined effect of design parameters on the main objective functions.

The main conclusions can be summarized in the following points:

- As the solar air heater is the main tool that converts the solar energy into thermal one, A SAH numerical model based on energy balance equations has been established and experimentally validated. The delivered results are in a good agreement with the experimental test results where the mean relative error is 5.745%.
- The optimization of the solar air heater was based on the multi-objective procedure and numerical simulation using MATLAB. The main objective function where the exergetic improvement potential and the determined optimal conditions are: 1.28 for the ration L/W, 0.067m for the air duct height and 49 for number of fins on the absorber. This optimal design improved the energy efficiency and the IP of the SAH by 15.76% and 19.33%, respectively.
- A 2D CFD model have been developed to study the air distribution uniformity inside the drying chamber, and the results from the numerical model established demonstrate reasonable agreement with the results obtained from the experimental investigation.

- The results of the multi- objective optimization of the drying chamber in order to enhance the drying uniformity that the solar dryer design should be selected based on multi-criteria selection.
- Changing the ordinary chimney by a solar chimney improves the drying air temperature by 7 degrees but the temperature uniformity is better by 37.3% for the solar dryer with ordinary chimney.
- The forced convection increased the average temperature by 16 K for $\dot{m}$ = 0.141 kg.s^{-1}, 11 K for $\dot{m}$ =0.0636 kg.s^{-1}, and 8 K for $\dot{m}$ = 0.0872 kg.s^{-1}.
- CFD along with image processing proved the $\dot{m}$=0.06 kg.s^{-1} as the optimal operating condition that enhances the drying uniformity and drying temperature.
- The findings of this study clearly highlighted the potential of the image processing and CFD techniques in improving drying uniformity of agri-food products using solar dryers.

Perspectives:

The current thesis did not reach all the stated goals at the beginning. Because of the lack of means to do some complementary experiments or the time factor. The most important of these goals that we seek to achieve in the future are to use hybrid Pv-t instead of thermal solar air heater, and to improve the indirect solar drying system suing energy storage.

Appendix A Experimental error analysis

Total uncertainty (W_T) in the temperature measurement comes from the thermocouples, connection points and reading, and can be evaluated by the following expression:

$$W_T = \left[W^2_{\text{Thermocuples}} + W^2_{\text{Connection}} + W^2_{\text{Reading}}\right]^{1/2}$$

$$W_T = \left[(0.3)^2 + (0.1)^2 + (0.5)^2\right]^{1/2} = 0.59$$

On the other hand, to measure solar radiation, the total uncertainty (W_{SR}) arises from the pyranometer and its reading and can be predicted as:

$$W_{SR} = \left[W^2_{\text{Pyranometer}} + W^2_{\text{Reading}}\right]^{1/2}$$

$$W_{SR} = \left[(1.2)^2 + (0.2)^2\right]^{1/2} = 1.22$$

To measure the air velocity a total uncertainty (W_{wv}) is sourced from the anemometer, and its reading. where W_{wv} can be estimated by Eq. (B.4):

$$W_{Wv} = \left[W^2_{\text{Anemometer}} + W^2_{\text{Reading}}\right]^{1/2}$$

$$W_{Wv} = \left[(0.03)^2 + (0.2)^2\right]^{1/2} = 0.283$$

The total uncertainty in the measurement of wind speed (W_{ws}) arising from the anemometer and reading are evaluated as:

$$W_{Ws} = \left[W^2_{\text{Anemometer}} + W^2_{\text{Reading}}\right]^{1/2}$$

$$W_{Ws} = \left[(0.9)^2 + (0.2)^2\right]^{1/2} = 0.92$$

Appendix B Coefficients of equations

$$F_1 = \frac{h_{g,amb}}{\rho_g \delta_g C_g}, F_2 = \frac{R_{g,abs}}{\rho_g \delta_g C_g}, F_3 = \frac{h_{g,ga}}{\rho_g \delta_g C_g},$$

$$F_4 = \frac{\alpha_g G}{\rho_g \delta_g C_g}, F_5 = \frac{h_{g,amb}}{\rho_g \delta_g C_g}, F_6 = \frac{R_{g,abs}}{\rho_g \delta_g C_g},$$

$$F_7 = \frac{h_{abs,fluid}}{\rho_{abs}\delta_{abs}C_{abs}}\left[1+\frac{A_{f,fluid}}{A_{abs,fluid}}\eta_f\right]A_{abs,fluid},$$

$$F_8 = \frac{R_{g,abs}}{\rho_{abs}\delta_{abs}C_{abs}}, F_9 = \frac{h_{abs,ga}}{\rho_{abs}\delta_{abs}C_{abs}},$$

$$F_{10} = \frac{R_{ins,abs}}{\rho_{abs}\delta_{abs}C_{abs}}, F_{11} = \frac{\alpha_{abs}\tau_g G}{\rho_{abs}\delta_{abs}C_{abs}},$$

$$F_{12} = \frac{h_{abs,fluid}}{\rho_{fluid}\delta_{fluid}C_{fluid}}\left[1+\frac{A_{f,fluid}}{A_{abs,fluid}}\eta_f\right]A_{abs,fluid},$$

$$F_{13} = \frac{h_{ins,fluid}}{\rho_{fluid}\delta_{fluid}C_{fluid}}, F_{14} = \frac{\dot{m}C_{fluid}}{\rho_{fluid}\delta_{fluid}C_{fluid}},$$

$$F_{15} = \frac{R_{abs,ins}}{\rho_{ins}\delta_{ins}C_{ins}}, F_{16} = \frac{h_{ins,fluid}}{\rho_{ins}\delta_{ins}C_{ins}}, F_{17} = \frac{U_{ins}}{\rho_{ins}\delta_{ins}C_{ins}}.$$

$$Y_1 = \left(\frac{1}{\Delta t} + F_1 + F_2 + F_3\right)$$

$$Y_2 = \left(\frac{1}{\Delta t} + F_5 + F_6\right)$$

$$Y_3 = \left(\frac{1}{\Delta t} + F_7 + F_8 + F_9 + F_{10}\right)$$

$$Y_4 = \left(\frac{1}{\Delta t} + F_{12} + F_{13} + F_{14}\right)$$

$$Y_5 = \left(\frac{1}{\Delta t} + F_{15} + F_{16} + F_{17}\right)$$

Appendix C Image image processing of temperature distribution inside the drying chamber

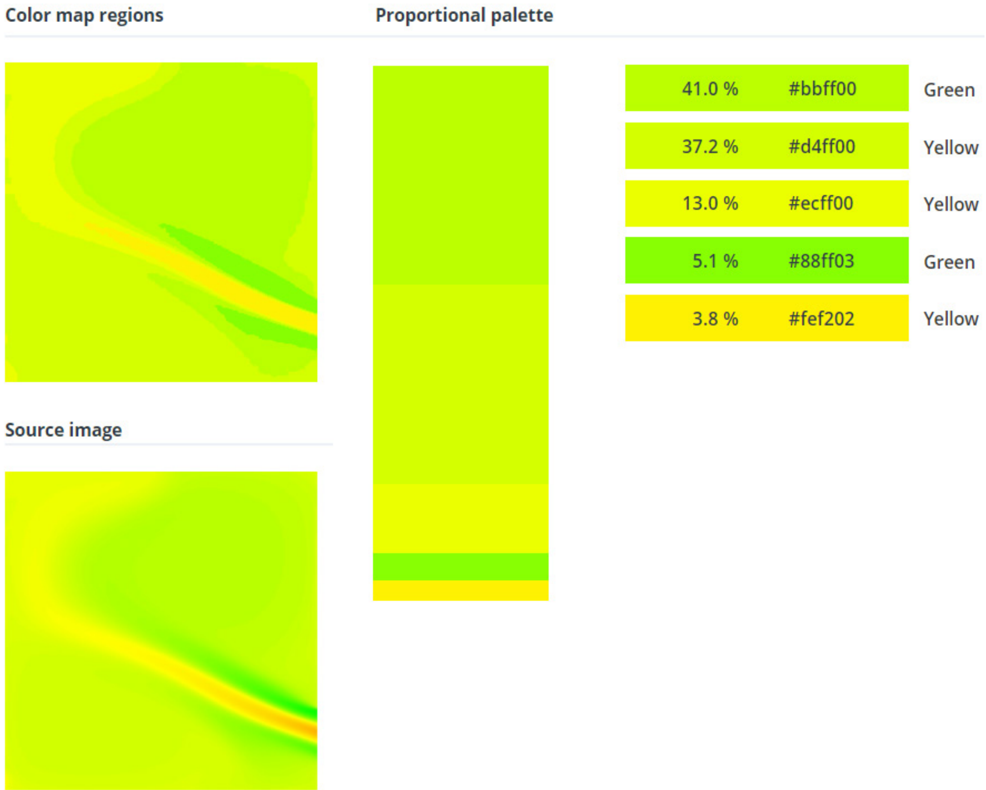

Fig. C-1 Sample of extracted color palette of temperature distribution for natural convection with solar chimney.

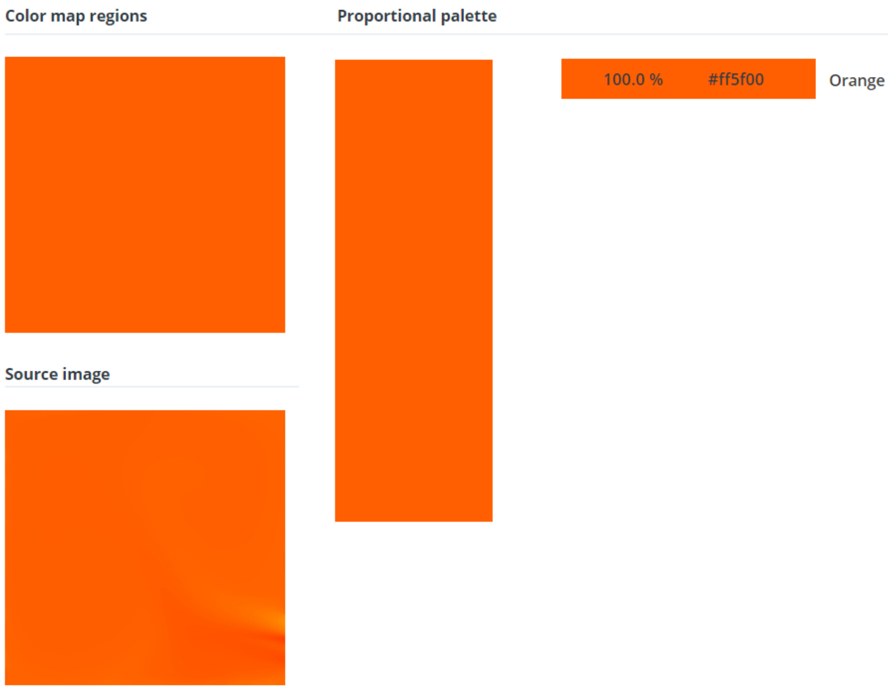

Fig. C-2 Sample of extracted color palette of temperature distribution for $\dot{m}$=0.0141 kg.s^{-1}.

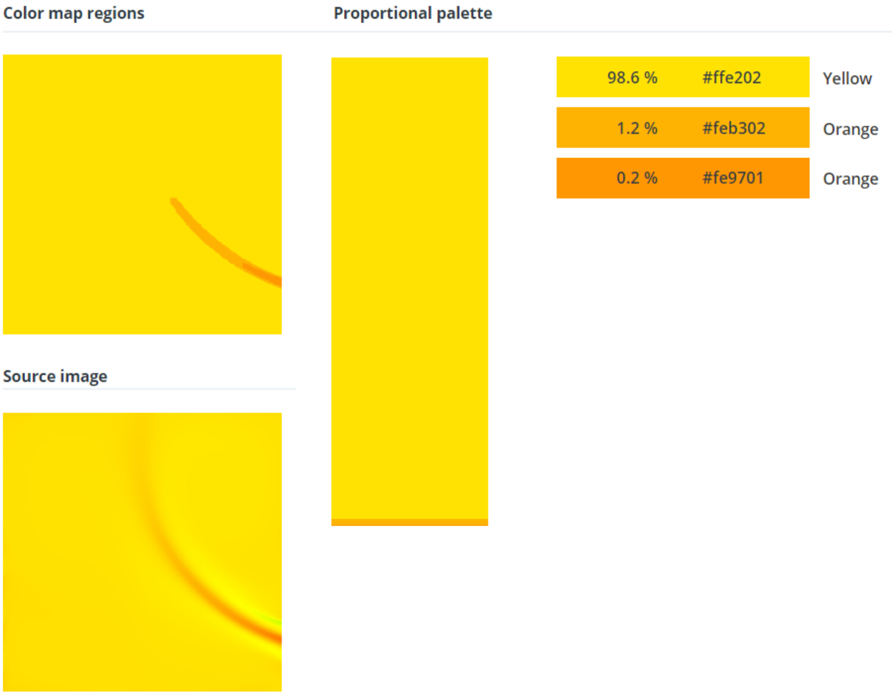

Fig. C-3 Sample of extracted color palette of temperature distribution for $\dot{m}=0.06\ kg.s^{-1}$.

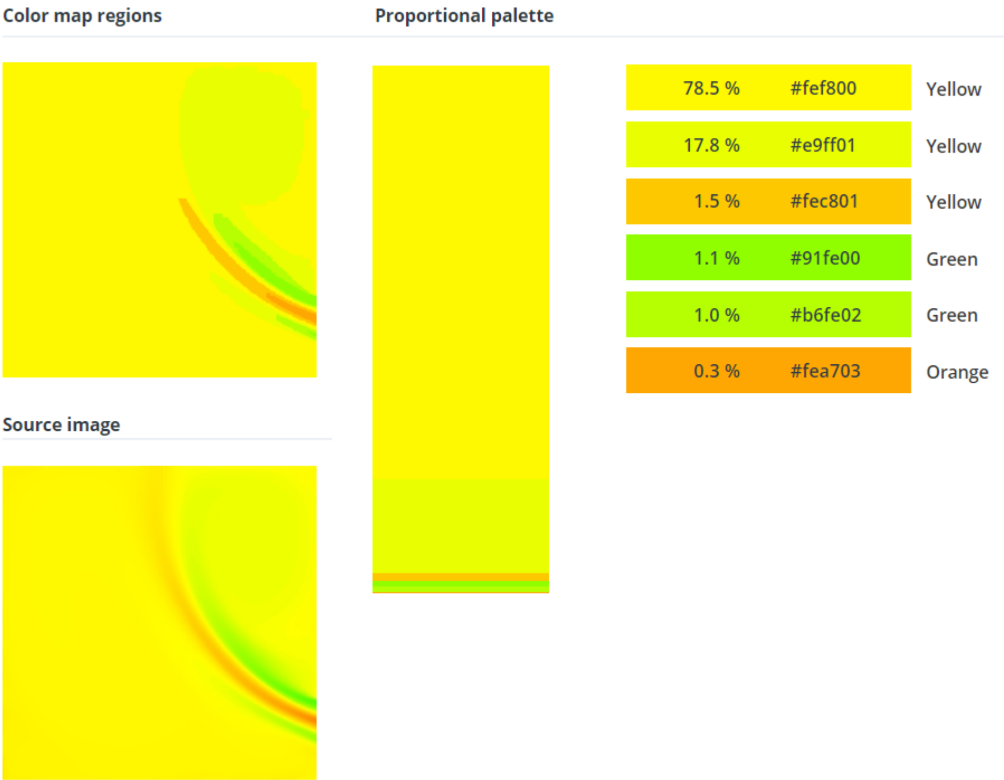

Fig. C-4 Sample of extracted color palette of temperature distribution for $\dot{m}=0.08\ kg.s^{-1}$.

Appendix D Image image processing of velocity distribution inside the drying chamber

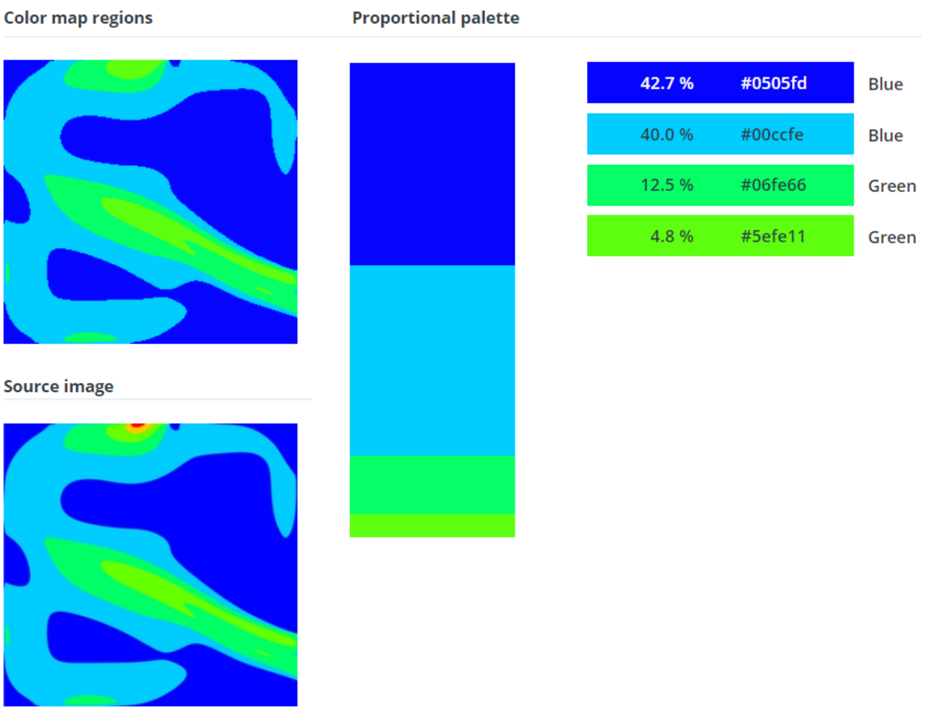

Fig. D- 5 Sample of extracted color palette of velocity distribution for natural convection with ordinary chimney.

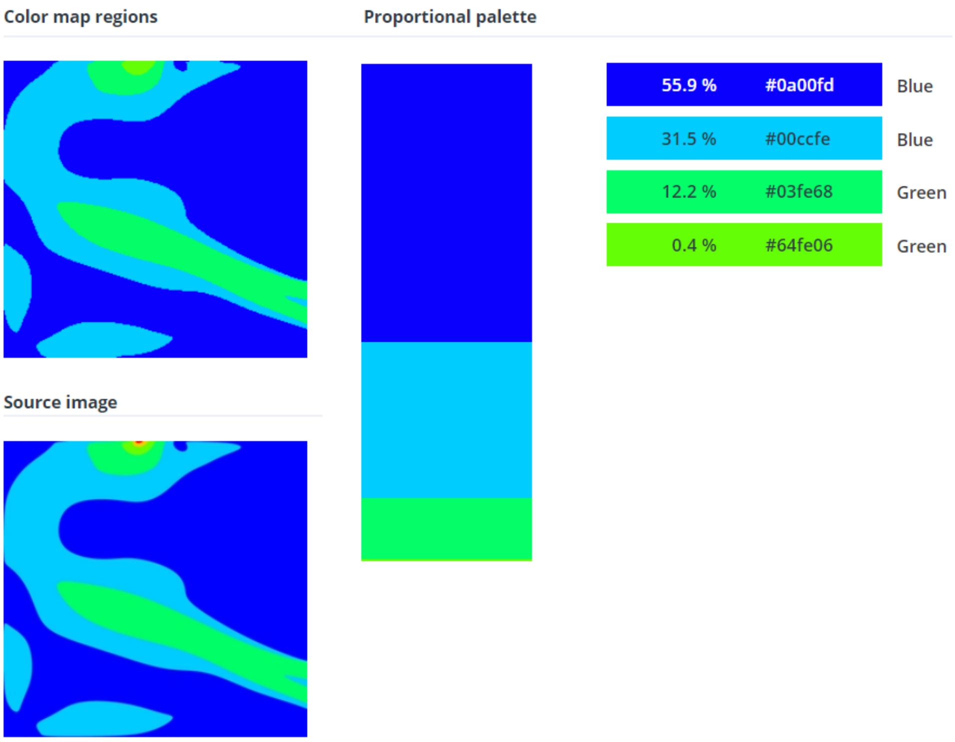

Fig. D- 6 Sample of extracted color palette of velocity distribution for natural convection with solar chimney.

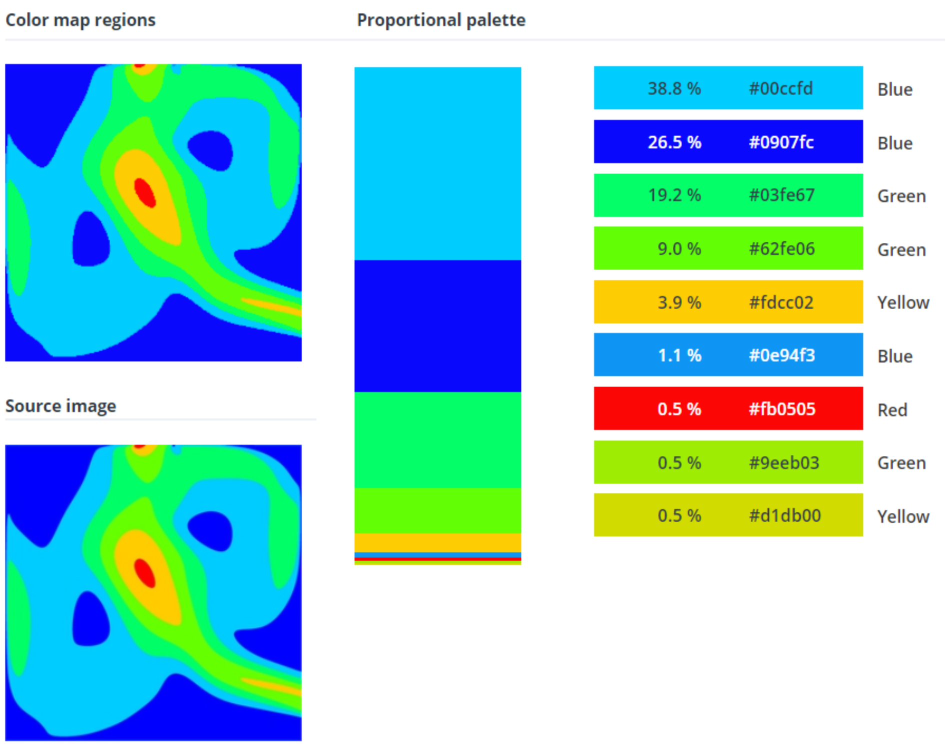

Fig. D-**7** Sample of extracted color palette of velocity distribution for $\dot{m}$=0.0141 $kg.s^{-1}$.

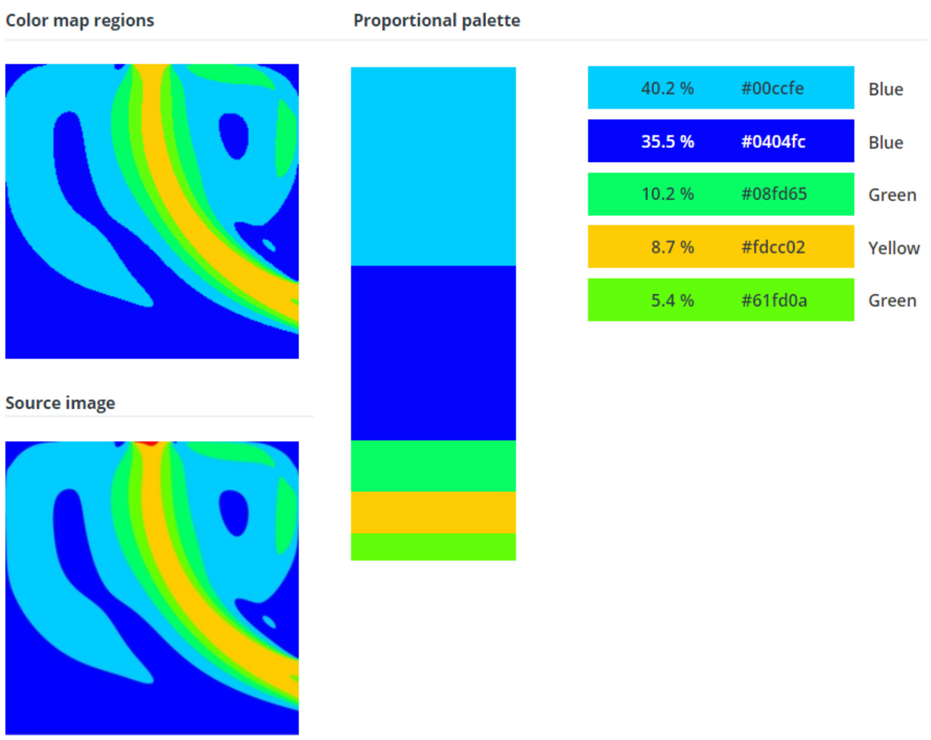

Fig. D- 8 Sample of extracted color palette of velocity distribution for $\dot{m}$=0.06 $kg.s^{-1}$.

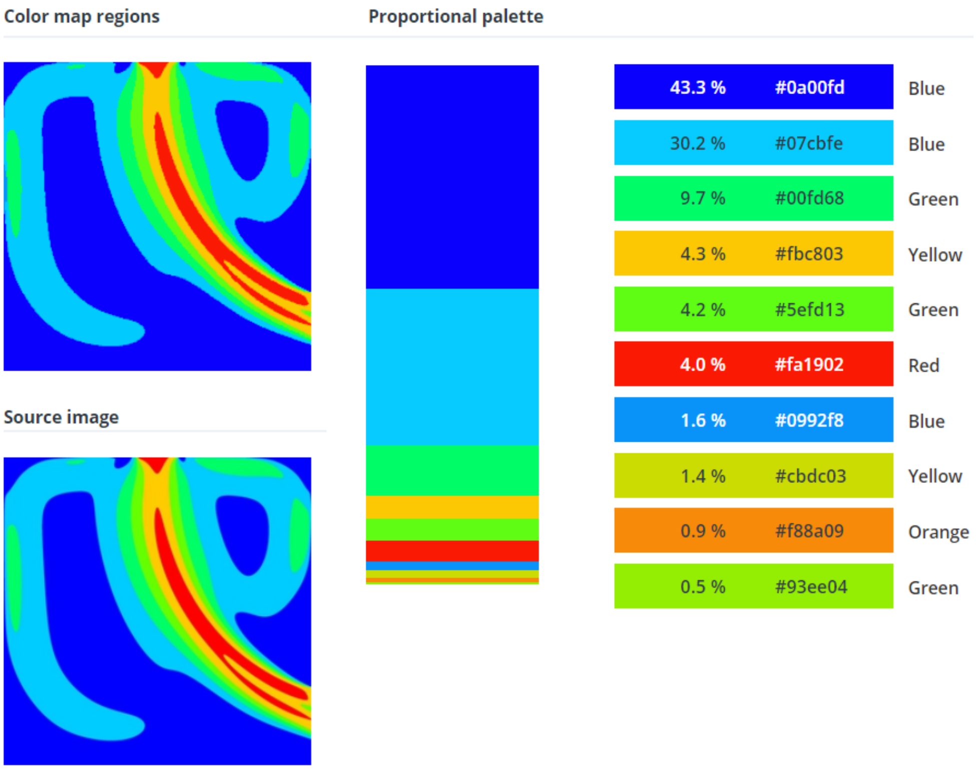

Fig. D- 9 Sample of extracted color palette of velocity distribution for $\dot{m}$=0.08 kg.s^{-1}.

REFERENCES

Abhay, L., Chandramohan, V. P., & Raju, V. R. K. (2018). Numerical analysis on solar air collector provided with artificial square shaped roughness for indirect type solar dryer. *Journal of Cleaner Production, 190*, 353-367. doi:10.1016/j.jclepro.2018.04.130

Akbulut, A., & Durmuş, A. (2010). Energy and exergy analyses of thin layer drying of mulberry in a forced solar dryer. *Energy, 35*(4), 1754-1763. doi:10.1016/j.energy.2009.12.028

Akpinar, E. K. (2010). Drying of mint leaves in a solar dryer and under open sun: Modelling, performance analyses. *Energy Conversion and Management, 51*(12), 2407-2418. doi:10.1016/j.enconman.2010.05.005

Akpinar, E. K., & Koçyiğit, F. (2010). Energy and exergy analysis of a new flat-plate solar air heater having different obstacles on absorber plates. *Applied Energy, 87*(11), 3438-3450. doi:10.1016/j.apenergy.2010.05.017

Al-Kayiem, H. H., Hussein, A. K., & Peow, T. S. (2013). Investigations of Natural Convective Heat Transfer in Rectangular Thermal Passages. *International Journal of Mechanical and Mechatronics Engineering, 75*(3), 452-457. doi:doi.org/10.5281/zenodo.1335854

Alimohammadi, Z., Samimi Akhijahani, H., & Salami, P. (2020). Thermal analysis of a solar dryer equipped with PTSC and PCM using experimental and numerical methods. *Solar Energy, 201*, 157-177. doi:https://doi.org/10.1016/j.solener.2020.02.079

Amanlou, Y., & Zomorodian, A. (2010). Applying CFD for designing a new fruit cabinet dryer. *Journal of Food Engineering, 101*(1), 8-15. doi:10.1016/j.jfoodeng.2010.06.001

Anderson, J.-O., & Westerlund, L. (2014). Improved energy efficiency in sawmill drying system. *Applied Energy, 113*, 891-901. doi:https://doi.org/10.1016/j.apenergy.2013.08.041

Arias Bustos, C., & Moors, E. H. M. (2018). Reducing post-harvest food losses through innovative collaboration: Insights from the Colombian and Mexican avocado supply chains. *Journal of Cleaner Production, 199*, 1020-1034. doi:10.1016/j.jclepro.2018.06.187

Arslan, E., & Aktaş, M. (2020). 4E analysis of infrared-convective dryer powered solar photovoltaic thermal collector. *Solar Energy, 208*, 46-57. doi:10.1016/j.solener.2020.07.071

Arunkumar, H. S., Vasudeva Karanth, K., & Kumar, S. (2020). Review on the design modifications of a solar air heater for improvement in the thermal performance. *Sustainable Energy Technologies and Assessments, 39*, 100685. doi:10.1016/j.seta.2020.100685

Atalay, H. (2019). Performance analysis of a solar dryer integrated with the packed bed thermal energy storage (TES) system. *Energy, 172*, 1037-1052. doi:10.1016/j.energy.2019.02.023

Babu, A. K., Kumaresan, G., Antony Aroul Raj, V., & Velraj, R. (2019). CFD studies on different configurations of drying chamber for thin-layer drying of leaves. *Energy Sources, Part A: Recovery, Utilization, and Environmental Effects*, 1-13. doi:10.1080/15567036.2019.1607935

BADACHE, M. (2013). *Étude numérique et expérimentale du transfert de chaleur dans un capteur solaire à perforations doté d'un collecteur transparent et opaque.* (doctor). École de technologie supérieure université du québec,

Bekele, A., Mishra, M., & Dutta, S. (2013). Heat transfer augmentation in solar air heater using delta-shaped obstacles mounted on the absorber plate. *International Journal of Sustainable Energy, 32*(1), 53-69. doi:10.1080/14786451.2011.598637

Benhamza, A., Boubekri, A., Atia, A., El Ferouali, H., Hadibi, T., Arıcı, M., & Abdenouri, N. (2021). Multi-objective design optimization of solar air heater for food drying based on energy, exergy and improvement potential. *Renewable Energy, 169*, 1190-1209. doi:10.1016/j.renene.2021.01.086

Benhamza, A., Boubekri, A., Atia, A., Halimi, S., Mouissi, F. M., & Mennouche, D. (2018). Optimized parameters of an air solar collector for drying applications using the experimental design method (DOE).

Benhamza, A., & Settou, B. (2016). *SIMULATION NUMERIQUE D'UN CAPTEUR SOLAIRE PLAN UTILISANT DES MATERIAUX A CHANGEMENT DE PHASE.* (MASTER ACADEMIQUE master thesis). Université Kasdi merbah Ouargla,

Bennett, C. O., & Myers, J. E. (1982). *Momentum, heat, and mass transfer* (Vol. 370): McGraw-Hill New York.

Boubekri, A., Benmoussa, H., Courtois, F., & Bonazzi, C. (2010). Softening of Overdried 'Deglet Nour' Dates to Obtain High-Standard Fruits: Impact of Rehydration and Drying Processes on Quality Criteria. *Drying Technology, 28*(2), 222-231. doi:10.1080/07373930903526764

Brandl, D., Mach, T., Kaltenecker, P., Sterrer, R., Neururer, C., Treberspurg, M., & Hochenauer, C. (2015). CFD assessment of a solar honeycomb (SHC) façade element with integrated PV cells. *Solar Energy, 118*, 155-174. doi:https://doi.org/10.1016/j.solener.2015.03.053

Cadafalch, J. (2009). A detailed numerical model for flat-plate solar thermal devices. *Solar Energy, 83*(12), 2157-2164. doi:10.1016/j.solener.2009.08.013

CEREFE. (2020). *Transition Energétique en Algérie: Leçons, Etat des Lieux et Perspectives pour un Développement Accéléré des Energies Renouvelables*. Retrieved from

Chaatouf, D., Salhi, M., Raillani, B., Dihmani, N., Amraqui, S., Moussaoui, M. A., & Mezrhab, A. (2021). *Trays Effect on the Dynamic and Thermal Behavior of an Indirect Solar Dryer Using CFD Method*, Singapore.

Chegere, M. J. (2018). Post-harvest losses reduction by small-scale maize farmers: The role of handling practices. *Food Policy, 77*, 103-115. doi:10.1016/j.foodpol.2018.05.001

Chen, H.-H., Huang, T.-C., Tsai, C.-H., & Mujumdar, A. S. (2008). Development and Performance Analysis of a New Solar Energy-Assisted Photocatalytic Dryer. *Drying Technology, 26*(4), 503-507. doi:10.1080/07373930801929557

Chouicha, S., Boubekri, A., Mennouche, D., & Berrbeuh, M. H. (2013). Solar Drying of Sliced Potatoes. An Experimental Investigation. *36*, 1276-1285. doi:10.1016/j.egypro.2013.07.144

Darabi, H., Zomorodian, A., Akbari, M. H., & Lorestani, A. N. (2015). Design a cabinet dryer with two geometric configurations using CFD. *Journal of Food Science and Technology, 52*(1), 359-366. doi:10.1007/s13197-013-0983-1

Demissie, P., Hayelom, M., Kassaye, A., Hailesilassie, A., Gebrehiwot, M., & Vanierschot, M. (2019). Design, development and CFD modeling of indirect solar food dryer. *Energy Procedia, 158*, 1128-1134. doi:10.1016/j.egypro.2019.01.278

Dinçer, İ., & Zamfirescu, C. (2016). *Drying phenomena: theory and applications*: John Wiley & Sons.

Duffie, J. A., & Beckman, W. A. (2013). *Solar engineering of thermal processes*: John Wiley & Sons.

El Hage, H., Herez, A., Ramadan, M., Bazzi, H., & Khaled, M. (2018). An investigation on solar drying: A review with economic and environmental assessment. *Energy, 157*, 815-829. doi:https://doi.org/10.1016/j.energy.2018.05.197

Evangelisti, L., De Lieto Vollaro, R., & Asdrubali, F. (2019). Latest advances on solar thermal collectors: A comprehensive review. *Renewable and Sustainable Energy Reviews, 114*, 109318. doi:10.1016/j.rser.2019.109318

FAO. (2013). *Food wastage footprint: Impacts on natural resources*: FAO.

Ferreira, S. L., Bruns, R. E., Ferreira, H. S., Matos, G. D., David, J. M., Brandao, G. C., . . . dos Santos, W. N. (2007). Box-Behnken design: an alternative for the optimization of analytical methods. *Anal Chim Acta, 597*(2), 179-186. doi:10.1016/j.aca.2007.07.011

Flourentzou, F., Van der Maas, J., & Roulet, C. A. (1998). Natural ventilation for passive cooling: measurement of discharge coefficients. *Energy and Buildings, 27*(3), 283-292. doi:https://doi.org/10.1016/S0378-7788(97)00043-1

Food, & Organization, A. (2010). The state of food insecurity in the world: Addressing food insecurity in protracted crises. In: FAO Rome.

Fudholi, A., & Sopian, K. (2019). A review of solar air flat plate collector for drying application. *Renewable and Sustainable Energy Reviews, 102*, 333-345. doi:10.1016/j.rser.2018.12.032

Fudholi, A., Sopian, K., Othman, M. Y., Ruslan, M. H., & Bakhtyar, B. (2013). Energy analysis and improvement potential of finned double-pass solar collector. *Energy Conversion and Management, 75*, 234-240. doi:10.1016/j.enconman.2013.06.021

Gerald, C. F. (2004). *Applied numerical analysis*: Pearson Education India.

Ghaffari, A., & Mehdipour, R. (2015). Modeling and Improving the Performance of Cabinet Solar Dryer Using Computational Fluid Dynamics. *International Journal of Food Engineering, 11*(2), 157-172. doi:10.1515/ijfe-2014-0266

Giri, S. K., & Prasad, S. (2007). Optimization of Microwave-Vacuum Drying of Button Mushrooms Using Response-Surface Methodology. *Drying Technology, 25*(5), 901-911. doi:10.1080/07373930701370407

Güler, H. Ö., Sözen, A., Tuncer, A. D., Afshari, F., Khanlari, A., Şirin, C., & Gungor, A. (2020). Experimental and CFD survey of indirect solar dryer modified with low-cost iron mesh. *Solar Energy, 197*, 371-384. doi:10.1016/j.solener.2020.01.021

Gupta, M. K., & Kaushik, S. C. (2008). Exergetic performance evaluation and parametric studies of solar air heater. *Energy, 33*(11), 1691-1702. doi:10.1016/j.energy.2008.05.010

Hadibi, T., Boubekri, A., Mennouche, D., Benhamza, A., & Abdenouri, N. (2021). 3E analysis and mathematical modelling of garlic drying process in a hybrid solar-electric dryer. *Renewable Energy, 170*, 1052-1069. doi:10.1016/j.renene.2021.02.029

Hadibi, T., Boubekri, A., Mennouche, D., Benhamza, A., & Kumar, A. (2021). Economic analysis and drying kinetics of a geothermal-assisted solar dryer for tomato paste drying. *J Sci Food Agric*. doi:10.1002/jsfa.11326

Heydari, A., & Mesgarpour, M. (2018). Experimental analysis and numerical modeling of solar air heater with helical flow path. *Solar Energy, 162*, 278-288. doi:10.1016/j.solener.2018.01.030

Hodges, R. J., Buzby, J. C., & Bennett, B. (2011). Postharvest losses and waste in developed and less developed countries: opportunities to improve resource use. *The Journal of Agricultural Science, 149*(S1), 37-45. doi:10.1017/S0021859610000936

Hollands, K. G. T., Unny, T. E., Raithby, G. D., & Konicek, L. (1976). Free Convective Heat Transfer Across Inclined Air Layers. *Journal of Heat Transfer, 98*(2), 189-193. doi:10.1115/1.3450517

Hu, J., & Zhang, G. (2019). Performance improvement of solar air collector based on airflow reorganization: A review. *Applied Thermal Engineering, 155*, 592-611. doi:10.1016/j.applthermaleng.2019.04.021

Iranmanesh, M., Samimi Akhijahani, H., & Barghi Jahromi, M. S. (2020). CFD modeling and evaluation the performance of a solar cabinet dryer equipped with evacuated tube solar collector and thermal storage system. *Renewable Energy, 145*, 1192-1213. doi:10.1016/j.renene.2019.06.038

Jain, A., Sharma, M., Kumar, A., Sharma, A., & Palamanit, A. (2019). Computational fluid dynamics simulation and energy analysis of domestic direct-type multi-shelf solar dryer. *Journal of Thermal Analysis and Calorimetry, 136*(1), 173-184. doi:10.1007/s10973-018-7973-5

Kabeel, A. E., Hamed, M. H., Omara, Z. M., & Kandeal, A. W. (2017). Solar air heaters: Design configurations, improvement methods and applications – A detailed review. *Renewable and Sustainable Energy Reviews, 70*, 1189-1206. doi:10.1016/j.rser.2016.12.021

Kabeel, A. E., Hamed, M. H., Omara, Z. M., & Kandeal, A. W. (2018). Influence of fin height on the performance of a glazed and bladed entrance single-pass solar air heater. *Solar Energy, 162*, 410-419. doi:10.1016/j.solener.2018.01.037

Kalaiarasi, G., Velraj, R., & Swami, M. V. (2016). Experimental energy and exergy analysis of a flat plate solar air heater with a new design of integrated sensible heat storage. *Energy, 111*, 609-619. doi:10.1016/j.energy.2016.05.110

Kalaiarasi, G., Velraj, R., Vanjeswaran, M. N., & Ganesh Pandian, N. (2020). Experimental analysis and comparison of flat plate solar air heater with and without integrated sensible heat storage. *Renewable Energy, 150*, 255-265. doi:10.1016/j.renene.2019.12.116

Kalogirou, S. A. (2004). Solar thermal collectors and applications. *Progress in Energy and Combustion Science, 30*(3), 231-295. doi:10.1016/j.pecs.2004.02.001

Kalogirou, S. A., Karellas, S., Braimakis, K., Stanciu, C., & Badescu, V. (2016). Exergy analysis of solar thermal collectors and processes. *Progress in Energy and Combustion Science, 56*, 106-137. doi:https://doi.org/10.1016/j.pecs.2016.05.002

Kamarulzaman, A., Hasanuzzaman, M., & Rahim, N. A. (2021). Global advancement of solar drying technologies and its future prospects: A review. *Solar Energy, 221*, 559-582. doi:10.1016/j.solener.2021.04.056

Karim, M., & Hawlader, M. (2006). Performance investigation of flat plate, v-corrugated and finned air collectors. *Energy, 31*(4), 452-470. doi:10.1016/j.energy.2005.03.007

Karmare, S. V., & Tikekar, A. N. (2009). Experimental investigation of optimum thermohydraulic performance of solar air heaters with metal rib grits roughness. *Solar Energy, 83*(1), 6-13. doi:https://doi.org/10.1016/j.solener.2008.05.017

Khaldi, S., Korti, A. I. N., & Abboudi, S. (2017a). Improving the Airflow Distribution Within an Indirect Solar Dryer by Modifications Based on Computational Fluid Dynamics. *International Journal of Air-Conditioning and Refrigeration, 25*(03). doi:10.1142/s2010132517500225

Khaldi, S., Korti, A. N., & Abboudi, S. (2017b). Applying CFD for Studying the Dynamic and Thermal Behavior of Solar Chimney Drying System with Reversed Absorber. *International Journal of Food Engineering, 13*(11). doi:10.1515/ijfe-2017-0081

Khanlari, A., Sözen, A., Afshari, F., Şirin, C., Tuncer, A. D., & Gungor, A. (2020). Drying municipal sewage sludge with v-groove triple-pass and quadruple-pass solar air heaters along with testing of a solar absorber drying chamber. *Science of The Total Environment, 709*, 136198. doi:https://doi.org/10.1016/j.scitotenv.2019.136198

Kulkarni, K., Afzal, A., & Kim, K.-Y. (2015). Multi-objective optimization of solar air heater with obstacles on absorber plate. *Solar Energy, 114*, 364-377. doi:10.1016/j.solener.2015.02.008

Kumar, A., & Layek, A. (2019). Thermo-hydraulic performance of roughened solar air heater by design of experiment and meta-heuristic approach. *Thermal Science and Engineering Progress, 10*, 92-102. doi:10.1016/j.tsep.2019.01.011

Kumar, M., Sansaniwal, S. K., & Khatak, P. (2016). Progress in solar dryers for drying various commodities. *Renewable and Sustainable Energy Reviews, 55*, 346-360. doi:10.1016/j.rser.2015.10.158

Kumar, R., Goel, V., Singh, P., Saxena, A., Kashyap, A. S., & Rai, A. (2019). Performance evaluation and optimization of solar assisted air heater with discrete multiple arc shaped ribs. *Journal of Energy Storage, 26*, 100978. doi:10.1016/j.est.2019.100978

Lamidi, R. O., Jiang, L., Pathare, P. B., Wang, Y. D., & Roskilly, A. P. (2019). Recent advances in sustainable drying of agricultural produce: A review. *Applied Energy, 233-234*, 367-385. doi:https://doi.org/10.1016/j.apenergy.2018.10.044

Lingayat, A. B., Chandramohan, V. P., Raju, V. R. K., & Meda, V. (2020). A review on indirect type solar dryers for agricultural crops – Dryer setup, its performance, energy storage and important highlights. *Applied Energy, 258*, 114005. doi:10.1016/j.apenergy.2019.114005

Lokeswaran, S., & Eswaramoorthy, M. (2013). An Experimental Analysis of a Solar Greenhouse Drier: Computational Fluid Dynamics (CFD) Validation. *Energy Sources, Part A: Recovery, Utilization, and Environmental Effects, 35*(21), 2062-2071. doi:10.1080/15567036.2010.532195

Lundqvist, J., de Fraiture, C., & Molden, D. (2008). *Saving Water: From Field to Fork: Curbing Losses and Wastage in the Food Chain*. Retrieved from http://hdl.handle.net/10535/5088

Majdi, H., Esfahani, J. A., & Mohebbi, M. (2019). Optimization of convective drying by response surface methodology. *Computers and Electronics in Agriculture, 156*, 574-584. doi:10.1016/j.compag.2018.12.021

Mäkelä, M. (2017). Experimental design and response surface methodology in energy applications: A tutorial review. *Energy Conversion and Management, 151*, 630-640. doi:10.1016/j.enconman.2017.09.021

McAdams, W. H. (1954). *Heat transmission*. Retrieved from

Mecheri, A., Kouici, A., Boubekri, A., & Benhamza, A. (2019). *Etude d'amélioration de l'homogénéité du champ thermique dans un séchoir solaire en utilisant la méthode des plans d'expériences.* Ouargla university,

Mennouche, D., Boubekri, A., Chouicha, S., Bouchekima, B., & Bouguettaia, H. (2017). Solar drying process to obtain high standard "deglet-nour" date fruit. *40*(5), e12546. doi:https://doi.org/10.1111/jfpe.12546

Milani Shirvan, K., Mamourian, M., Mirzakhanlari, S., Ellahi, R., & Vafai, K. (2017). Numerical investigation and sensitivity analysis of effective parameters on combined heat transfer performance in a porous solar cavity receiver by response surface methodology. *105*, 811-825. doi:10.1016/j.ijheatmasstransfer.2016.10.008

Mohana, Y., Mohanapriya, R., Anukiruthika, T., Yoha, K. S., Moses, J. A., & Anandharamakrishnan, C. (2020). Solar dryers for food applications: Concepts, designs, and recent advances. *Solar Energy, 208*, 321-344. doi:10.1016/j.solener.2020.07.098

Mugi, V. R., & Chandramohan, V. P. (2020). Energy end exergy analysis of forced and natural convection indirect solar dryers: Estimation of exergy inflow, outflow, losses, exergy efficiencies and sustainability indicators from drying experiments. *Journal of Cleaner Production*, 124421. doi:10.1016/j.jclepro.2020.124421

Munesue, Y., Masui, T., & Fushima, T. (2015). The effects of reducing food losses and food waste on global food insecurity, natural resources, and greenhouse gas emissions. *Environmental Economics and Policy Studies, 17*(1), 43-77. doi:10.1007/s10018-014-0083-0

Myers, R. H., Montgomery, D. C., & Anderson-Cook, C. M. (2016). *Response surface methodology: process and product optimization using designed experiments*: John Wiley & Sons.

Nadir, N., Bouguettaia, H., Boughali, S., & Bechki, D. (2019). Use of a new agricultural product as thermal insulation for solar collector. *Renewable Energy, 134*, 569-578. doi:10.1016/j.renene.2018.11.054

Naphon, P. (2005). On the performance and entropy generation of the double-pass solar air heater with longitudinal fins. *Renewable Energy, 30*(9), 1345-1357. doi:10.1016/j.renene.2004.10.014

Nazri, N. S., Fudholi, A., Mustafa, W., Yen, C. H., Mohammad, M., Ruslan, M. H., & Sopian, K. (2019). Exergy and improvement potential of hybrid photovoltaic thermal/thermoelectric (PVT/TE) air collector. *Renewable and Sustainable Energy Reviews, 111*, 132-144. doi:10.1016/j.rser.2019.03.024

Pérez-Espinosa, R., García-Valladares, O., & Pilatowsky, I. (2020). Numerical modeling and experimental validation of Back-Pass rectangular ducts solar air heaters. *Applied Thermal Engineering*, 115018. doi:10.1016/j.applthermaleng.2020.115018

Potgieter, M. S. W., Bester, C. R., & Bhamjee, M. (2020). Experimental and CFD investigation of a hybrid solar air heater. *Solar Energy, 195*, 413-428. doi:10.1016/j.solener.2019.11.058

Poveda, J. (2020). Marchantia polymorpha subsp. ruderalis (Bischl. & Boissel.-Dub.)-arbuscular mycorrhizal fungi interaction: beneficial or harmful? *Symbiosis*. doi:10.1007/s13199-020-00708-6

Qader, B. S., Supeni, E. E., Ariffin, M. K. A., & Talib, A. R. A. (2019). RSM approach for modeling and optimization of designing parameters for inclined fins of solar air heater. *Renewable Energy, 136*, 48-68. doi:10.1016/j.renene.2018.12.099

Raam Dheep, G., & Sreekumar, A. (2020). Experimental Studies on Energy and Exergy Analysis of a Single-Pass Parallel Flow Solar Air Heater. *Journal of Solar Energy Engineering, 142*(1). doi:10.1115/1.4044127

Ranjbaran, M., Emadi, B., & Zare, D. (2014). CFD Simulation of Deep-Bed Paddy Drying Process and Performance. *Drying Technology, 32*(8), 919-934. doi:10.1080/07373937.2013.875561

Sandali, M., Boubekri, A., Benhamza, A., Settou, B., Halassa, D., & Mennouche, D. (2017). A simulation study of a solar collector using phase change materials for air heating application needs. *AIP Conference Proceedings, 1814*(1), 020010. doi:https://doi.org/10.1063/1.4976229

Sandali, M., Boubekri, A., & Mennouche, D. (2019). Improvement of the Thermal Performance of Solar Drying Systems Using Different Techniques: A Review. *Journal of Solar Energy Engineering, 141*(5). doi:10.1115/1.4043613

Sandali, M., Boubekri, A., Mennouche, D., & Benhamza, A. (2018). *Etude du comportement thermique d'un séchoir solaire direct influencé par l'intégration d'un milieu poreux non consolide.* Paper presented at the 6 ème séminaire maghrébin sur les sciences et les technologies de séchage (SMSTS 2018).

Sandali, M., Boubekri, A., Mennouche, D., & Gherraf, N. (2019). Improvement of a direct solar dryer performance using a geothermal water heat exchanger as supplementary energetic supply. An experimental investigation and simulation study. *Renewable Energy, 135*, 186-196. doi:10.1016/j.renene.2018.11.086

Sanghi, A., Ambrose, R. P. K., & Maier, D. (2017). CFD simulation of corn drying in a natural convection solar dryer. *Drying Technology, 36*(7), 859-870. doi:10.1080/07373937.2017.1359622

Saravanakumar, P. T., Somasundaram, D., & Matheswaran, M. M. (2020). Exergetic investigation and optimization of arc shaped rib roughened solar air heater integrated with fins and baffles. *Applied Thermal Engineering, 175*, 115316. doi:10.1016/j.applthermaleng.2020.115316

Saxena, A., Varun, & El-Sebaii, A. A. (2015). A thermodynamic review of solar air heaters. *Renewable and Sustainable Energy Reviews, 43*, 863-890. doi:10.1016/j.rser.2014.11.059

Settou, B., Settou, N., Gouareh, A., Negrou, B., Mokhtara, C., & Messaoudi, D. (2021). A high-resolution geographic information system-analytical hierarchy process-based method for solar PV power plant site selection: a case study Algeria. *Clean Technologies and Environmental Policy, 23*(1), 219-234. doi:10.1007/s10098-020-01971-3

Şevik, S. (2013). Design, experimental investigation and analysis of a solar drying system. *Energy Conversion and Management, 68*, 227-234. doi:https://doi.org/10.1016/j.enconman.2013.01.013

Sharma, A., Chen, C. R., & Vu Lan, N. (2009). Solar-energy drying systems: A review. *Renewable and Sustainable Energy Reviews, 13*(6-7), 1185-1210. doi:10.1016/j.rser.2008.08.015

Singh Chauhan, P., Kumar, A., & Tekasakul, P. (2015). Applications of software in solar drying systems: A review. *Renewable and Sustainable Energy Reviews, 51*, 1326-1337. doi:10.1016/j.rser.2015.07.025

Singh, P., & Gaur, M. K. (2020). Review on development, recent advancement and applications of various types of solar dryers. *Energy Sources, Part A: Recovery, Utilization, and Environmental Effects*, 1-21. doi:10.1080/15567036.2020.1806951

Singh, S., & Dhiman, P. (2014). Thermal and thermohydraulic performance evaluation of a novel type double pass packed bed solar air heater under external recycle using an analytical and RSM (response surface methodology) combined approach. *Energy, 72*, 344-359. doi:10.1016/j.energy.2014.05.044

Sivakandhan, C., Arjunan, T. V., & Matheswaran, M. M. (2020). Thermohydraulic performance enhancement of a new hybrid duct solar air heater with inclined rib roughness. *Renewable Energy, 147*, 2345-2357. doi:10.1016/j.renene.2019.10.007

Sultan, U., Zhang, Y., Farooq, M., Imran, M., Akhtar Khan, A., Zhuge, W., . . . Ali, Q. (2021). Qualitative assessment and global mapping of supercritical CO2 power cycle technology. *Sustainable Energy Technologies and Assessments, 43*, 100978. doi:10.1016/j.seta.2020.100978

Sumit Tiwaria, S. A., G.N. Tiwaric. ((2018)). PVT air collector integrated greenhouse dryers. *Renewable and Sustainable Energy, 90*, 142–159. doi:10.1016/j.rser.2018.03.043

Swinbank, W. C. (1963). Long-wave radiation from clear skies. *Quarterly Journal of the Royal Meteorological Society, 89*(381), 339-348. doi:10.1002/qj.49708938105

Tajdaran, S., Kendrick, C., Hopkins, E., & Bonatesta, F. (2020). Geometrical optimisation of Transpired Solar Collectors using design of experiments and computational fluid dynamics. *Solar Energy, 197*, 527-537. doi:10.1016/j.solener.2020.01.018

Tegenaw, P. D., Gebrehiwot, M. G., & Vanierschot, M. (2019). On the comparison between computational fluid dynamics (CFD) and lumped capacitance modeling for the simulation of transient heat transfer in solar dryers. *Solar Energy, 184*, 417-425. doi:10.1016/j.solener.2019.04.024

Tuncer, A. D., Khanlari, A., Sözen, A., Gürbüz, E. Y., Şirin, C., & Gungor, A. (2020). Energy-exergy and enviro-economic survey of solar air heaters with various air channel modifications. *Renewable Energy, 160*, 67-85. doi:10.1016/j.renene.2020.06.087

Udomkun, P., Romuli, S., Schock, S., Mahayothee, B., Sartas, M., Wossen, T., . . . Müller, J. (2020). Review of solar dryers for agricultural products in Asia and Africa: An innovation landscape approach. *Journal of Environmental Management, 268*, 110730. doi:10.1016/j.jenvman.2020.110730

van Eck, N. J., & Waltman, L. (2010). Software survey: VOSviewer, a computer program for bibliometric mapping. *Scientometrics, 84*(2), 523-538. doi:10.1007/s11192-009-0146-3

Vijayan, S., Arjunan, T. V., & Kumar, A. (2016). Mathematical modeling and performance analysis of thin layer drying of bitter gourd in sensible storage based indirect solar dryer. *Innovative Food Science & Emerging Technologies, 36*, 59-67. doi:10.1016/j.ifset.2016.05.014

Vijayan, S., Arjunan, T. V., & Kumar, A. (2020). Exergo-environmental analysis of an indirect forced convection solar dryer for drying bitter gourd slices. *Renewable Energy, 146*, 2210-2223. doi:https://doi.org/10.1016/j.renene.2019.08.066

Vijayan, S., Arjunan, T. V., Kumar, A., & Matheswaran, M. M. (2020). Experimental and thermal performance investigations on sensible storage based solar air heater. *Journal of Energy Storage, 31*. doi:10.1016/j.est.2020.101620

Yeh, H.-M. (2012). Upward-type flat-plate solar air heaters attached with fins and operated by an internal recycling for improved performance. *Journal of the Taiwan Institute of Chemical Engineers, 43*(2), 235-240. doi:https://doi.org/10.1016/j.jtice.2011.10.008

Zeng, K., Gauthier, D., Lu, J., & Flamant, G. (2015). Parametric study and process optimization for solar pyrolysis of beech wood. *Energy Conversion and Management, 106*, 987-998. doi:10.1016/j.enconman.2015.10.039

Zoukit, A., El Ferouali, H., Salhi, I., Doubabi, S., & Abdenouri, N. (2019a). Simulation, design and experimental performance evaluation of an innovative hybrid solar-gas dryer. *Energy*, 116279. doi:10.1016/j.energy.2019.116279

Zoukit, A., El Ferouali, H., Salhi, I., Doubabi, S., & Abdenouri, N. (2019b). Takagi Sugeno fuzzy modeling applied to an indirect solar dryer operated in both natural and forced convection. *Renewable Energy, 133*, 849-860. doi:10.1016/j.renene.2018.10.082

Contribution to the design of high-performance solar dryers using simulation tools coupled with design of experiments (DoE)

ABSTRACT

Solar energy is a free and renewable source of energy that can be a suitable alternative to using fossil fuels in drying applications. The solar dryers are one of the best solutions to avoid the shortcomings of open sun drying and high energy consumption in industrial drying. Indirect type solar dryer (ISD) is commonly used type for fruits and vegetables because it allows better control of drying to achieve required temperature, retention of product color, nil damage to crops. The quality of the dried products varies significantly with the uniformity of velocity and temperature distribution in the drying chamber. Accordingly, optimizing the operating conditions and the dryer design is of significant importance to improve the drying uniformity. Moreover, the challenging step in the conception of solar dryers (SDs) is achieving a design that enables uniform airflow distribution. Hence, a considerable number of experiments needed to obtain the optimal SD design is extremely time-consuming as well as not efficient from an economic point of view. CFD can be the key to optimize the geometric shape and operating parameters with low cost and reduced time compared to physical experiments. At the optimal conditions the solar air heater parameters were 52°C, 51.78% and 1397.34 W for the outlet temperature, thermal efficiency, and improvement potential (IP) respectively. The ISD optimal design improved the thermal efficiency by 15.76% and IP by 19.33%. The air temperature uniformity was improved significantly, by 21.7 and 20.3%, for the mass flow rate of $\dot{m}$=0.0141 and 0.06 $kg.s^{-1}$, respectively, while it was marginally increased for $\dot{m}$=0.08 $kg.s^{-1}$.

Key words: *renewable energy; solar drying; solar air heater; CFD; indirect solar dryer; response surface methodology (RSM);*

مساهمة في تصميم مجففاتٍ شمسية عالية الأداء باستخدام أدوات المحاكاة العددية مقترنة بطريقة مخططات التجارب (DoE)

الملخـص

تندرج هذه الأطروحة تحت إطار إيجاد بدائل مجانية ومتجددة للوقود الأحفوري المستعمل في عمليات تجفيف الأغذية الزراعية خاصة. من بين التقنيات المختلفة لتجفيف الفواكه والخضروات بالطاقة الشمسية، يعتبر المجفف الشمسي غير المباشر أفضل الخيارات لأنه يسمح بتحكم أفضل في التجفيف لبلوغ درجة الحرارة المطلوبة، الاحتفاظ بلون المنتج، وكذلك عدم إتلاف المنتوج المجفف.

تختلف جودة المنتجات المجففة اختلافًا كبيرًا مع انتظام سرعة الهواء وتوزيع درجة الحرارة في غرفة التجفيف. وفقًا لذلك، يعد تحسين ظروف التشغيل أو تصميم المجفف ذو أهمية بالغة للحصول على منتوج ذو جودة عالية. علاوة على ذلك، فإن الخطوة الصعبة في بناء تصميم جديد للمجفف الشمسي (أو حتى في حالة تجديد المجففات الشمسية القديمة) هي تحقيق تصميم يتيح توزيع منتظم لتدفق الهواء. ومن ثم، فإن عددًا كبيرًا من التجارب اللازمة للحصول على التصميم الأمثل يستغرق وقتًا طويلاً للغاية كما أنه غير فعال من الناحية الاقتصادية. يمكن أن تكون ديناميكا الموائع الحسابية هي المفتاح لتحسين الشكل الهندسي والتشغيل بتكلفة منخفضة ووقت أقل مقارنة بالتجارب المادية. تهدف هذه الدراسة الى تحسين شكل المجففات الشمسية. الطريقة المقترحة في هذه الاطروحة تعتمد على العمل التجريبي، المحاكاة العددية، والامثلة متعددة الاهداف .اعتمدت الدراسة بشكل اساسي على تحسين تجانس التجفيف داخل مجفف شمسي غير مباشر. يعتبر هذا الاخير اختيار يتوافق وتجفيف الاغذية. الطريقة المقترحة خلال الدراسة يمكن تطبيقها في تحسين تصميم الأنظمة الطاقوية المماثلة. بعد تحسين سخان الهواء الشمسي كانت الظروف المثلى 52 درجة مئوية و 15.76% و 1397.34 واط لدرجة حرارة المخرج والكفاءة الحرارية و IP على التوالي. أدى تصميم ISD الأمثل إلى تجانس الحرارة في غرفة التجفيف بنسبة 15.76٪ و IP بنسبة 19.33٪. تم تحسين اتساق درجة حرارة الهواء بشكل ملحوظ، بنسبة 21.7 و 20.3٪، لمعدل تدفق الكتلة بمقدار $\dot{m}$ = 0.0141 و 0.06 $kg.s^{-1}$ على التوالي ، بينما تمت زيادتها هامشيًا لـ $\dot{m}$ = 0.08 $kg.s^{-1}$.

الكلمات المفتاحية: *الطاقات المتجددة، التجفيف بالطاقة الشمسية، اللاقط الشمسي الهوائي، المحاكاة العددية، المجفف الشمسي غير المباشر.*